DESIGN AND ANALYSIS OF HONEYCOMB STRUCTURES WITH ADVANCED CELL WALLS

A Dissertation

by

RUOSHUI WANG

Submitted to the Office of Graduate and Professional Studies of
Texas A&M University
in partial fulfillment of the requirements for the degree of

DOCTOR OF PHILOSOPHY

Chair of Committee,	Xinghang Zhang
Co-Chair of Committee,	Jyhwen Wang
Committee Members,	Amine Benzerga
	Karl 'Ted' Hartwig
Head of Department,	Ibrahim Karaman

December 2016

Major Subject: Materials Science and Engineering

ABSTRACT

Honeycomb structures are widely used in engineering applications. This work consists of three parts, in which three modified honeycombs are designed and analyzed. The objectives are to obtain honeycomb structures with improved specific stiffness and specific buckling resistance while considering the manufacturing feasibility.

The objective of the first part is to develop analytical models for general case honeycombs with non-linear cell walls. Using spline curve functions, the model can describe a wide range of 2-D periodic structures with nonlinear cell walls. The derived analytical model is verified by comparing model predictions with other existing models, finite element analysis (FEA) and experimental results. Parametric studies are conducted by analytical calculation and finite element modeling to investigate the influences of the spline waviness on the homogenized properties. It is found that, comparing to straight cell walls, spline cell walls have increased out-of-plane buckling resistance per unit weight, and the extent of such improvement depends on the distribution of the spline's curvature.

The second part of this research proposes a honeycomb with laminated composite cell walls, which offer a wide selection of constituent materials and improved specific stiffness. Analytical homogenization is established and verified by FEA comparing the mechanical responses of a full-detailed honeycomb and a solid cuboid assigned with the calculated homogenization properties. The results show that the analytical model is accurate at a small computational cost. Parametric studies reveal nonlinear relationships

between the ply thickness and the effective properties, based on which suggestions are made for property optimizations.

The third part studies honeycomb structures with perforated cell walls. The homogenized properties of this new honeycomb are analytically modeled and investigated by finite element modeling. It is found that comparing to conventional honeycombs, honeycombs with perforated cell walls demonstrate enhanced in-plane stiffness, out-of-plane bending rigidity, out-of-plane compressive buckling stress, approximately the same out-of-plane shear buckling strength, and reduced out-of-plane stiffness. For the future design, empirical formulas, based on finite element results and expressed as functions of the perforation size, are derived for the mechanical properties and verified by mechanical tests conducted on a series of 3D printed perforated honeycomb specimens.

ACKNOWLEDGEMENTS

I would like to thank my committee chair and co-chair, Dr. Zhang and Dr. Wang, and my committee members, Dr. Benzerga, and Dr. Hartwig, for their guidance and support throughout the course of this research.

I would also like to thank my colleagues, Cheng-Kang Yang and Ying Zhang, for providing me assists and advice on my research. Thanks also go to my friends and the department faculty and staff for making my time at Texas A&M University a great experience.

Finally, I'd like to thank my mother Xiaoli Yang and father Xiaojun Wang for their encouragement and to my wife, Feng Jiang, for her patience and love during the last year of my study.

TABLE OF CONTENTS

Page

Page

LIST OF FIGURES

Page

Page

Page

Page

LIST OF TABLES

Page

1. INTRODUCTION

Honeycombs are 2-D cellular materials with a regular periodic microstructure inspired from biological structures such as bee hives, microstructure of abalone shells and bamboo cross-sections [1–3]. As one of the most famous product of bionic engineering in human history, honeycombs provide ideal solutions for the balance between high stiffness, high strength and light weight. In addition, honeycombs with regular hexagonal cells perform perfect in-plane isotropy, which greatly reduced the effort of modeling and analysis [4].

The first blooming of honeycomb materials began with Hugo Junkers patented the first weight-saving sandwich panel core designed for aircraft wing boxes in 1915. Since then, light-weight sandwich beams and shells with honeycomb cores have become the most well-known and mostly manufactured honeycomb material products. By bonding face sheets on the two transverse sides of honeycomb structures, the sandwich panels can sustain large out-of-plane compression, bending and shear loads with a small weight cost [5–11]. Note that the term “plane” used in this dissertation defaults to the plane in which the 2-D periodicity extends. With the further study and understanding of the features of honeycomb materials, many novel applications of honeycombs such as morphing wings [12–14], non-pneumatic tires [15] and energy absorption structures for dynamic crushing [16–18] have also attracted attention in recent years. Attentions have also been paid on the honeycomb structures’ capabilities of heat dissipation [19,20], noise insulation [21–24] and fire-resistance [25] owing to their cellular geometry.

There are two widely used processes for honeycomb manufacturing, as shown in Fig. 1.1 [10]. In the first process (Fig. 1.1. (a)), the raw materials sheets are first cut into panels, then adhesive bond strips are applied on both sides of each panel in a periodic manner. After stacking together and the adhesive is cured, the sheet piles are pulled and expanded to form the hexagon honeycombs. In another process (Fig.1.1 (b)), raw material sheets are first corrugated, then stacked together and welded.

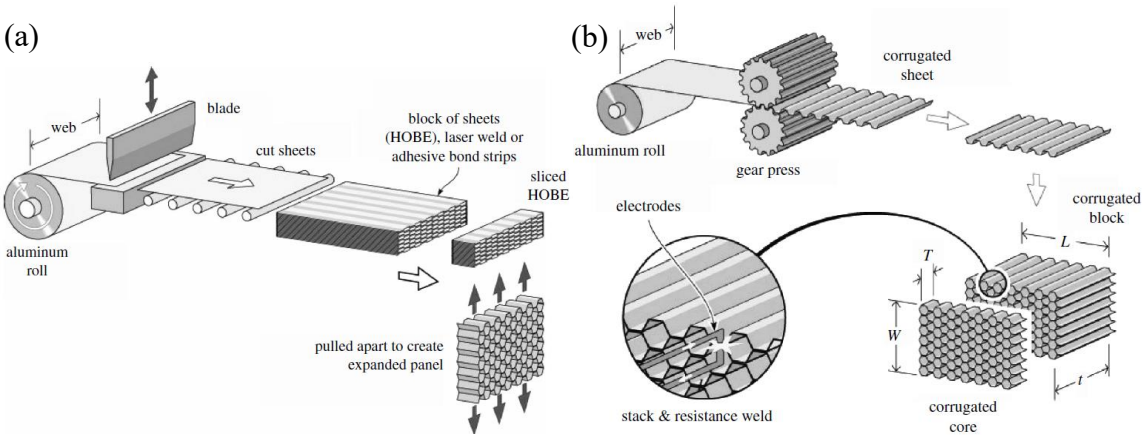

Fig. 1.1. Two widely used honeycomb manufacturing processes. (a) Bonding-expanding process; (b) Corrugation-welding process. (reprinted from Haydn N.G Wadley, 2006) [10].

1.1 Literature Review on Honeycomb Materials

For all of the honeycombs' applications introduced above, a reliable analytical model is indispensable to predict their mechanical responses and design products with tailored properties. The commonly used analytical modeling method for honeycombs is to find their homogenized properties so that the whole structure can be treated as an

orthotropic solid material, which greatly simplifies the calculation complexity. The most widely recognized fundamental work that firstly and comprehensively described the mechanical behaviors of general case honeycombs and their analogues was done by Gibson and Ashby in 1990 [1]. Although they have stated in their work that not all results were well-investigated, this work has still been treated as the cornerstone of the following research in this field. In 1996, Masters and Evans [26] proposed an improved in-plane elastic and shear moduli model of hexagonal honeycombs by taking the hinging and stretching effect into consideration. Since the most well-known application of honeycomb materials is sandwich panel cores, the early stage researches of honeycomb modeling mainly focused on the out-of-plane properties. As one of the examples, Kelsey et al. [27] developed a model for the shear stiffness of hexagonal honeycombs by the classical energy method in 1958 and verified it by a series of shear and bending tests.

One shortcoming of those early stage models, including Gibson and Ashby's model, is that the effective transverse shear modulus was only given in the form of upper bound and lower bound. These two bounds coincide when the unit cell is regular hexagon, but in some special cases the difference between the two bounds can be as high as 100% [28]. Penzien and Didriksson [29] provided a modified model by formulating a displacement field and introducing warping effect of sandwich skins. They found that the transverse shear moduli of honeycomb sandwich are related to its out-of-plane depth. To find a precise solution for the transverse shear moduli, Grediac [28] conducted parametric studies on honeycombs with a series of different aspect ratios by FE and concluded that the exact value of effective transverse shear modulus depends on the ratio of cell wall

length and width, i.e. the out-of-plane depth. An empirical function was then given to help predict the exact shear modulus between the upper and lower bound. Based on this result, Shi and Pin [30] proposed an improved lower limit calculation method for the effective transverse shear modulus, which agrees well with the experimental results. To explain the mechanism behind the empirical function, Pan et al. [31] presented a new analytical model for the effective transverse shear modulus by combining cantilever beam bending theory and the thin plates shear strength theory. Xu et al. [8] extended the analytical transverse shear model of Pan et al. to general configuration honeycombs by a two-scale asymptotic analysis.

The out-of-plane bending rigidity of honeycombs is also a vital property of honeycomb materials. Because of the fact that bending deformation of honeycombs cannot be treated as a plate bending problem by using the effective in-plane elastic modulus, Chen [32,33] derived a detailed honeycomb out-of-plane bending and torsion model by combining the 3-D rotation and twisting of each cell wall in a honeycomb panel unit cell. Chen's model successfully described the anticlastic shape honeycomb panel forms under bending load, and it became the most reliable solution in this field.

Other than the traditional mechanics of material approach, many different methods have also been used to homogenize honeycomb materials. Similar to Kesley et al's work [27], Hohe et al. [34,35] presented an energetic homogenization approach for triangular, hexagonal, quadrilateral and general case honeycomb based on the assumption of equivalence representative volume element (RVE) energy, and theirs result showed good agreement with experiments. In their latest work, this method was extended to all polygon

cellular materials [36]. As a special case of honeycomb homogenization, Qiao and Wang [37] derived the mechanical model for fiber reinforced polymer (FRP) sinusoidal honeycomb by strain energy method. Li et al. [38] used trigonometric function series to derive the minimized internal strain energy according to a close observation of the displacement field on a deformed numerical model, and it showed very good agreement with FE simulation results. To avoid the inaccuracy results from the analytical assumptions and geometry simplifications, some researchers abandoned tedious equations and tried to include all of the geometry details of a unit cell in a numerical homogenization process to find the most precise solution. Works of Grediac [28] and Shi and Pin [30] can be treated as precursors of this field. To reduce the computational cost of the effective elastic properties of foam-filled honeycombs, Burlayenko and Sadowski [39] proposed a displacement based homogenization technique via 3-D finite element analysis. Similar research has also been carried out by Sadowski and Bęc [40]. In the FE homogenization strategy proposed by Catapano and Montemurro [41], the cell walls' stress distribution along its thickness was firstly taken into consideration. In the second part of their work, a two-level optimization procedure based on their numerical homogenization and a genetic algorithm is proposed [42].

Since honeycombs are usually used for load-bearing and energy absorbing, great attentions have also been paid on their failure and collapse behaviors, especially the out-of-plane yielding, buckling and crushing properties. In 1963, McFarland [43] assumed the simplified honeycomb collapse model based on the observation of a honeycomb crushing experiment and obtained the first analytical solutions of the upper and lower limits of

honeycombs' crushing stress. Wierzbicki [44] modified McFarland's collapse model by replacing the semi-empirical buckling wave assumption with a calculated wavelength and changing the deformation type, which was proven to be closer to the real-tested collapse stress. Based on Timoshenko's theory of elastic instability [45], Zhang and Ashby [46] derived the upper bond and lower bond of honeycombs' buckling stress by assuming the extreme cases of cell walls boundary conditions. However, the similar shortcoming showed again—the difference between the two bonds is too significant. Some experimental and numerical observations of the collapse process of honeycombs showed that the cell walls remain flat before the onset of the first eigenmode for buckling, which always happens before plastic yielding for thin wall honeycombs [47,48]. Inspired by these facts, Jiménez and Triantafyllidis [49] combined Bloch wave theory and von Kármán plate theory to solve for the onset of the first bifurcation buckling, and the result was successfully verified by FE simulations conducted on representative volume element (RVE) models of hexagonal and square honeycombs.

In addition to deriving the reliable homogenization models, the modification and improvement of honeycomb structures for tailored properties has also attracted significant attention. Some researchers seek higher specific stiffness and specific strength while others aim at achieving certain properties with minimum material cost. Conventionally, there are two approaches achieve these goals: (1) changing the cell walls' arrangement, such as cell wall length, angle and thickness; (2) replacing the cell walls with substructures.

The first approach is mostly based on Gibson and Ashby's fundamental honeycomb model and is already widely employed in design of honeycomb products. Wang and McDowell [4] compared the in-plane stiffness and yield strength (which is designed to occur before elastic buckling) of seven different periodic lattices and demonstrated that honeycombs with diamond, equilateral triangle and kagome (a hexagram-like cell) unit cells have superior in-plane mechanical properties among them. Ju et al. [50] conducted a series of functional designs on honeycombs with various angles and fixed width to reach a target shear modulus. They also derived a design space of material and geometry for the target shear modulus. Hou et al. [51] presented an optimized geometry design of aluminum honeycomb sandwich panels for high crashworthiness resistance. Singh et al. [52] and Chen and Davalos [53] discussed the influence of sandwich skin and fill-in materials on the structure selection for various loadings. All of the above optimization approaches are straightforward in calculation and easy to be realized in manufacturing, but the range of material properties that can be achieved are limited. On the other hand, many researches have already proven that regular hexagonal is the optimum unit cell geometry for honeycombs to attain the maximum out-of-plane specific buckling resistance and out-of-plane specific shear stiffness [26]. Regular hexagonal unit cells can also provide isotropic homogenized in-plane moduli, which is an important characteristic in many applications. Hence, there are very few options for cell wall arrangement design.

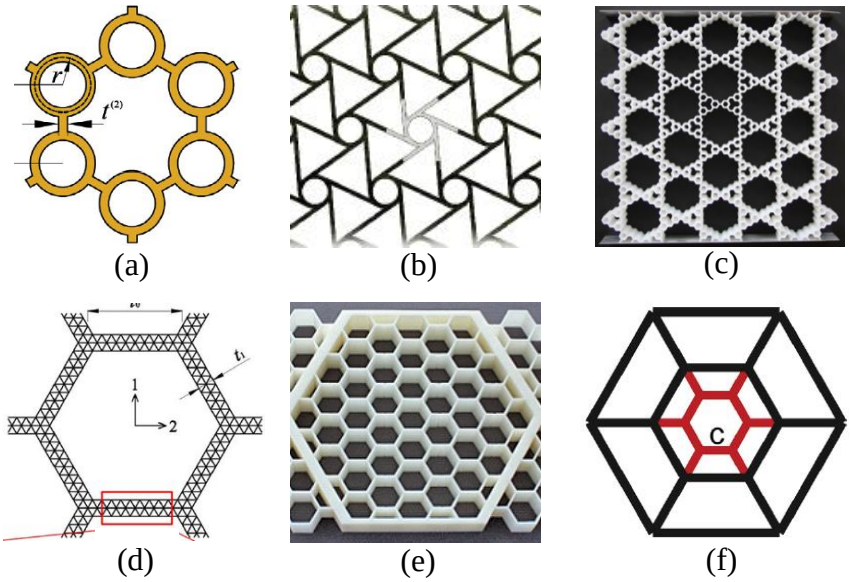

Fig. 1.2. Examples of honeycombs with substructures. (a) Cylinder joint honeycomb [54] (reprinted from Chen Q, et al., 2014); (b) auxetic chiral honeycomb (reprinted from Karnessis N, Burriesci G, 2013) [55]; (c) honeycomb with hierarchy joints (reprinted from Ajdari A, et al., 2012) [56]; (d) honeycomb with hierarchy cell walls (reprinted from Sun Y, Pugno NM, 2013) [57]; (e) multi-order honeycomb (reprinted from Taylor CM, 2011) [58]; (f) spider web hone (reprinted from Mousanezhad D, et al., 2015) [66].

The second approach is relatively new and drawing increasing attentions in the recent decades. In most of the related researches, the overall configuration of a honeycomb unit cell is remained as regular hexagons, but part or all of the cell walls or joints are replaced by substructures. Figure 1.2. depicts some of these examples. Observing the non-uniform thickness of natural bee hive cell walls, Chen et al. [54] designed and analyzed a novel cylindrical-joints honeycomb structure (Fig. 1.2. (a)) with in-plane Young's moduli and fracture strength 76% and 303% higher than those of the conventional honeycombs, respectively. Similar geometries are also employed on some auxetic structures called "chiral" honeycombs (Fig. 1.2. (b)), in which the cell walls are not perpendicularly but tangentially connected with the cylinder joints to maintain a constant negative Poisson's

ratio over a significant range of strain [55,59,60]. The concept of hierarchy, another kind of high weight-efficiency structures, is also introduced into honeycomb designs by many researchers [61]. The structure investigated by Ajdari et al. [62] in their research is a typical case of hierarchical honeycombs (Fig. 1.2. (c)). By adjusting the structural aspect ratio of the first and second order hierarchy honeycombs, they obtained increased in-plane specific stiffness up to 2.0 and 3.5 times as large as that of the regular hexagonal honeycombs, respectively. Oftadeh et al. [63] conducted parametric studies on the similar structure and evaluated the highest achievable elastic modulus for different total hierarchy orders and relative densities to help structure design. Pugno's group [57,64,65] comprehensively studied honeycombs with different kinds of hierarchical cell walls, including triangle (Fig. 1.2. (d)), hexagon, kagome, re-entrant hexagon and chiral triangle. Except replacing the existing structure, some authors suggested filling hierarchy substructures in the cell voids. Taylor et al. [58] filled second order honeycombs in the void space of the first order honeycomb unit cells (Fig. 1.2. (e)) and conducted parametric studies on both sub- and super-structure geometries, which showed that in the optimized case, the in-plane specific stiffness was increased by 75% compared with conventional honeycombs. Mousanezhad and Davood [66] analytically modeled and tested a unique hierarchical honeycomb with spider web-shaped substructure (Fig. 1.2. (f)) and demonstrated an elevated capacity of energy absorption. Computer aided topology optimization is a novel but very powerful tool in structure design, which helps designers to acquire optimal structures for a maximized target parameter. Larsen et al. [67] used this method to design the unit cell of compliant micromechanisms and showed that numerical

topology optimization can also greatly reduce the design cycle of new products (they finished their design, fabrication and tests in one day). Almost all of those studies reported remarkable improvement in specific stiffness and buckling resistance (some of them can even increase by 300%-400%), but they suffer from a common disadvantage for being difficult to fabricate due to their unusually complicated geometries. Currently, most of them can only be produced via 3-D printing, which greatly restricts the extensive use of those structures in industry.

Inspired by the literature above and considering the manufacturing feasibility, this work proposes three novel honeycomb improvement approaches. The first approach replaces the straight cell walls with spline-shaped cell walls, which functions as a new modeling method for honeycombs with general case geometries as well. The second approach replaces the solid cell walls with laminated composites to obtain further enhanced specific stiffness, special cell walls surfaces and a wider range of material options to reach target effective properties. The third approach proposes a novel honeycomb with perforated cell walls for an increased in-plane stiffness and out-of-plane buckling resistance.

1.2 Honeycombs with Spline Cell Walls

In the ideal models, the cell walls of a honeycomb are usually flat thin plates or straight lines in 2D view. In practice, most honeycomb products inevitably contain curved cell walls created during the widely used adhesion-expansion manufacturing process [10],

as shown in Fig. 1.3. (a). In other cases, some honeycombs with corrugated cell walls are made on purpose to obtain enhanced out-of-plane stability, as shown in Fig. 1.3 (b). Experiments have demonstrated that those nonlinear geometries could greatly reduce the reliability of the traditional analytical model predictions which are based on ideal straight cell walls [37]. To reflect the influence of cell walls' curvature in analytical models, William [68] introduced circular arc in the junction region of the cell walls as an imitation of the deformed cell walls; and Qiao and Wang [37] developed the analytical model for honeycombs with sinusoidal cell walls. Those models provided satisfying solutions for specific type of honeycomb cell walls curvature, but could not be used as general solutions for arbitrary cell wall curvature. In addition to the regular hexagons, honeycombs with many other cell geometries, such as triangle, square, kagome, and rectangular have also been investigated to meet the performance requirements of different applications [10,11]. Hohe and Becker [11] developed a new modeling approach for general case unit cells by discretizing the 2-D cell wall geometry into straight segments to approximate the curved cell walls. Xu, et al. [8] reported a different homogenization method for honeycombs with arbitrary 2-D unit cell configurations by solving partial differential equations. Those models provide exact solutions for arbitrary unit cell geometries, but require great mathematical efforts to describe specific honeycomb cells geometries.

In this part of work, efforts are made to use spline curve functions to build a unique unit cell that can be easily modeled and simply transformed to describe different cell geometries. By selecting enough control points, spline curve unit cells can approximate arbitrary 2-D single-curve geometries with a much higher flexibility than traditional

straight, circular, or sinusoidal models, and that the well-established spline functions and theories allow relatively simple and invariable expressions for the homogenized moduli. The introduction of cell wall corrugation brings greatly enhanced out-of-plane buckling resistance due to the enlarged second moment of inertia offers an alternative to tailoring and optimizing honeycomb through cell wall length, angle, and thickness change.

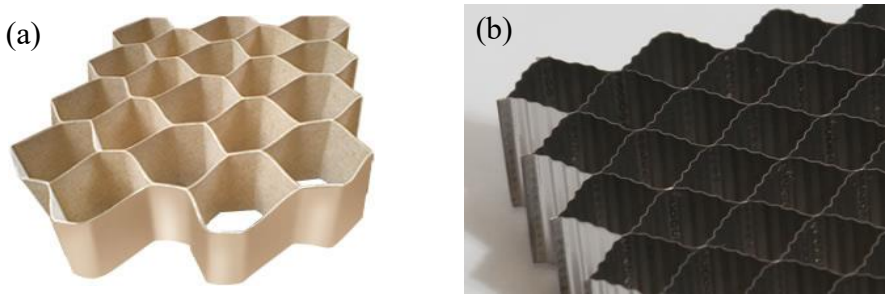

Fig. 1.3. Honeycomb with nonlinear cell walls. (a) Curvature formed during bonding-expanding process (www.lhexagone.com/carton-nid-abeilles.php); (b) Wavy cell walls to increase buckling resistance (www.indyhoneycomb.com/products/structural-honeycomb/).

1.3 Honeycombs with Composite Laminated Cell Walls

One of the benefit of using composite laminates is the enhanced bending rigidity at a small increased weight. To obtain maximized bending rigidity, the stiffer plies are usually placed at the outermost layers to bear the maximum in-plane stress. In this part, this feature of composite laminates is utilized to improve the in-plane stiffness of honeycombs by replacing the single material cell walls with composite laminates. Fan et al. [69] presented a similar work on honeycomb with sandwich cell walls consist of two surfaces separated by a light middle core. They have assumed that the middle core

functions only as a spacer and all of the in-plane loads are carried by the surface sheets. The effect of surface spacing on the homogenized in-plane moduli was investigated, but the effect of employing multi material laminates was not discussed. By employing multi-layer cell walls in honeycombs, designers can get a wider material options to reach certain required homogenized properties, elevated specific stiffness and strength and alterable cell wall surfaces.

Another reason of choosing composite laminated cell walls is its easiness of manufacturing. With the widely used bonding-expanding or corrugation-welding processes (Fig. 1.1.), honeycombs with composite cell walls honeycombs can be fabricated by simply replacing the single layered cell wall with composite laminates. Due to the bonding process, the cell walls in the bonding area will have twice the thickness. This characteristic is considered and discussed in the following sections.

1.4 Honeycombs with Perforated Cell Walls

Two strategies of honeycomb geometry modification can be summarized from the previous works on honeycombs with substructures to increasing the homogenized stiffness and strength: (1) reinforcing the cell wall joints, (2) shortening the span of single cell walls. Based on these facts and considering the manufacturing feasibility, this work proposes a novel honeycomb with perforated cell walls. One of the supporting proof for this innovation is a computer aided topology optimization conducted by Dale et al. [13] on a honeycomb used in an aircraft morphing wing. Their program generated perforations

on the honeycomb cell walls to reach a higher specific bending rigidity, but no analytical discussion was provided. Currently, to the best of the author's knowledge, no research has been reported on the mechanical properties of honeycombs with perforated cell walls. There are some commercial honeycomb products with small perforations on their cell walls, but the purpose is mostly for air ventilation, water draining or pipeline connections.

The advantage of punching openings on honeycomb cell walls in increasing its overall effective in-plane stiffness is obvious. Many fundamental works have stated that when the honeycomb undergoes external in-plane loads, the stress on a honeycomb cell wall concentrates at its two ends [1]. Chen's group chose to enhance the joints by utilizing this phenomenon [54]. Similarly, but there could also be a substantial weight-saving benefit by removing the materials in the middle area. For the out-of-plane properties, a large number of researches on perforated thin plates have reported that although a circular opening at the center of the plate reduces thin plates' effective stiffness, it increases the specific buckling resistance of the plate if the perforation's size and location are in a certain range [70–84]. Yu, et. Al. [70] investigated the relationship between the in-plane compressive buckling coefficient *k* and the ratio of the hole diameter to the plate length of a square plate with its loading edges clamped and the other two edges simply supported. Their study revealed that when constant strain load is applied, which is a common loading condition for honeycomb materials, *k* first decreases slightly as the hole diameter changes from zero to half of the plate. The coefficient, *k*, then rises over the initial value as the hole diameter keeps increasing. Since it has been proven that for thin wall honeycombs made from common materials, elastic buckling always occurs before plastic yielding [47,48],

there is a room of strengthening by postponing the occurrence of bifurcation to a larger strain. Although the boundary condition of a honeycomb cell wall is different from that of a single plate and the failure mode may change with different perforation sizes, such improvement is still significant if the evaluation is based on unit weight. Roberts, et. al.'s [71] FEA study showed that different from compressive buckling, the shear buckling coefficient factor of a square plate decreases monotonically as the size of perforation increases. However, such decrease can be compensated by the saved structure weight. Although other perforation shapes such as square and triangle have also been investigated, it has been concluded that centric circular openings, in general, provide larger load carrying capacity than others [85–88]. Perforated honeycombs are also expected to have other potential advantages such as improved noise and heat insulation, which, however, are not in the scope of this research.

One approach to analyze the overall deformation of perforated honeycombs under uniform loads is to decompose it into the deflections of perforated thin plates with appropriate boundary conditions. Although the mechanical responses of perforated thin plates have attracted significant attention since 1960s, there is still no exact analytical solution available for the deflection functions of plates with large perforations (the effect of the hole on the plate's edge stress is not negligible) due to the non-linear inner boundary [89,90]. A number of authors have presented approximate solutions for different loads by point-matching method [89–92] or Rayleigh-Ritz method [93,94]. Theoretically, such method can provide accurate result if the number of the series function terms are infinite, but within typical range of calculation complicity (10-20 terms), results calculated from

these method deviates greatly from experiment or FEA results when the hole size exceeds half of the plate width [72–75,91–95]. For this reason, most of the relevant studies are based on FEA since the early 1970s [75,77].

To produce perforated honeycombs, a sheet perforation process is needed before the conventional process (Fig. 1.1) to introduce the designed periodic perforation pattern. This extra process would increase the cost, but it is anticipated to be more economy than the 3D printing of hierarchy honeycombs when produced in mass.

1.5 Research Objectives

To narrow down the scope of this research and avoid the influence of trivial factors, the presented research focuses only on thin wall honeycombs (cell wall thickness-to-length ratio is less than 1/15) under uniform quasi-static external loads. The mechanical responses discussed are within elastic range and free from adhesive debonding. The method of homogenization is used in the analytical modeling sections of three parts, which treat the periodic cellular structures as orthotropic bulks with homogeneous moduli and strengths.

The objective of the first part is to establish the homogenized orthotropic stiffness matrix for general case honeycombs by Bezier spline functions. Energy method and Castigliano's theorem are used to extract the force-displacement relationship of a single cell wall, and the homogenized moduli are derived according to the different connection manners of the cell walls. The derived analytical model is then applied to represent three

special honeycomb configurations having sinusoidal, hexagonal and monolithic unit cells. Numerical and experimental verifications are also conducted for a comprehensive verification. Parametric studies are conducted, analytically and numerically, to examine the influence of the spline cell wall geometries on the honeycomb's effective in-plane properties and the out-of-plane stability.

The objective of the second part is to derive the analytical homogenized stiffness matrix of honeycombs with irregular hexagonal unit cells and *n*-layer cell walls by combining Gibson and Ashby's fundamental honeycomb model and the classical laminated plate theory(CLPT). The analytical model is verified by comparing the simulation tests results of a full-detailed double layer cell wall honeycomb model and a monolithic model assigned with the calculated homogenized properties. In the parametric study section, those two models are used to investigate how the laminate plies influence the honeycomb's homogenized properties.

The objective of the third part is to derive the homogenized elastic moduli, bending rigidities and out-of-plane critical buckling stresses of perforated honeycombs. As an initial work on this kind of new honeycombs, only square thin cell walls with centric circular perforations were studied since they can be assumed to have single half wave of buckling deflection, which maximizes the influence of the perforations. All the cell walls have the same length and thickness, but the cell wall angle can vary. Parametric studies were conducted by FEA to investigate how perforation size changes the homogenized properties. Approximated analytical solutions and empirical formulas derived from FEA

results are provided for the effective moduli and critical stresses for the future designing of this type of structures.

2. HONEYCOMBS WITH SPLINE CELL WALLS

2.1 Analytical Modeling

2.1.1 Bezier Curve Function

Originally, spline means curves formed by forcing a highly flexible wood slat pass though certain fixed points. The basic form of spline curve functions consists of piecewise cubic functions locate between every two adjacent control points with a second order continuity at each junction. To achieve a better geometric control, Bezier curve was created, which can define weight factors on each control point and specify tangent direction at the two ends by the relative position between the first two and last two control points. Based on Bezier curve, a further advanced model called B-spline was developed, which additionally allows local shape adjustment without global propagation.

For the honeycomb structures discussed in this study, the non-linear cell walls are expected to have zero slope (horizontal tangent) at their junctions due to adhesive bonding, hence Bezier curves become a suitable choice for their simple control on the starting and ending curve slope. Since prevention of the control points' global propagation is not required, it's not necessary to employ the higher order B-spline function sets. The basic function of Bezier curve is:

$$P(u) = \sum_{i=0}^{n} P_i B_{i,n}(u), u \in [0,1] \tag{2.1}$$

in which P_i is the coordinates of the *ith* control point and $B_{i,n}$ is defined by:

$$B_{i,n}(u) = \frac{n!}{i!\,(n-i)!} u^i (1-u)^{n-i}, u \in [0,1] \tag{2.2}$$

where *n* is the total number of control points minus one. In this part, Bezier curves with four control points is selected in the analytical modeling, as shown in Fig. 2.1. By adjusting the point locations and the unit cell size, it can represent honeycombs with unit cell geometries of hexagon, triangle, kagome, square, diamond, sinusoidal wave, etc. Thus, setting *n*=3 yields the Bezier curve function:

$$P(u) = (1-u)^3 P_0 + 3u(1-u)^2 P_1 + 3u^2(1-u)P_2 + u^3 P_3, u \in [0,1] \tag{2.3}$$

or in form of parametric equations with separated X_1 and X_2 coordinates:

$$X_1(u) = (1-u)^3 P_0(x_1) + 3u(1-u)^2 P_1(x_1) + 3u^2(1-u)P_2(x_1) + u^3 P_3(x_1),$$
$$u \in [0,1];$$
$$X_2(u) = (1-u)^3 P_0(x_2) + 3u(1-u)^2 P_1(x_2) + 3u^2(1-u)P_2(x_2) + u^3 P_3(x_2),$$
$$u \in [0,1] \tag{2.4}$$

where $P_i(x_1)$ and $P_i(x_2)$ are the X_1 and X_2 coordinates of point Pi respectively. The coordinates of the four control points are $P_0(0, 0)$, $P_1(a, 0)$, $P_2(l\text{-}a, h)$ and $P_3(l, h)$. *l* and *h* are the length and height of the unit cell respectively. P_1 and P_2 have the same X_2-coordinate values as those of P_0 and P_3 respectively to maintain a horizontal tangent at P_0 and P_3. The extent of the curve's undulation with respect to the P_0-P_3 center line is controlled by a shape parameter *a*—when $a=0$, the curve is a straight line; the larger *a* is,

the curvier the cell wall becomes. When $a=1$, the tangent at the midpoint of the curve is vertical. The elastic modulus and Poisson's ratio of the solid material of the cell walls are E_s and v_s respectively, and the thickness of the cell wall t is uniform along its length.

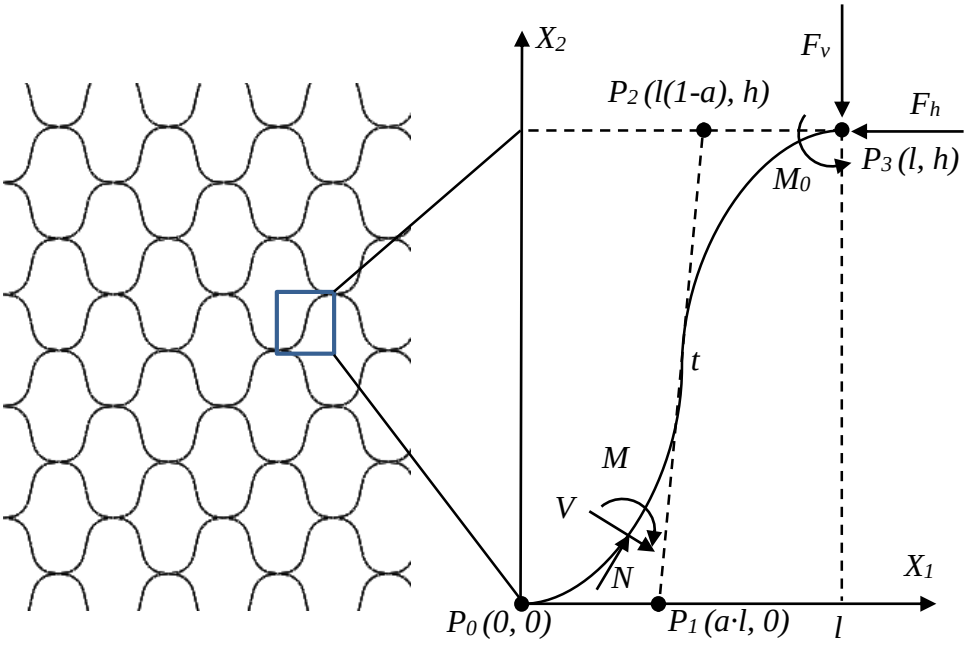

Fig. 2.1. Unit cell of honeycombs with spline cell walls.

2.1.2 In-plane Properties

The homogenized orthotropic stiffness matrix of the spline honeycomb is derived in this and the next subsections. With the curve functions given in Eq. (2.4), strain energy method is employed to calculate the elastic responses of the unit cells, which are the basic elements of the honeycomb's overall mechanical responses. Assuming that the uniform loads applied on the whole honeycomb structure in the X_1 and X_2 direction generate

concentrated vertical force F_v and horizontal force F_h on the two ends of each cell wall, which lead to internal axial force N, shear force V and bending moment M on an arbitrary cell wall sections:

$$N = F_h \frac{1}{\sqrt{1+(\frac{dX_2}{dX_1})^2}} + F_v \frac{\frac{dX_2}{dX_1}}{\sqrt{1+(\frac{dX_2}{dX_1})^2}},$$

$$V = F_h \frac{\frac{dX_2}{dX_1}}{\sqrt{1+(\frac{dX_2}{dX_1})^2}} - F_v \frac{1}{\sqrt{1+(\frac{dX_2}{dX_1})^2}},$$

$$M = F_h X_2 - F_v X_1 + M_0 \tag{2.5}$$

where M_0 denotes the reaction moment at the two ends to maintain the zero slope:

$$M_0 = \frac{F_v l}{2} - \frac{F_h h}{2} \tag{2.6}$$

Since X_1 and X_2 are functions of u (Eq. (2.4)), dX_2/dX_1 can be replaced by $(dX_2/du)/(dX_1/du)$. Note that in order to let the following integration solvable, this conversion can only be applied when dX_1/du is positive over the whole domain of $u \in [0,1]$, which leads to the constraint of $a \leq 1$. However, this restriction can be eliminated by rotating the coordinate system. The total elastic strain energy over the spline cell wall is:

$$U = \int_0^1 \left(\frac{\alpha_N N^2}{2} + \frac{\alpha_V V^2}{2} + \frac{\alpha_M M^2}{2} \right) \sqrt{1+\left(\frac{dX_2}{dX_1}\right)^2} \frac{dX_1}{du} du \tag{2.7}$$

in which

$$\alpha_N = \frac{1}{E_s t}, \alpha_V = \frac{1}{G_s t}, \alpha_M = \frac{12}{E_s t^3} \tag{2.8}$$

Applying Castigliano's theorem, the deflections in the X_1 and X_2 direction can be calculated as:

$$\Delta X_1 = \frac{\partial U}{\partial F_h}, \Delta X_2 = \frac{\partial U}{\partial F_v} \tag{2.9}$$

which are functions of concentrated force F_h and F_v. To obtain the effective modulus in the X_1-direction E_1^* and the effective in-plane Poisson's ratio v_{12}^*, the X_2-direction load is assumed to be zero (free expansion condition), that is, $F_v = 0$. The two effective properties can be calculated:

$$E_1^* = \frac{F_h l}{\Delta X_1 (h + t_1)},$$

$$v_{12}^* = -\frac{\Delta X_2/(h + \mathrm{t})}{\Delta X_1 / l} \tag{2.10}$$

where the horizontal force F_h is cancelled and E_1^* and v_{12}^* are only determined by E_s, v_s and unit cell geometry. Considering the cell wall thickness, $h+t$ is used as the total unit cell height. By the same method, E_2^* and v_{21}^* can be calculated by setting $F_h = 0$, which gives

$$E_2^* = \frac{F_v(h+t)}{\Delta X_2 l},$$

$$v_{21}^* = -\frac{\Delta X_1/l}{\Delta X_2/(h+t)} \tag{2.11}$$

The two effective Poisson's ratios also satisfy the symmetry condition of orthotropic materials:

$$v_{21}^* = v_{12}^* \frac{{E_2}^*}{{E_1}^*} \tag{2.12}$$

The in-plane shear modulus ${G_{12}}^*$ can be obtained by solving

$$\Delta X_2 = \frac{\partial U}{\partial F_v} = 0 \tag{2.13}$$

Once F_h is represented in terms of F_v, ${G_{12}}^*$ can be calculated as:

$$G_{12}^* = \frac{F_h/l}{\Delta X_1/(h+t)} \tag{2.14}$$

2.1.3 Out-of-plane Properties

The out-of-plane properties are straightforward in derivation since they are less dependent on the specific curve shape. The out-of-plane compression stiffness ${E_3}^*$ is calculated directly by the Voigt's upper bound theory:

$$E_3^* = \frac{E_s S t}{(h+t)l} \tag{2.15}$$

where S is the total length of the cell wall:

$$S = \int_0^s ds = \int_0^1 \sqrt{1 + \left(\frac{dX_2}{dX_1}\right)^2} \frac{dX_1}{du} du \tag{2.16}$$

The out-of-plane shear moduli were calculated based on Xu and Qiao's work [8]:

$$G_{13}^* = \frac{G_s t l}{(h+t)S} \tag{2.17}$$

$$G_{23}^* = \frac{G_s t (h+t)}{lS} \tag{2.18}$$

The out-of-plane Poisson's ratios are of minor importance in this study, thus the approximated solutions suggested in Gibson and Ashby's work are used:

$$v_{13}^* = v_{23}^* = 0;$$

$$v_{31}^* = v_{32}^* = v_s \tag{2.19}$$

2.1.4 Boundary Condition: Horizontal Plates

In this case, the spline cell walls are connected by horizontal plates with a thickness of t_h, as shown in Fig. 2.2 (a) and Fig. 2.2 (b). In the first case, one horizontal plate is inserted per two corrugated layers. Hence, the total unit cell height changes from $h+t$ to $h+2t+t_h/2$. It has been proven that under the X_1-direction load, the horizontal plates take most of the strain energy and the contribution of the spline cell walls' bending is negligible. Assume that the horizontal walls have a different thickness t_h, then E_1^* becomes:

$$E_1^* = \frac{t_h}{2h + 4t + t_h} E_s \tag{2.20}$$

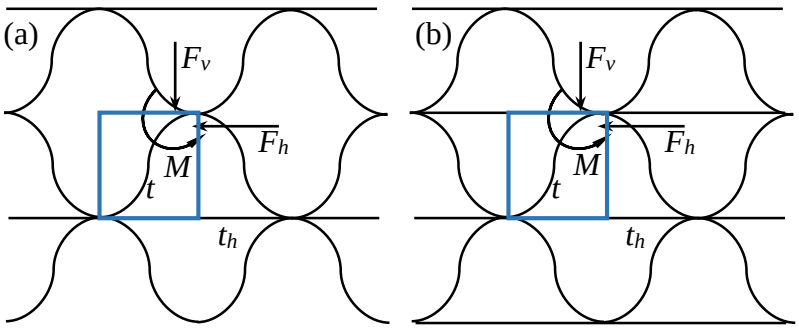

Fig. 2.2. Two typical types of honeycombs with horizontal plates: (a) one plate per two corrugated layers; (b) one plate per corrugated layer.

In this case, v_{12}^* is independent of the horizontal plates, so it can be calculated by Eq. (2.10) with the adjusted total unit cell height. When the whole structure is under a virtual vertical (the X_2-direction) load, both force F_v and force F_h exist at the two ends of the spline cell walls due to the constraint in the X_1-direction caused by the stretching/compressing of the horizontal plates. A relationship between P and F can be found by compatibility condition:

$$\Delta X_1 = \frac{\partial U}{\partial F_h} = -\frac{2F_h l}{E_s t_2} \tag{2.21}$$

Thus, ΔX_2 becomes a function of F_v only, and E_2^* and v_{21}^* can be calculated through Eq. (2.11). Note that the symmetry condition in Eq. (2.12) still holds under this condition. To calculate the modified in-plane shear modulus, strain energy of the horizontal plates needs to be counted in the total strain energy of a unit cell, which is denoted as U':

$$U' = \int_0^1 \left(\frac{\alpha_N N^2}{2} + \frac{\alpha_V V^2}{2} + \frac{\alpha_M M^2}{2}\right)\sqrt{1 + \left(\frac{dX_2}{dX_1}\right)^2}\frac{dX_1}{du}du + \frac{4F^2 l}{E_s t_2} \qquad (2.22)$$

Replacing the $h+t$ term (the original total unit cell height) in Eq. (2.13) and (2.14) with $h+2t+t_h/2$ (the new total unit cell height), the modified G_{12}^* can be determined. The out-of-plane moduli E_3^* and G_{13}^* can be obtained by changing the corresponding unit cell geometries in Eq. (2.15) and (2.17):

$$E_3^* = \frac{E_s(2St + lt_h)}{(2h + 4t + t_h)l} \qquad (2.23)$$

$$G_{13}^* = \frac{2G_s(tl + t_h S)}{(2h + 4t + t_h)S} \qquad (2.24)$$

G_{23}^*, however, is mainly unaffected by the introducing of the flat walls, so Eq. (2.18) with the adjusted total height is applicable here. All other properties, such as the out-of-plane Poisson's ratios, are also remain unchanged.

For the case of Fig. 2.2 (b), one horizontal plate is inserted per one corrugated layer. In the analytical derivation, such condition is equivalent to the honeycomb of Fig. 2.2 (a) with flat walls having twice the thickness. Hence, simply replacing t_h with $2t_h$ in Eq. (2.20) to (2.24) and the total unit cell height yields the desired effective properties.

2.1.5 Boundary Condition: Bonding Strips

Some cellular structures such as hexagonal honeycombs have bonding stripes instead of bonding bonding lines, which is reflected as the flat cell walls between the adjacent junction points in the 2D graph, as shown in Fig. 2.3 (a). In this condition, a flat

cell wall with length d and the same thickness t is added in the unit cell, as shown in Fig. 2.3 (b). The flat wall won't generate strain energy under in-plane axial compression and out-of-plane shear in the X_2-X_3 direction since they are not continuously connected. Thus, simply replacing the original unit cell length l by the new total length $l+d$ in Eq. (2.10), (2.11), (2.15) and (2.18) can provide the corresponding modified properties. The properties that involve strain energy generated by the flat cell walls are G_{12}^* and G_{13}^*. For G_{12}^*, the rotation and bending of the flat cell wall is the main mechanism of the unit cell deformation. Therefore, M_0 in Eq. (2.5) needs to be replaced by the moment generated on the flat cell wall, $F_v d/2$. The moment M about the axis of an arbitrary section of the curved segment becomes:

$$M' = \frac{F_v d}{l} X_1 - \frac{F_v d}{2} \tag{2.25}$$

Through the same process shown in Eq. (2.5) to (2.9) and set $F_h=0$, the deflection ΔX_2 can be calculated. Following the process provided in Gibson and Ashby's model the modified G_{12}^* becomes:

$$G_{12}^* = \frac{F_v E_s t^3 (l+d)\sqrt{h^2+l^2}}{hd\left(E_s t^3 \Delta X_2 + 2F_v d^2\sqrt{h^2+l^2}\right)} \tag{2.26}$$

The modified G_{13}^* can be obtained by the same method used in Eq. (2.17) by adding the flat segment:

$$G_{13}^* = \frac{G_s t(2l^2+d^2)}{2h(l+d)S} \tag{2.27}$$

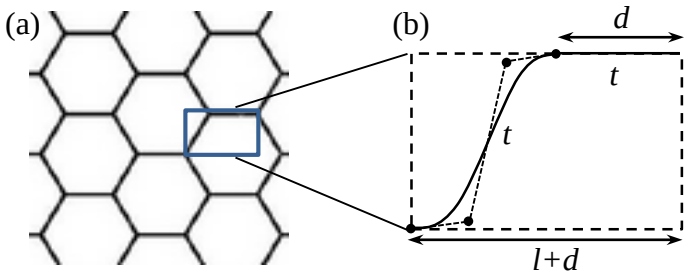

Fig. 2.3. (a) Honeycomb with bonding strips instead of bonding lines and (b) its unit cell.

2.2 Verification

According to the analytical model derived in the previous section, the in-plane moduli are very sensitive to the specific shape of the spline cell walls, whereas the out-of-plane moduli are less shape-dependent and directly determined by the total length S of the spline curve obtained from the integral in Eq. (2.16). Hence, the in-plane moduli are used as the indicators to verify the derived homogenization model in the following two subsections.

2.2.1 Analytical Verification

To verify the analytical models, the derived effective in-plane moduli are calculated for three different unit cell geometries, and the effective stiffness under varied unit cell length to height ratios are compared with those calculated from the existing accepted analytical models.

The first case is the regular hexagonal honeycombs. In this case, the spline cell walls are shaped as straight lines by setting $a=0$ and a flat cell wall (bonding stripe) is added in the unit cell. E_1^*, E_2^* and G_{12}^* obtained from the present analytical model and the classical cell wall bending model [1] are compared in Fig. 2.4 in logarithmic scale. The second geometry is a sinusoidal honeycomb with horizontal plates. In this case, the shape parameter a is set as 9/25 for close approximation of a sinusoidal curve. The spline curve model results are compared with the results from Qiao and Wang [37]. Only E_2^* and G_{12}^* are compared Fig. 2.5, since Eq. (2.20) shows that E_1^* is nearly independent of the curved cell walls. The curve pairs in Fig. 2.4 and Fig. 2.5 show excellent agreement. The average differences of each modulus before taking logarithm are less than 2%. This result proves that the Bezier spline unit cells are capable of describing honeycombs with those 2-D geometries.

In the third geometry, a slim unit cell is built to approximate a monolithic bulk. In this case, the tangent direction of the spline curve at its middle point is made vertical by setting $a=1$. In Fig. 2.6, the unit cell height h is remained constant. Unit cell length l is used as x-axis and the ratio of E_s/ E_2^* is used as the y-axis. The cross point of the two dashed lines marks where the unit cell length equals to the cell wall thickness ($l=t$) while $E_2^*=E_s$, in other words, the ideal solid with elastic modulus of E_s. The figure shows that the predicted curve almost passes through the cross point. Considering the round corner at the top and bottom ends, the plot shows that the spline unit cell is also capable of describing such extreme condition.

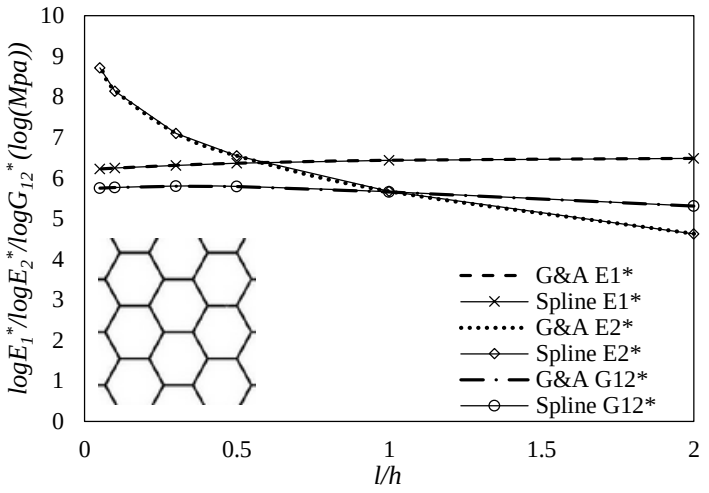

Fig. 2.4. Effective in-plane elastic and shear moduli of hexagonal honeycombs that are calculated by Gibson and Ashby's model and the Spline curve model.

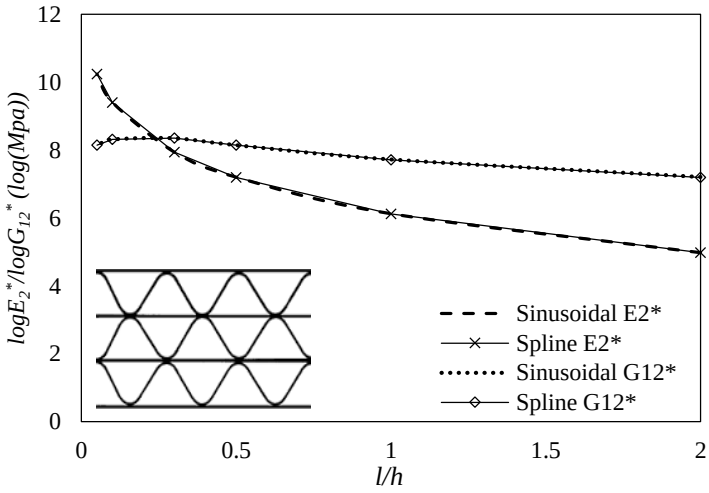

Fig. 2.5. Effective in-plane transverse elastic and shear moduli of sinusoidal honeycombs that are calculated by Qiao and Wang's model and the Spline curve model.

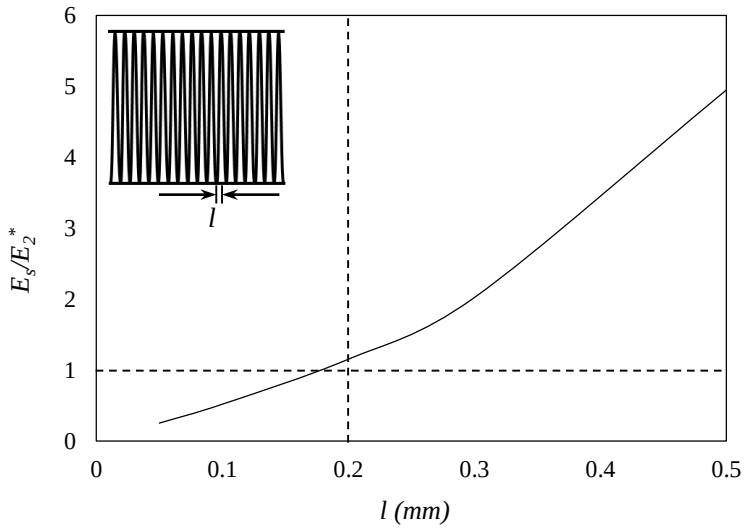

Fig. 2.6. E_s/E_2^* versus unit cell length *l*.

2.2.2 Experimental Verification

Fig. 2.7 shows the spline honeycomb specimens fabricated by 3D printing (EOS P 396 selective laser sintering printer, EOS of North America Inc, Novi, MI) from nylon powders. These specimens have unit cell geometry of *l=h=16mm, t=0.7mm* and three shape parameters *a=0.3, a=0.5* and *a=0.7* from left to right, each one has two replicates, which are labeled as specimen A and B in the following charts. To ensure the junctions are strong enough to hold the cell walls together, the geometry in these locations was adjusted. As a result, the bendable segment was shortened, which was considered in the calculation of analytical solutions. To obtain the printed solid material's elastic properties, compression tests in three printing directions were conducted on solid cubic specimens printed in the same batch. The tests results gave a nearly isotropic stiffness matrix with an average elastic modulus of 943 MPa. Due to surface roughness caused by the sintering

process, the real working thickness of the cell walls is to some degree smaller than the design thickness. To evaluate the working thickness, in-plane compression tests were conducted on a regular hexagonal honeycomb specimen, and the results were substituted into Gibson and Ashby's honeycomb model to calculate the equivalent thickness. It showed that for the design thickness of 1mm, the actual working thickness is 0.64 mm.

The in-plane compression tests of the spline honeycomb in the X_1 and X_2 directions were carried out following ASTM C364/C364M standard test for sandwich core edgewise properties. According to the standard, a special fixture as shown in Fig. 2.8 was made to constrain the flatwise deflection of the honeycomb. The contacting surfaces of the fixture were polished to reduce lateral friction. The tests were performed on a MTS Insight screw driven mechanical test machine with a load cell of 2kN. The head displacement rate was 0.5mm/min, as suggested in the ASTM standards.

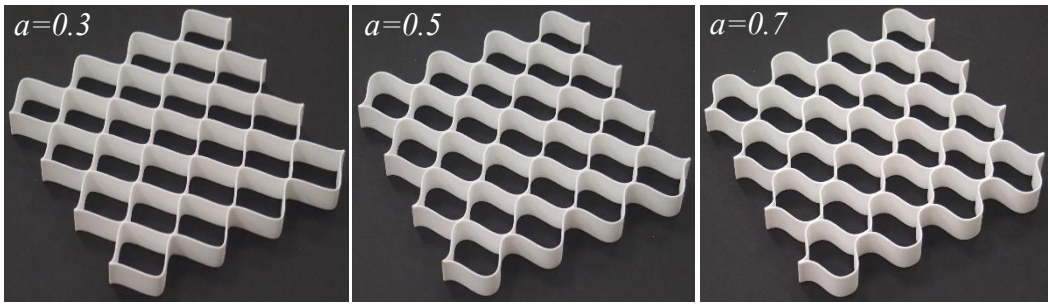

Fig. 2.7. 3D Printed spline honeycomb specimens with shape parameter *a*=0.3, 0.5 and 0.7 from left to right.

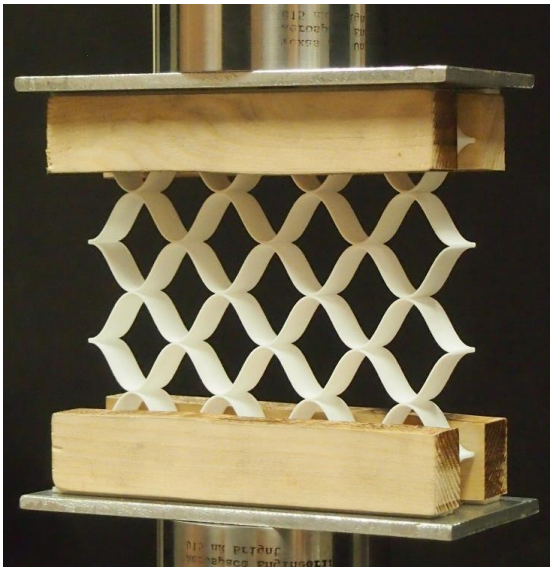

Fig. 2.8. Fixture set for edgewise compression test of honeycomb sandwich cores.

The experimental and the analytical results are plotted in Fig. 2.9. It can be seen that the analytical results marked with squares and triangles are in well agreement with the experimental results marked with crosses. There are two possible reasons for the differences: the adjusted junction geometry on the specimens and the relatively large thickness-length ratio of the specimen cell walls. First order bending theory is used in the analytical model because cell wall thickness is assumed to be negligible, but the specimens' relatively large thickness will reduce the accuracy of such model. Real honeycomb products usually have a thickness-to-length ratio less than 1/20, which is closer to the solution of the first order bending analysis.

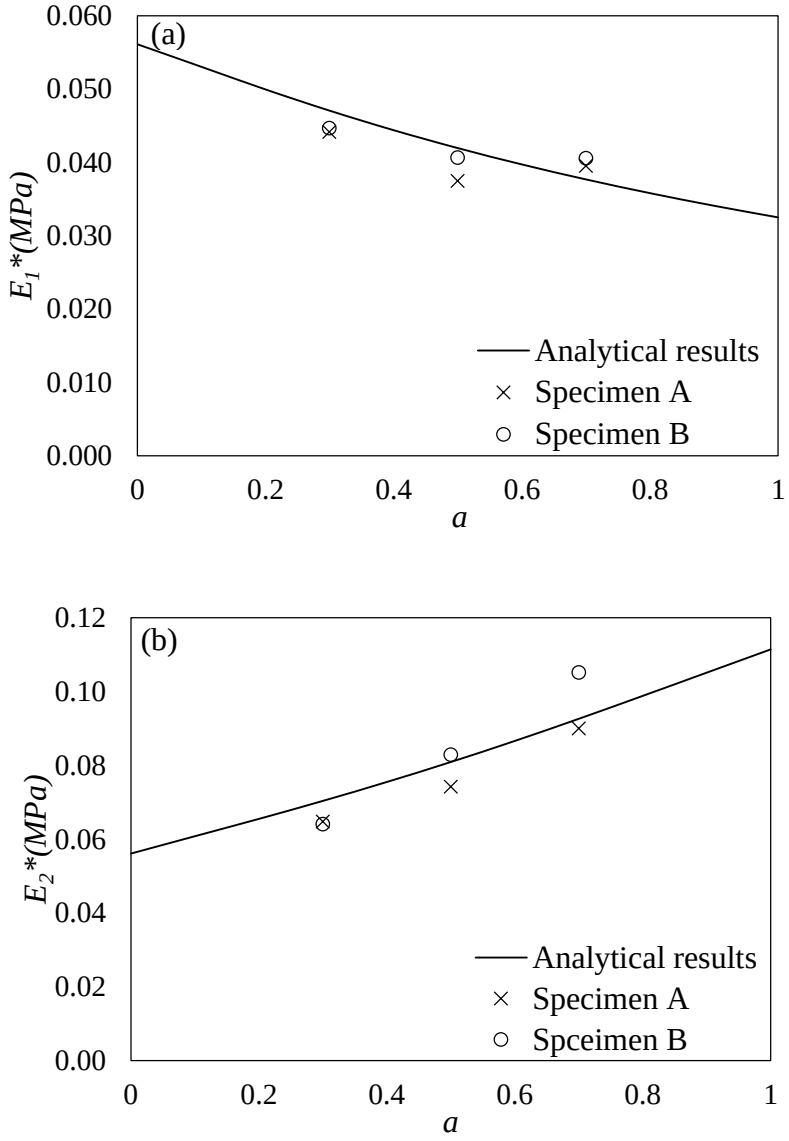

Fig. 2.9. Graphical comparison of experimental and analytical in-plane elastic moduli: (a) E_1^*; (b) E_2^*.

2.3 Parametric Study and Discussions

2.3.1 FEA Models

It has been verified via commercial finite element code Abaqus that a quarter of the smallest repetitive unit (Fig. 2.10) with proper boundary conditions can accurately represent the mechanical behaviors of the corresponding infinite periodic honeycomb panel. Therefore, a 4-point Bezier curve unit cell is built and tested in Abaqus to reduce the computational cost. To investigate the effect of spline geometry on the effective properties, the spline shape parameter a is varied from 0 to 1 at an interval of 0.1 under three unit cell aspect ratios: $l/h=0.5$, $l/h=1$ and $l/h=2$, as shown Fig. 2.11. Horizontal plates or flat cell walls are not modeled in order to focus on the effect of spline geometry. For the same reason stated previously, the in-plane moduli under different unit cell geometries are investigated in the first subsection. In the second subsection, the out-of-plane buckling resistance of spline cell walls are investigated, and the empirical functions were derived based on the results. Linear shell element S4 is used to mesh the part subjected to in-plane compression loads, and quadratic shell element S8R is used to mesh the part for out-of-plane buckling tests. The mesh size is determined by convergence studies conducted under the two loads.

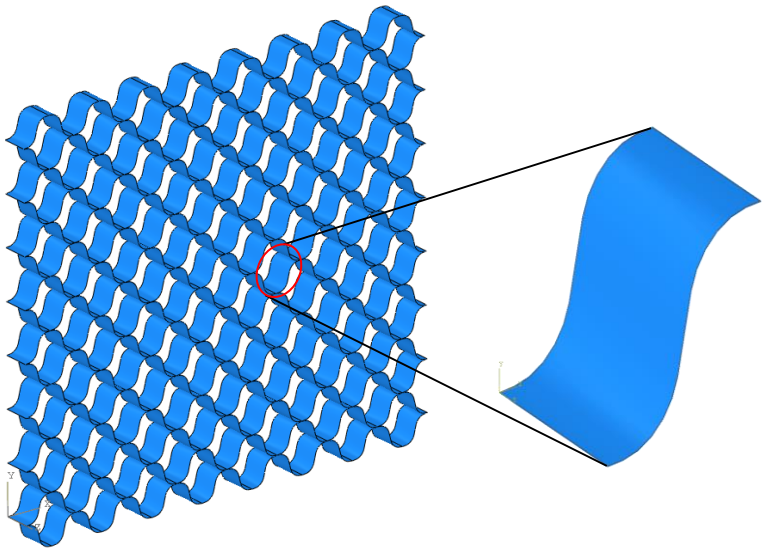

Fig. 2.10. Finite element unit cell selected from a honeycomb with spline cell walls.

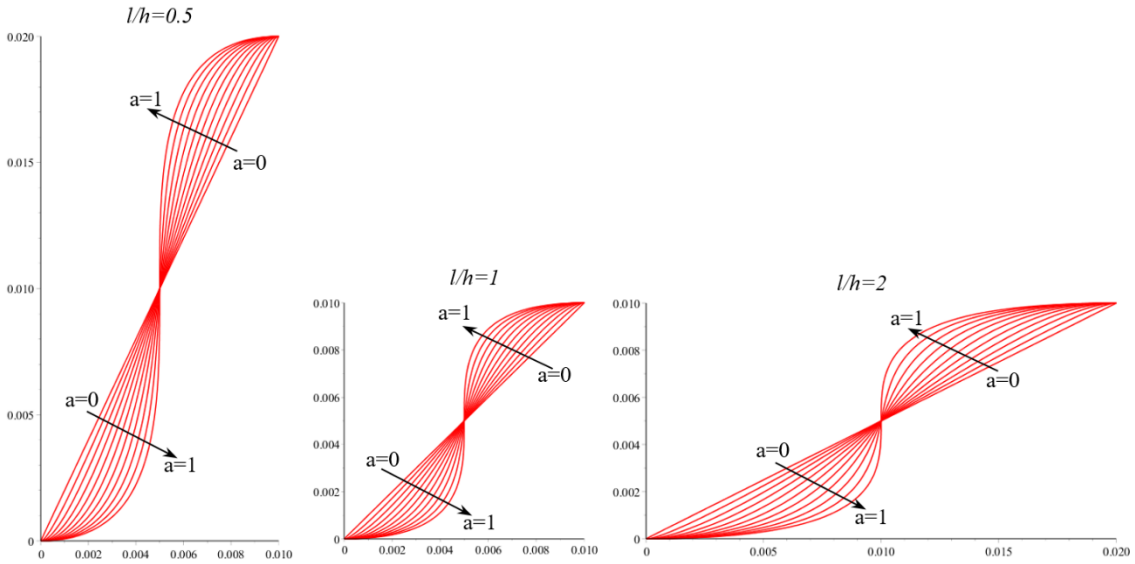

Fig. 2.11. The three unit cell aspect ratios with varying spline shape parameters built in the finite element models.

2.3.2 In-plane Stiffness

The effect of changing spline cell wall shape on the effective in-plane elastic moduli E_1^* and E_2^* are investigated and discussed in this subsection. To simulate the boundary condition in a honeycomb, the two ends of the cell walls are free to translate but constraint from rotation. Horizontal plates or flat cell walls are not modeled here in order to focus on the effect of spline geometry. The effective moduli are evaluated by substituting the displacements and the applied quasi-static load extracted from the two ends of the unit cell into Eq. (2.10) and (2.11). In Fig. 2.12, the numerical and analytical in-plane moduli E_1^*, E_2^* of the three unit cell aspect ratios are normalized by $Es{\cdot}\rho$, where ρ is the relative density of the cellular structure:

$$\rho = \frac{S}{(h + t_1)l} \tag{2.28}$$

By this way the plotted curves are material-less and weight-normalized. It is obvious that the analytical and numerical results of E_1^* and E_2^* are in good agreements with a maximum difference of 2.3%, which further verified the analytical model. For all of the three aspect ratios, the normalized effective modulus E_1^* decreases as the shape parameter a increases (Fig. 2.12 (a), (b), (c)), thus a straight cell wall is preferred to obtain a higher material efficiency. Nevertheless, the normalized E_2^* curves exhibit different patterns. In Fig. 2.12 (d), the normalized E_2^* increases monotonically as a increases; in Fig. 2.12 (e) and (f), however, the maximums are found at $a=0.752$ and $a=0.445$ respectively. These peak values could be utilized as the optimization strategies for higher specific E_2^*, but it will cause a reduced specific E_1^*.

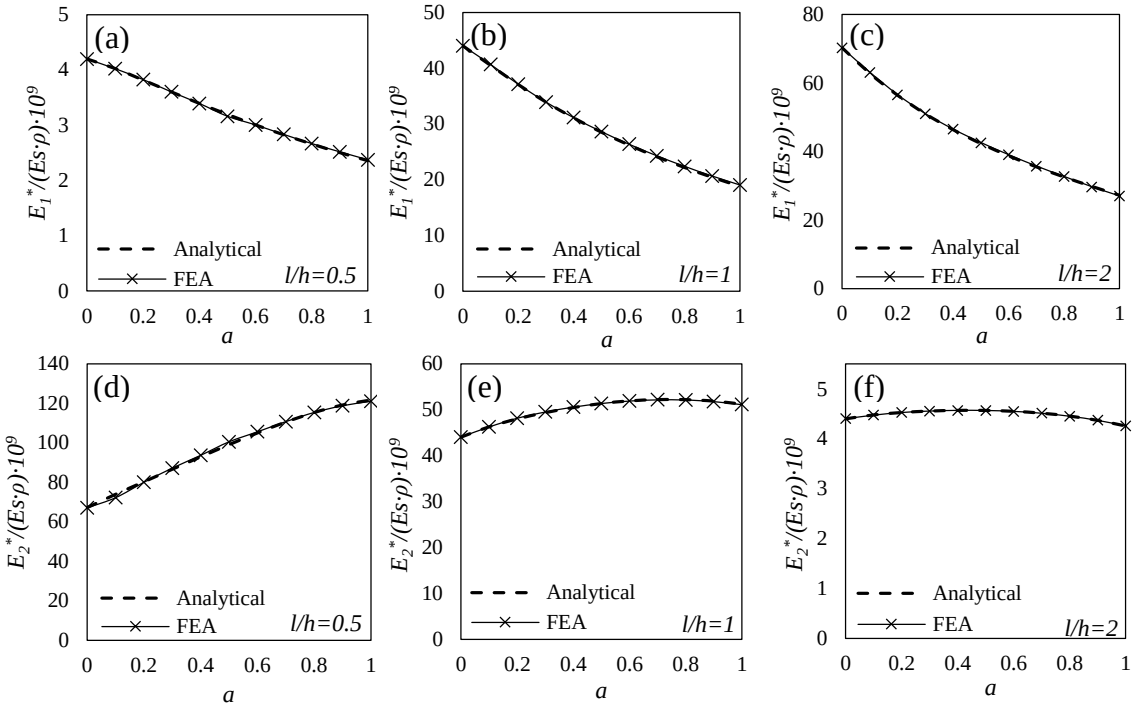

Fig. 2.12. Normalized effective in-plane moduli versus spline shape parameter under the three unit cell aspect ratios

2.3.3 Out-of-plane Stability

Only the first eigenmodes (smallest rational eigenvalue) are analyzed to calculate the critical force. By observing the buckling shape of a large spline honeycomb panel, the spline cell walls are considered to be clamped at all edges. The effective critical stress σ_{3cr}^{*} is calculated from the critical force F_{cr} by the following equation:

$$\sigma_{3cr}^{*} = \frac{F_{cr}}{(h + t_1)l} \tag{2.29}$$

In order to compare the specific critical buckling stress of different cell wall shapes, the above critical stress needs to be normalized by the corresponding relative density of the honeycomb:

$$\sigma_{3cr}^{*}|specific = \frac{\sigma_{3cr}^{*}}{\rho} = \frac{\sigma_{3cr}^{*}}{S\dfrac{1}{(h+t_1)l}} = \frac{F_{cr}}{S} \tag{2.30}$$

Hence the *Fcr/S* calculated from the simulation results and S calculated from Eq. (2.16) are plotted and compared in Fig. 2.13. Obviously, increasing the waviness of spline cell walls brings substantial increase in the out-of-plane buckling resistance, but the trends are quite irregular for different unit cell aspect ratios. For *l/h*=0.5 and *l/h*=1, the normalized buckling stresses increase monotonically with *a*; for *l/h*=2, the curve shows a maximum around a=0.8.

To analyze the associated mechanisms, their first eigen buckling shapes of selected *a* values are illustrated in Fig. 2.14. The corresponding *a* values are marked in Fig. 2.13 by dashed vertical lines. The colored contours in Fig. 2.13 represent the displacement field. It is obvious that the buckling mode is closely related to the length of the relatively flat segment on the spline cell walls. In the case of *l/h=0.5*, the bulge shape changes continuously as the cell wall becomes curvier, so its *Fcr/S-a* curve in Fig. 2.13 increases steadily. The buckling mode of *l/h=1* altered at *a=0.7* from one half-wave to two half-waves as the flat segment becomes narrow. For this reason, the slope of the *Fcr/S-a* curve with *l/h=1* has a more significant change. The *Fcr/S-a* curve of *l/h=2*, different from the other two, shows a maximum value around *a=0.8*. From Fig. 2.14 it can be seen that at this *a* value, the buckling region shifts from the middle area to one end (the

eigenvalues for buckling to occur on either of the two ends are the same), where the longer flat segment exists. Hence, it can be summarized that to maximize the out-of-plane buckling resistance the spline cell walls should have large curvature and avoid continuous flat segment.

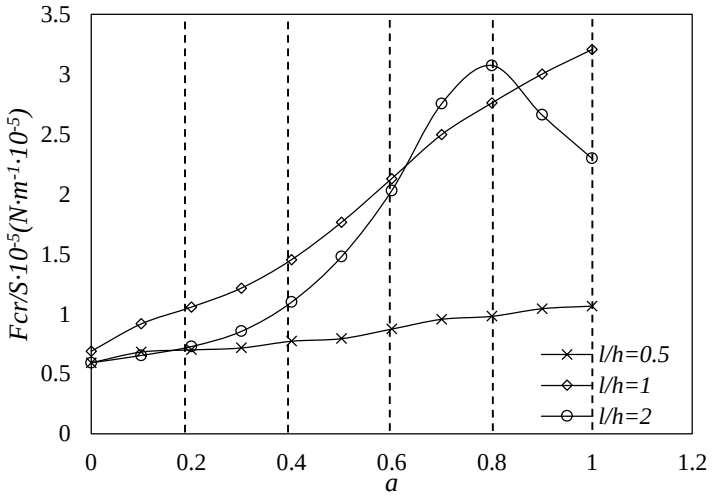

Fig. 2.13. Specific out-of-plane buckling stress versus spline shape parameter under the three unit cell aspect.

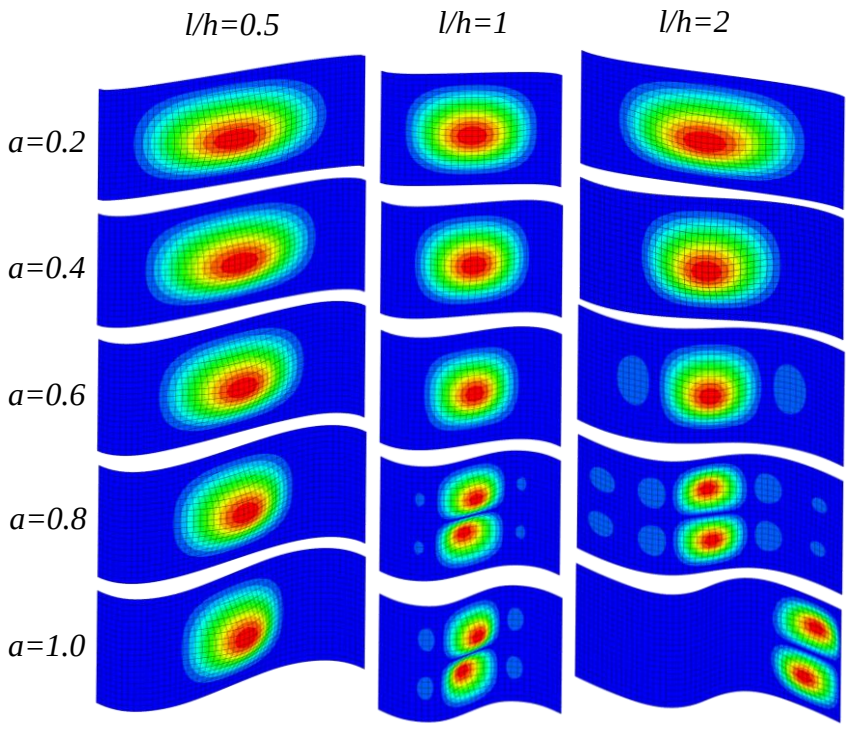

Fig. 2.14. First buckling modes of spline cell walls with selected shape parameters under three aspect ratios.

2.4 Conclusions

In this part of work, Bezier spline curve functions are used to model the elastic properties for a wide range of 2-D periodic structures with nonlinear cell walls. The effective orthotropic stiffness matrix of the primary spline honeycombs is derived via strain energy method, and a shape parameter *a* is assigned as an indicator of the extent of the cell walls' undulation. Based on this outcome, the analytical solutions for spline honeycombs with continuous horizontal plates or bonding strips are subsequently derived by properly modifying the original solutions. Analytical, experimental and numerical

verifications show that the presented method can precisely predict the in-plane mechanical properties of several honeycomb structures having a wide range of unit cell geometries.

Parametric studies are performed by finite element simulations to examine the influence of the spline cell wall shape geometry on its effective in-plane elastic moduli and out-of-plane stability. Results show that as the spline cell wall becomes curvier, the effective specific elastic modulus E_1^* become smaller. The specific E_2^*, however, shows different pattern of change under different unit cell aspect ratios. For l/h=0.5, The specific E_2^* increases monotonically with the spline shape parameter a; for $l/h=1$ and $l/h=2$, maximum specific E_2^* are found at a=0.752 and a=0.445 respectively. This result shows that the developed model can be used for property optimization. Parametric study of the out-of-plane stability of the spline cell walls shows that the buckling force is largely determined by the distribution of the cell walls' curvature—buckling a relative long segment of cell wall with small curvature is more prone to buckling, and the buckling mode depends on the length of this segment. In order to maximize the out-of-plane stability, the spline cell walls should have continuous high curvature or approximately equal-length segments with low curvature.

3. HONEYCOMBS WITH LAMINATED COMPOSITE CELL WALLS

3.1 Analytical Modeling

Although many new methods have been developed to obtain analytical homogenization of honeycombs, Gibson and Ashby's fundamental honeycomb model has never been significantly challenged. Considering the accuracy and the corresponding computational cost, their model is still the most efficient one for thin-wall honeycombs [1]. Therefore, the homogenized stiffness matrix of composite cell wall honeycombs is derived by combining Gibson and Ashby's model and the classic laminated plate theory (CLPT) model. Solutions for the general case honeycomb with *n*-layer composite cell walls are presented.

3.1.1 In-plane Elastic Moduli

According to Gibson and Ashby's model, the normal stress in the cell walls can be approximated to zero, hence the overall in-plane deformation of honeycombs becomes the accumulation of cell wall bending deflections as depicted in Fig. 3.1. Due to symmetry of the unit cell, the deflection angles at the two ends must be zero, which leads to a moment M_0 at these locations. With the above boundary conditions, the effective in-plane elastic moduli E_1^* and E_2^* are given by Gibson and Ashby's model as:

$$E_1^* = \frac{12cos\theta E_s I}{(h + lsin\theta)l^2 sin^2\theta},$$

$$E_2^* = \frac{12(h + lsin\theta)E_sI}{l^4cos^3\theta} \tag{3.1}$$

where h, l and θ are the unit cell geometry parameters as shown in Fig. 3.1, E_s is the elastic modulus of the solid material used as the cell walls and I is the moment of inertia of the cell walls.

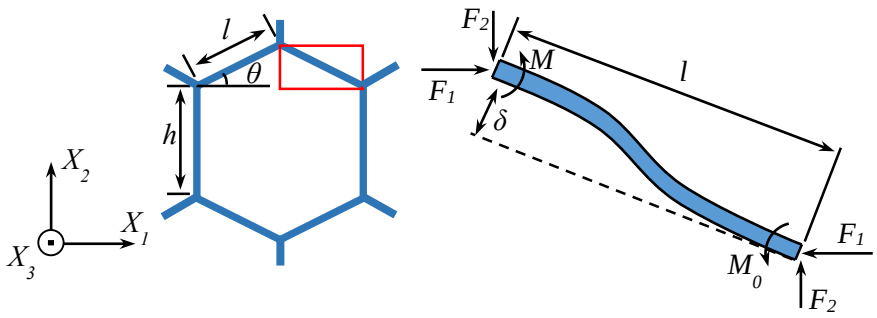

Fig. 3.1. The bending mode of the inclined cell walls when the honeycomb is subjected to uniform in-plane compression.

For honeycombs with laminated cell walls, the macroscopic geometry parameters h, l and θ remain unchanged, but the flexural rigidity E_sI must be replaced by the corresponding effective parameter of the laminated cell walls. Thus, CLPT is introduced. Note that X_1, X_2 and X_3 in Fig. 3.1 are the global honeycomb coordinate; x, y and z in Fig. 3.2 are the local cell wall coordinate. By applying CLPT, the bending moment M and longitudinal force N of a composite beam are:

$$M = B\varepsilon_x + D\frac{d^2w}{dx^2}, \quad N = A\varepsilon_x + B\frac{d^2w}{dx^2} \tag{3.2}$$

where w represents the beam deflection as a function of x and ε_x is the mid-plane strain along the longitudinal direction. A, B and D are extensional stiffness, coupling stiffness

and bending stiffness respectively, which are determined by the cell wall's ply arrangement:

$$A = \sum_{i=1}^{n} E_{si}(z_i - z_{i-1}),$$

$$B = \frac{1}{2}\sum_{i=1}^{n} E_{si}({z_i}^2 - {z_{i-1}}^2),$$

$$D = \frac{1}{3}\sum_{i=1}^{n} E_{si}({z_i}^3 - {z_{i-1}}^3) \tag{3.3}$$

where E_{si} is the elastic modulus of the *ith* ply. Fig. 3.2 illustrates the cross section of an *n*-layer composite cell wall, where t_i is the thickness of *ith* ply and z_i is the distance from the cell wall bottom surface to the interface of *ith* and (i+1)th layer. Due to the assumption of no normal cell wall stress, we set N=0, then Eq. (3.2) gives the moment at arbitrary cross section:

$$M = \left(D - \frac{B^2}{A}\right)\frac{d^2y}{dx^2} \tag{3.4}$$

Hence $(D\text{-}B^2/A)$ is the effective flexural rigidity. The effective in-plane elastic moduli ${E_1}^*$ and ${E_2}^*$ can then be expressed as:

$${E_1}^* = \frac{12cos\theta}{(h + lsin\theta)l^2sin^2\theta}\left(D - \frac{B^2}{A}\right)$$

$${E_2}^* = \frac{12(h + lsin\theta)}{l^4cos^3\theta}\left(D - \frac{B^2}{A}\right) \tag{3.5}$$

It can be shown by simple calculation that for regular hexagonal honeycombs with θ=30° and h=l, Eq. (3.5) gives identical solution for ${E_1}^*$ and ${E_2}^*$.

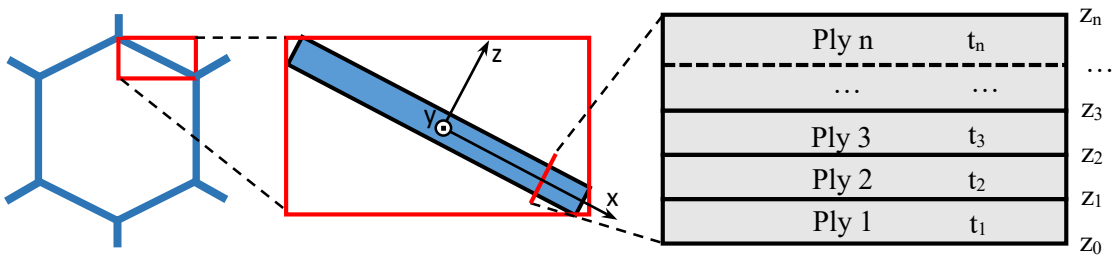

Fig. 3.2. Cross section of an n-layer laminated composite honeycomb cell wall.

3.1.2 In-plane Shear Modulus

The in-plane shear deformation is more complicated for it contains twisting and bending of cell walls in all directions. The local shear deflection in a unit cell is given by:

$$\delta_v = \frac{2\tau_{12} lbcos\theta}{3E_s I} \cdot \left(\frac{h}{2}\right)^3 + \frac{\tau_{12} l^2 h^2 bcos\theta}{24(E_s I)} \tag{3.6}$$

The first and second term are the contributions of the cell walls' bending and torsion respectively. Due to the different cell wall thickness the flexural rigidity E_sI in the two terms are different. Hence the effective in-plane shear modulus becomes:

$$G_{12}^* = \frac{\tau_{12}}{\gamma_{12}} = \frac{12(h + lsin\theta)}{lh^2 cos\theta} \cdot \frac{2K_s K_d}{lK_d + 2hK_s} \tag{3.7}$$

where K_s and K_d are the effective flexural rigidity $(D\text{-}B^2/A)$ of the single and double thickness cell walls respectively.

3.1.3 Out-of-plane Elastic Modulus

The out-of-plane linear elastic deformation of honeycombs is independent of the unit cell geometry and can be simply derived by Voigt and Reuss's upper bound:

$$E_3^* = \sum_{i=1}^{n} f_i \, E_{si} \tag{3.8}$$

3.1.4 Out-of-plane Shear Moduli

When the honeycomb is subjected to out-of-plane shear load, the cell walls undergo both r and bending deformation. It has been observed that the majority of the total strain energy is stored in the shear deformation of the cell walls that have non-zero projection on the load directions. Thus, the double-thickness cell walls have no influence on G_{13}^*, which is:

$$G_{13}^* = \frac{cos\theta}{lsin\theta + h} \sum_{i=1}^{n} G_{si} t_i \tag{3.9}$$

where G_{si} is the shear modulus of the *ith* ply. For G_{23}^*, Gibson and Ashby's model provided two solutions as the upper and lower bounds. These two bounds have different values in general case but coincide when the unit cells are regular hexagons. The general solution of the upper and lower bounds of G_{23}^* are:

$$G_{23,upper}^* \leq \frac{(h + lsin^2\theta)}{(h + lsin\theta) lcos\theta} \sum_{i=1}^{n} G_{si} t_i,$$

$$G_{23,lower}^* \geq \frac{(2h + lsin\theta)^2}{(lsin\theta + h) lcos\theta (4h + l)} \sum_{k=1}^{n} G_{si} t_i \tag{3.10}$$

From M. Grediac's work [28], the exact value of G_{23}^* can be expressed by an empirical formula:

$$G_{23}^{*} = G_{23,lower}^{*} + \frac{0.787}{b/l}\left(G_{23,upper}^{*} - G_{23,lower}^{*}\right) \tag{3.11}$$

3.1.5 Poisson's Ratios

From Gibson and Ashby's model, the in-plane Poisson's ratios of honeycombs are material-independent and only related to the geometry of the unit cell:

$$v_{12}^{*} = \frac{cos^2\,\theta}{\left(\frac{h}{l} + sin\,\theta\right) sin\,\theta},$$

$$v_{21}^{*} = \frac{\left(\frac{h}{l} + sin\,\theta\right) sin\,\theta}{cos^2\,\theta} \tag{3.12}$$

For regular hexagonal honeycombs, both in-plane Poisson's ratios equal to 1. The out-of-plane Poisson's ratios, on the contrary, are independent of the unit cell geometry:

$$v_{31}^{*} = v_{32}^{*} = \frac{\sum_{i=1}^{n} E_i t_i}{\sum_{i=1}^{n} v_i E_i t_i}.$$

$$v_{13}^{*} \approx 0,\ v_{23}^{*} \approx 0 \tag{3.13}$$

As presented above, all of the parameters that describe the linear elastic response of the honeycomb with multi-layered cell walls are derived.

3.2 Numerical Modeling

Commercial finite element code Abaqus Standard is employed to verify the analytical homogenization model and conduct a parametric study. A full detailed

honeycomb model with double-layer cell walls (four layers in the bonded cell walls) as shown in Fig. 3.3 is built in the FE code. The model has 11×9 hexagonal cells, as shown in Fig. 3.4 (a). In the parametric study, three E_{s1}-E_{s2} combinations—200 GPa-2 GPa, 200 GPa-50 GPa and 200 GPa-100 GPa—are assigned to the two plies with varying t_1-t_2 ratio are varied under each E_{s1}-E_{s2} combination. To avoid the influence of geometry change, the total cell wall thickness ($t=t_1+t_2$) is remained constant, and t_1 is varied from 0 mm to 1 mm a step size of 0.1 mm, which means t_2 is simultaneously varied from 1 mm to 0 mm. The cell wall length, width (the dimension in the X_3 direction) and total thickness (for the inclined cell walls) are 10 mm, 20 mm and 1mm respectively. S4R shell elements is used to build the cell walls due to their accuracy and efficiency in solving bending and shear problems. For comparison, a homogeneous cuboid model with the same overall dimensions of the full detailed honeycomb model are built by C3D8R brick elements as shown in Fig. 3.4 (b), and the effective properties calculated from the above E_{s1}, E_{s2} t_1, t_2 values through the derived analytical model are assigned to the corresponding cuboid models.

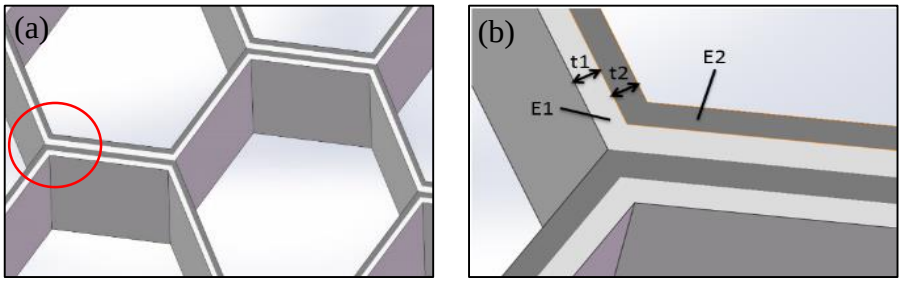

Fig. 3.3. (a) Honeycomb with double-layer cell walls. (b) Ply arrangement in junction area.

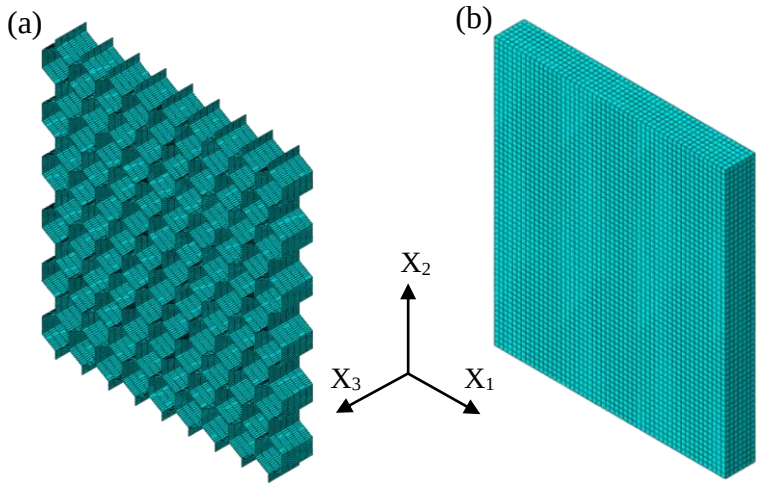

Fig. 3.4. FE models built for verification and parametric study. (a) Full detailed honeycomb model with composite shell elements; (b) cuboid model with calculated effective properties.

Six types of loads—uniaxial compression in the X_1, X_2 and X_3 directions and shear in the X_1-X_2, X_2-X_3, X_3-X_1 directions—are applied on both models. The compression and shear loads are applied by coupling the translational degrees of freedom (DOF) of the nodes on the loading side to a reference point, and the translational DOFs of the nodes on the other side of the honeycomb/cuboid model are fixed. Under each of the 6 load cases, the displacement of the reference point is set to a constant in all of the 33 ply arrangements, and the reaction forces on the reference points are extracted as the indication of the two models' stiffness, which are plotted and compared in each subsection below.

3.3 Result and Discussion

3.3.1 In-plane Mechanical Behaviors

The simulation results discussed in this section are uniaxial compression applied in the X_1 and X_2 directions. The reaction forces of different cell walls are normalized by the force generated from the full detailed model with E_{s2}=2 GPa, t_1=0, t=t_2=1 mm. The normalized forces are denoted as F_{1n}, F_{2n}, F_{12n}, etc. The resulting curves are plotted in Fig. 3.5 (a) and Fig. 3.6 (a). The three intercepts at the left end of the chart represent the force obtained from E_{s2}= 2 GPa, E_{s2}= 50 GPa and E_{s2}= 100 GPa from low to high, and the converged intercept at the right end stands for the result of the cell walls with t=t_1 and E_{s1}=200 GPa.

The F_{1n}-t_1 (Fig. 3.5) and F_{2n}-t_1 (Fig. 3.6) curves obtained from the full detailed models and the cuboid models show excellent agreement with each other with an average percentage difference of 1.63% and 1.42% respectively. The curve shapes in Fig. 3.5 and Fig. 3.6 are alike, as Eq. (3.6) predicted. While E_{s1}=200 GPa and E_{s2}=2 GPa, the F_{1n}-t_1 and F_{2n}-t_1 curves behaves like a quadratic function, when E_{s2}=50 GPa, the curves transform to an "S" shape. With this shape, there is a "flat zone" (t_1=0.2~0.4mm) where the slop of the curve is nearly zero. When E_{s2} increases to 100GPa, the flat zone moves rightward to t_1=0.3~0.5 mm. Within this flat zone region, thickening the stiffer ply brings almost no benefit to the whole structure's effective stiffness. Fig. 3.5 (b) and Fig. 3.6 (b) illustrate the von Mises stress distribution of the deformed full detailed honeycomb models

with E_{s1}=200 GPa, E_{s2}=2 GPa, t_1=t_2=0.5 mm (which is the default in all of the following figures). For both load cases, the stress contours show clearly that the stress on the inclined cell walls is significantly larger than that in the vertical cell walls, which supports the assumption made earlier that the bending of the inclined cell walls is the dominant deformation. Boundary effect has also been observed on the model: the von Mises stress on the outside of the structure is higher than that on the inner region, which could be the reason for the slight difference between the results of the full detailed and the cuboid models.

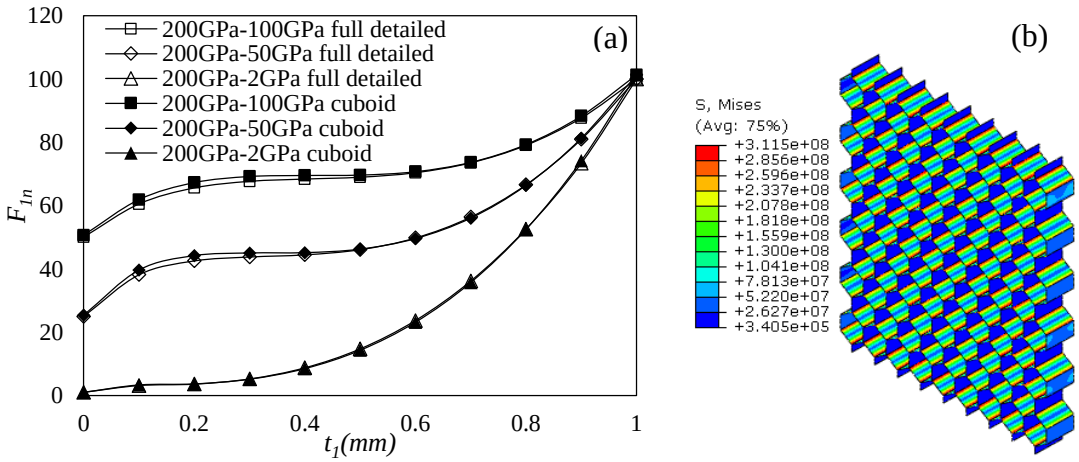

Fig. 3.5. (a) F_{1n}-t_1 response of X_1 uniaxial compression. (b) Stress contour of the deformed full detailed model

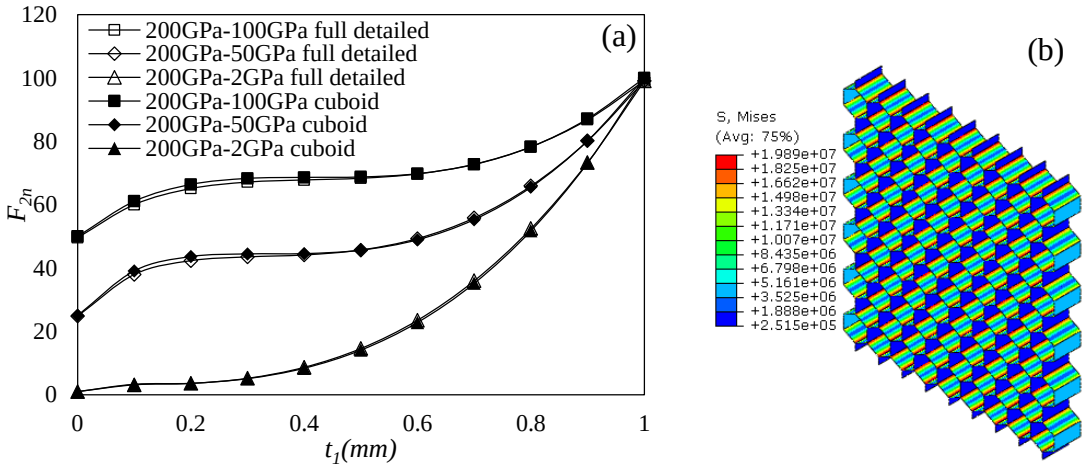

Fig. 3.6. (a) F_{2n}-t_2 response of X_2 uniaxial compression. (b) Stress contour of the deformed full detailed model

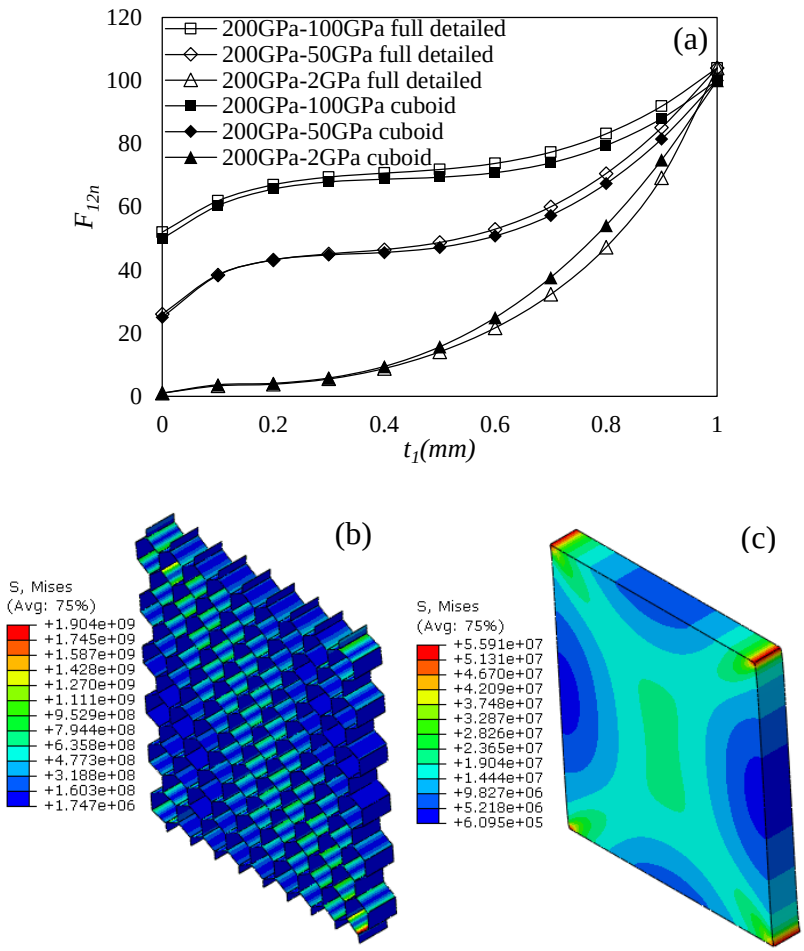

Fig. 3.7. (a) F_{12n}-t_1 response of X_1-X_2 shear. (b) Stress contour of the deformed full detailed model (c) Stress contour of the deformed homogenized model

In Fig. 3.7 (a), the F_{12n}-t_1 curves obtained from the X_1-X_2 shear simulations show similar shape to that of the in-plane compression tests. The curves also display flat zones in the same t_1 ranges. In this case, the average difference between the curves of the full detailed and the homogenized models is 5.12%, which is larger than the previous cases but not significant. From the stress contour shown in Fig. 3.7 (b) and (c) it can be seen that

the stress distribution on the full detailed and cuboid models are very similar: cells near the diagonal lines of the models experience higher stress than others.

The flat zones on the curves provide potential benefits in honeycomb design: for in-plane applications where a certain stiffness is required, the desired value of in-plane modulus can be laid in the flat zone by choosing proper E_{s1} and E_{s2} to ease tolerance, accommodate production variation, and make the property stable.

3.3.2 Out-of-plane Mechanical Behaviors

The out-of-plane compression modulus is essentially the Voigt and Reuss's upper bond, so the effective out-of-plane stiffness is proportional to the volume fraction of the ply materials, i.e. the ply thickness fraction in this study. The straight F_{3n}-t_1 response curves of X_3 compression shown in Fig. 3.8 (a) reflect such linearity. The average difference of the curves is as small as 0.73%, which is due to the highly uniform stress distribution in the honeycomb model shown in Fig. 3.8 (b). The curves of the full detailed model under X_1-X_3 and X_2-X_3 shear, however, show slight non-linearity, especially in the E_{s2}=2 GPa curves, as shown in Fig. 3.9 (a) and Fig. 3.10 (a). In Fig. 3.9 (a), the 200 GPa-2 GPa curve of the full detailed model begin firstly goes below the straight line of the cuboid model when t_1 begin to increase from zero, then rise above it. At t_1=0.2 mm, the difference between the two curves reaches its maximum at 34.20%. From the same figure it can be observed that as E_{s2} increases, the non-linearity of the curves diminishes. The

curves in Fig. 3.10 show similar shape change, but in this case F_{23n} of the homogenized model is 5.82% higher than that of the full detailed model.

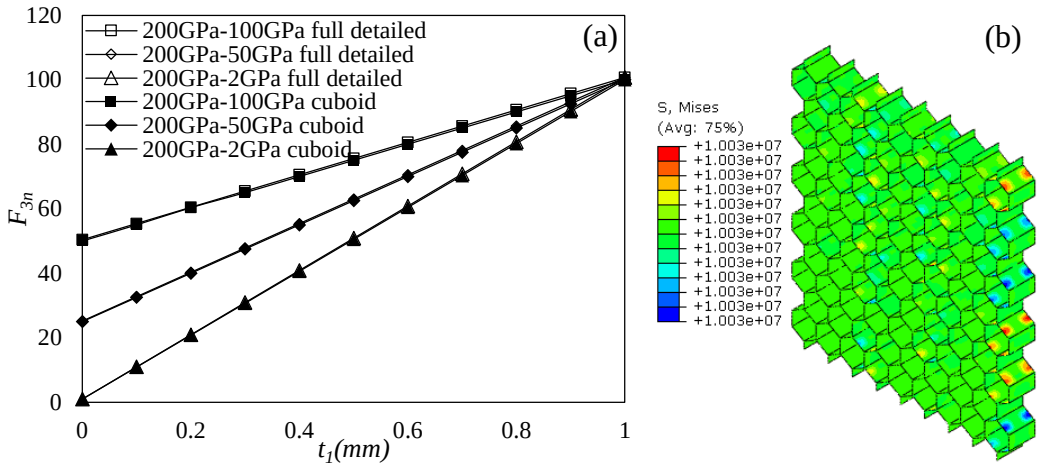

Fig. 3.8. (a) F_{3n}-t_1 response of X_3 compression. (b) Stress contour of the deformed homogenized model

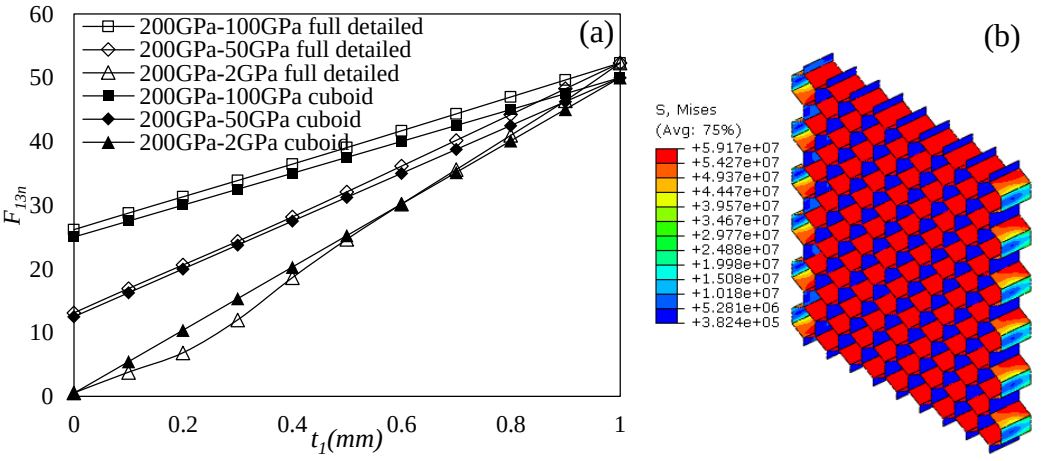

Fig. 3.9. (a) F_{13n}-t_1 response of X_1-X_3 shear. (b) Stress contour of the deformed full detailed model

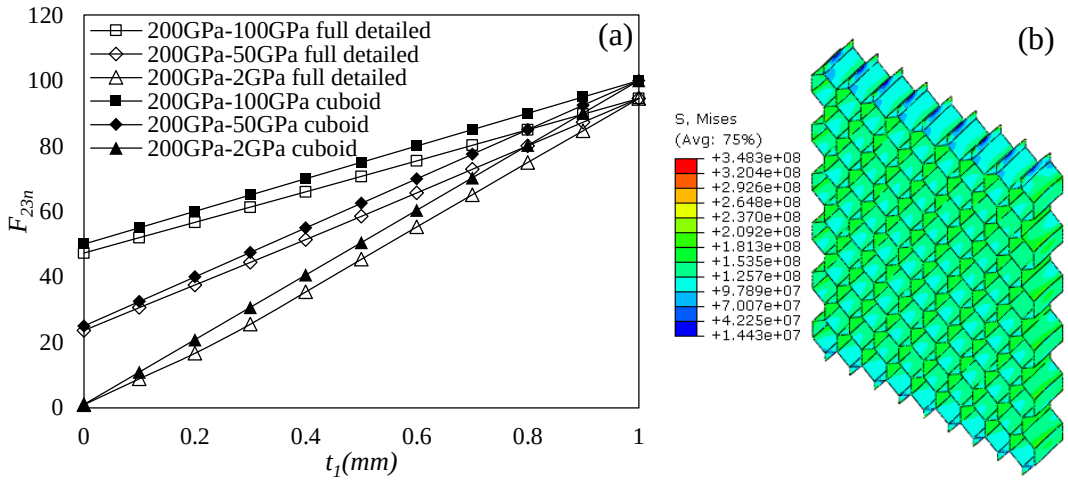

Fig. 3.10. (a) F_{23n}-t_1 response of X_2-X_3 shear. (b) Stress contour of the deformed full detailed model.

The boundary effect of the FE models that is different from the analytical model assumptions is most likely the reason for the differences between the results extracted from the full detailed and cuboid models. It is also believed that the boundary effect is the cause of the non-linearity of the curves under the out-of-plane loading. The resistant force generated from the cell wall bending is not considered in the derivation of G_{13}^*, which made the homogenized models less stiff than the full detailed model in the X_1-X_3 shear loading and affected the linearity between G_{13}^* and the t_1, as shown in Fig. 3.9 (a). Furthermore, the outmost vertical cell walls in the horizontal direction have much higher von Mises stress than the inner vertical cell walls, which led to a larger difference. Fig. 3.10 (b) shows that the outmost cell walls in the vertical direction have a relatively low stress, which reduced the resistant force of the full detailed honeycomb. Thus, the F_{23n}-t_1 curves of the full detailed model fall below those of the cuboid model in Fig. 3.10 (a).

3.4 Conclusions

A comprehensive study of honeycombs with composite cell walls is presented in this part. The analytical homogenization model for general case honeycomb structure with *n*-layer cell walls is derived, and numerical simulations are performed on a full detailed and a homogenized cuboid models to verify the analytical model and investigate the effect of cell wall ply arrangement on the effective moduli. Six load cases, include three compression tests and three shear tests, are applied by displacement boundary conditions. Normalized reaction forces on the loading point are extracted as the indicator of the effective stiffness and plotted for comparison.

The results show that the analytical homogenization model has very good accuracy in predicting the linear elastic response of honeycombs with composite cell walls, and some interesting features are observed. For the in-plane compression and shear tests, the effective stiffness initially increased rapidly as the thickness of the stiffer ply thickens. The curves then entered a flat zone where increasing the thickness of the stiffer ply can hardly improve the effective stiffness. After the flat zone, the curve rises steeply again to its end value at t_1=1 mm. The flat zone is a significant feature that can help stabilizing the effective property of the composite cell wall honeycombs. Its length and location are related to the ratio of E_{s1} and E_{s2}. The larger the difference between E_{s1} and E_{s2}, the shorter and more towards the left the flat zone is. The agreement between the curves of the full detailed and cuboid models under out-of-plane shear is not as good as those of the in-plane responses, but still satisfactory. The average difference between the curves of the two

models under X_1-X_3 and X_2-X_3 shear are relatively large, and the F_{13n}-t_1 and F_{23n}-t_1 curves of the full detailed model showed slight non-linearity at small t_1 and E_{s2} values. Such phenomenon is believed to be the result of the assumed borderless analytical model that is different from the full detailed finite element model, on which boundary effect is observed.

4. HONEYCOMBS WITH PERFORATED CELL WALLS

4.1 Analytical Modeling

4.1.1 Theoretical Considerations

As mentioned in the introduction (Section 1.4), no exact solution has been developed for the bending, twisting and buckling problems of thin plates with large perforations (the perforation-plate length ratio $2R/l > 0.3$), hence the solutions provided in this section are based on the approximate method proposed by the previous authors. The method of homogenization is used in the analytical derivations, which aims to describe the periodic cellular structures as homogeneous orthotropic bulks with the calculated effective moduli and strengths. The effective properties of perforated honeycombs to be analytically modeled in this section are:

In-plane elastic moduli E_1^* and E_2^*;

In-plane shear modulus G_{12}^*;

Out-of-plane critical buckling stress σ_{3cr}^*;

The same geometry parameter assignment and the global and local coordinates used in the previous part (Fig. 3.1 and Fig. 3.2) are continuously used in this part. Since only square cell walls are analyzed, $l=h=b$.

4.1.2 In-plane Moduli

For thin walled honeycombs with cell wall angle not close to 0 nor 90°, the bending deflection of the cell walls is the dominant deformation mechanism for the global in-plan compression and shear deformation. Fig. 4.1 (a) depicts the bending mode of the cell walls defined by Gibson and Ashby [1]. A simple investigation reveals that such deformation is equivalent to two jointed cantilever beams with the half-length bended in opposite directions under identical edge forces acting on their free ends, as shown in Fig. 4.1 (b). To start, the deflection of a half perforated cell wall subjected to cantilever-type bending is analyzed, as shown in Fig. 4.2. In order to describe the inner circular boundary, a polar coordinate system is overlapped on the previously defined rectangular coordinate system. The total vertical (the z-direction) force acts at the end of x=0 is F_0, and the corresponding z-direction deflection is δ_0.

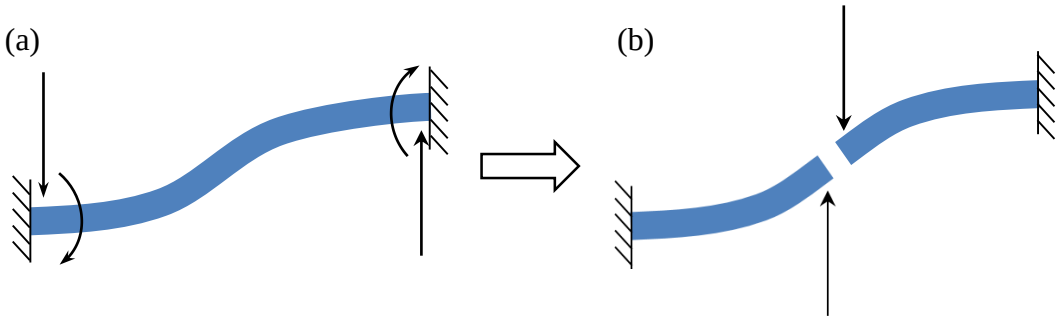

Fig. 4.1. (a) Bending mode of the honeycomb cell walls under uniform external in-plane load and (b) its equivalent form of two cantilever beams.

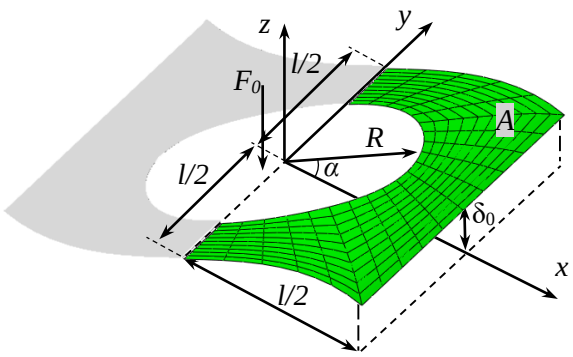

Fig. 4.2. A half perforated cell wall subjected to cantilever-type bending.

Assume that *w(x,y)* is the deflection function of the plate. According to Timoshenko's plate theory [45], the boundary conditions on the outer edges and the inner edge are:

$$w_{x=0} = 0; \quad \left(\frac{\partial^2 w}{\partial x^2}\right)_{x=0} = 0 \tag{4.1a}$$

$$w_{x=\frac{l}{2}} = \delta_0; \quad \left(\frac{\partial w}{\partial x}\right)_{x=\frac{l}{2}} = 0 \tag{4.1b}$$

$$M_{yy} = -D\left(\frac{\partial^2 w}{\partial y^2} + v\frac{\partial^2 w}{\partial x^2}\right)_{y=\pm\frac{l}{2}} = 0 \tag{4.1c}$$

$$V_{\mathrm{yy}} = -D\left(\frac{\partial^3 w}{\partial y^3} + (2-v)\frac{\partial^3 w}{\partial x^2 \partial y}\right)_{y=\pm\frac{l}{2}} = 0 \tag{4.1d}$$

$$M_n = -D\left(\left(\frac{\partial^2 w}{\partial x^2} + v\frac{\partial^2 w}{\partial y^2}\right)cos^2\,\alpha + \left(\frac{\partial^2 w}{\partial y^2} + v\frac{\partial^2 w}{\partial x^2}\right)sin^2\,\alpha\right.$$

$$\left. +2(1-v)\frac{\partial^2 w}{\partial x \partial y}sin\,\alpha\,cos\,\alpha\right)_{\sqrt{x^2+y^2}=R} = 0 \qquad (4.1e)$$

$$V_n = -D\left(\left(\frac{\partial^3 w}{\partial x^3} + (2-v)\frac{\partial^3 w}{\partial y^2 \partial x}\right)\ cos\,\alpha\right.$$

$$\left. +\left(\frac{\partial^3 w}{\partial x^3} + (2-v)\frac{\partial^3 w}{\partial y^2 \partial x}\right)\ cos\,\alpha\right)_{\sqrt{x^2+y^2}=R} = 0 \qquad (4.1f)$$

where M_{yy} and V_{yy} are the moment and shear force in the *y*-direction; M_n and V_n are the moment and shear force in the radial-direction of the polar coordinate system. Continuously using E_s as the elastic modulus of the solid material, t as the plate thickness and v as the solid material's Poisson's ratio, then the bending rigidity of the plate D is given as:

$$D = \frac{E_s t^3}{12(1-v^2)} \qquad (4.2)$$

For small perforations, it can be assumed that the overall deflection is not affected by the perforation. Let $w_s(x,y)$ be the deflection function in this case and assume that the bending curvature is uniform through the *y*-direction, it can be derived from Eq. (4.1a) and (4.1b), by the mechanics of beam deflection that:

$$w_s = \frac{3\,\delta_0}{(l/2)^3}\left(\frac{1}{2}(\frac{l}{2})^2 x - \frac{1}{6}x^3\right) \qquad (4.3)$$

Due to the perforation, the force-deflection relationship is calculated by strain energy method. The total bending energy U_h of the half cell wall is:

$$U_h = \frac{D}{2}\iint_A \left(\left(\frac{\partial^2 w_s}{\partial x^2}+\frac{\partial^2 w_s}{\partial y^2}\right)^2 - 2(1-v)\left(\frac{\partial^2 w_s}{\partial x^2}\cdot\frac{\partial^2 w_s}{\partial y^2}-\left(\frac{\partial^2 w_s}{\partial x \partial y}\right)^2\right)\right) dx\, dy \quad (4.4)$$

where A is the area of the perforated cell wall, i.e. the green area in Fig. 4.2. Let the external work done by the force F_0 be W:

$$W = \frac{1}{2}F_0\delta_0 \quad (4.5)$$

Equating the bending energy and the external work by $U_h=W$, the force-deflection ratio F_0/δ_0 can be obtained, which will be used in the derivation of the effective in-plane moduli later.

For large perforations, the above method is not valid since the perforation greatly changes the stress distribution of the whole cell wall. Therefore, a point-matching method modified from the one proposed in [91] is employed. Let $w_l(x,y)$ be the deflection function in this case. The deflection function in the polar coordinate system that satisfies equilibrium condition is established as:

$$w_l = (A_0 + B_0\, ln(r) + C_0 r^2 + D_0 r^2\, ln(r))\, cos\, \alpha$$

$$+\sum_m^{\infty}(A_m r^m + B_m r^{-m} + C_m r^{m+2} + D_m r^{-m+2})cos(m\,\alpha) \quad (4.6)$$

Applying the inner free edge boundary condition given in Eq. (4.1e) and (4.1f) in the form of the polar coordinates yields the following relationships:

$$B_0 = \frac{R^4\, C_0\, (v+3)}{v-1},$$

$$D_0 = 0,$$

$$A_m = \frac{C_m a_2 b_3 - C_m a_3 b_2 + D_m a_2 b_4 - D_m a_4 b_2}{a_1 b_2 - a_2 b_1},$$

$$B_m = -\frac{C_m a_1 b_3 - C_m a_3 b_1 + D_m a_1 b_4 - D_m a_4 b_1}{a_1 b_2 - a_2 b_1} \tag{4.7}$$

where

$$a_1 = R^{m-2}\, m\, (m-1)\, (1-v),$$

$$a_2 = R^{-m-2} m\, (m+1)(1-v),$$

$$a_3 = R^m\, (m+1)\, \big((m+2) + v\, (2-m)\big),$$

$$a_4 = R^{-m}(m-1)\, \big((m-2) - v\, (m+2)\big),$$

$$b_1 = R^{m-3}\, (m^2 - m^3 + v\, m^3 - v\, m^2),$$

$$b_2 = R^{-m-3}\, (m^2 + m^3 - v\, m^3 - v\, m^2),$$

$$b_3 = R^{m-1}\, (v\, m^3 - m^3 + v\, m^2 + 3m^2 + 4m),$$

$$b_4 = R^{-m-1}\, (-v\, m^3 - m^3 + v\, m^2 + 3m^2 - 4m) \tag{4.8}$$

Observing the bending mode of the cell wall, $w_l(r,\alpha)$ must also satisfiy the following symmetry conditions:

$$w_l(r,\alpha) = -w_l(-r,\alpha),$$

$$w_l(r,\alpha) = w_l(r,-\alpha) \tag{4.9}$$

Hence *m* can only be 3, 5, 7, 9, 11, …. Let the series in Eq. (4.6) be truncated to *K* terms, then there are *(2K+2)* unknowns in Eq. (4.6). To obtain the same number of equations to solve these unknowns, a certain number of points with known boundary conditions are needed. From Eq. (4.1b), each point on the *x=l/2* edge can provide two equations. The points on the *y=1/2* edge satisfies not only Eq. (4.1c) but also the deflection Eq. (4.3), which can also provide two equations. Hence, *(K+1)* points is needed for *(2K+2)* unknowns of *K* terms.

As an example, let *K*=7 (16 unknowns) and select 8 equally space points along the *x=l/2* and *y=l/2* edges as shown in Fig. 4.3, the deflection function can be solved. By the strain energy method given in Eq. (4.4) and (4.5), F_0/δ_0 under large perforations can be obtained. The deflection surface of a full perforated cell wall with *2R/l*=0.75 generated by this point-matching method is plotted in Fig. 4.4, in which singularity is formed in the location of the perforation to match the free boundary condition of the inner edge.

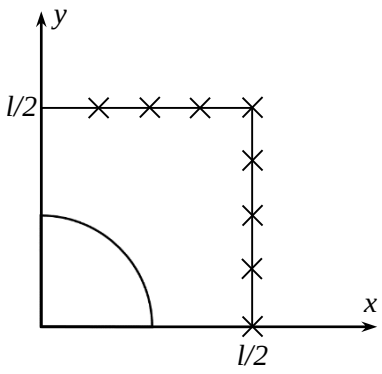

Fig. 4.3. Eight equally spaced points selected on the *x=l/2* and *y=l/2* edges.

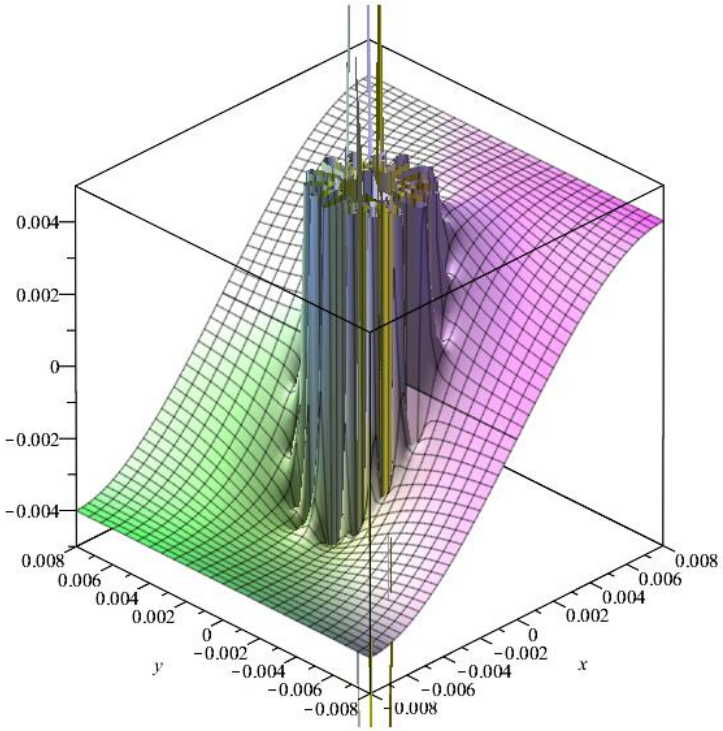

Fig. 4.4. Deflection surface of a perforated cell wall with *2R/l*=0.75.

In addition to the point-matching method, a semi-empirical method that can provide good accuracy is also proposed by this work. It is found that the bending deflection of the perforated cell wall is approximately equivalent to a rectangular plate with the same bending length *l*, total area *A* and a recalculated bending width *l'*, as shown in Fig. 4.5. The bending width *l'* is calculated as:

$$l' = \frac{l^2 - \pi R^2}{l} \tag{4.10}$$

Substituting *l* and *l'* into the solution for cantilever beams or cylindrical bending of wide plates, it can be derived that:

$$\frac{P_0}{\delta_0} = \frac{3Dl'}{(l/2)^3} \tag{4.11}$$

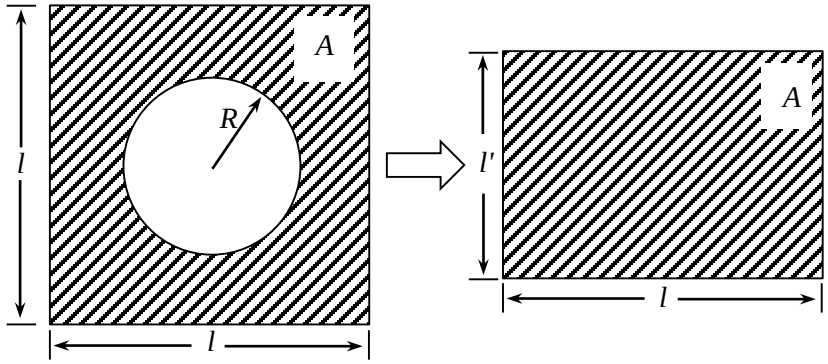

Fig. 4.5. Approximated equivalent shape of a perforated cell wall under bending, the crosshatch regions have the same area.

At last, according to Ashby and Gibson's analytical model [1], the effective in-plane moduli of honeycombs can be expressed by the ratio of the force F_0 to the deflection δ_0 derived above:

$$E_1^* = \frac{cos\theta}{2\,l(1+sin\theta)\;sin^2\,\theta} \cdot \frac{F_0}{\delta_0},$$

$$E_2^* = \frac{(1+sin\,\theta)}{2\,l\,cos^3\,\theta} \cdot \frac{F_0}{\delta_0},$$

$$G_{12}^* = \frac{(1+sin\,\theta)}{3\,l\cos\theta} \cdot \frac{F_0}{\delta_0} \tag{4.12}$$

In as study presented in a later section, it is noticed that the solution of the small perforation derivation is more accurate when $2R/l<0.52$, and the solution of the large perforation derivation is more accurate when $2R/l>0.52$. The in-plane elastic moduli

E_1^* and E_2^* obtained by the above three approaches are compared with the numerical and experimental results in Section 4.4.

4.1.3 Out-of-plane Compressive Critical Buckling Stress

The derivation proposed in [72,74] that use Rayleigh-Ritz method is modified to derive the homogenized buckling stress of perforated honeycombs under constant strain loads. For honeycombs used as sandwich cores, the jointed edges between the cell walls can be approximately seen as simply supported, and the boundary conditions of other two edges that connect with the face sheets are observed as between simply supported and rigidly clamped conditions. Hence, both boundary conditions are modeled in this section to obtain the upper and lower bounds of the buckling stress. Note that in either case, the lateral expansion of the cell walls is restricted, thus the loads on the cell walls are actually biaxial compression.

For the boundary condition that the four edges are simply supported, A.L. Schlack [72,73] suggested the plate deflection function, which is denoted as w_b here, and the in-plane displacement functions u and v in form of the finite polynomial series:

$$w_b = t\,A_{00}\left(1-\frac{4x^2}{l^2}\right)\left(1-\frac{4y^2}{l^2}\right)\left(1+A_{20}\frac{4x^2}{l^2}+A_{02}\frac{4y^2}{l^2}\right),$$

$$u = Bx + t\left(1-\frac{4x^2}{l^2}\right)\frac{2x}{l}\left(B_{00}+B_{20}\frac{4x^2}{l^2}+B_{02}\frac{4y^2}{l^2}\right),$$

$$v = Cy + t\left(1-\frac{4y^2}{l^2}\right)\frac{2y}{l}\left(C_{00}+C_{20}\frac{4x^2}{l^2}+C_{02}\frac{4y^2}{l^2}\right) \tag{4.13}$$

Since the constant strain load is applied in the *y*-direction and there is no lateral expansion in the *x*-direction, it can be derived that B=0. The total energy U of the system consists of the bending energy U_1 and the membrane energy U_2, which are given as:

$$U_1 = D\iint_A \left(\left(\frac{\partial^2 w_b}{\partial x^2}+\frac{\partial^2 w_b}{\partial y^2}\right)^2 - 2(1-v)\left(\frac{\partial^2 w_b}{\partial x^2}\cdot\frac{\partial^2 w_b}{\partial y^2}-\left(\frac{\partial^2 w_b}{\partial x \partial y}\right)^2\right)\right)dx\,dy,$$

$$U_2 = \frac{E_s t}{1-v^2}\iint_A \left(\varepsilon_x^2+\varepsilon_y^2+2v\,\varepsilon_x\varepsilon_y+\frac{1-v}{2}\gamma_{xy}^2\right)dx\,dy \tag{4.14}$$

where A still represents the area of a half of a perforated cell wall, as the green area marked in Fig. 4.2. The membrane strains in the equation are:

$$\varepsilon_x = \frac{\partial u}{\partial x}+\frac{1}{2}\left(\frac{\partial w_b}{\partial x}\right)^2,$$

$$\varepsilon_y = \frac{\partial v}{\partial y}+\frac{1}{2}\left(\frac{\partial w_b}{\partial y}\right)^2,$$

$$\gamma_{xy} = \frac{\partial u}{\partial y}+\frac{\partial v}{\partial x}+\frac{\partial w_b}{\partial x}\cdot\frac{\partial w_b}{\partial y} \tag{4.15}$$

According to Timoshenko [45], for a given constant displacement load C the other constants in Eq. (4.13) should be identified from the conditions of minimum total strain energy, i.e.

$$\frac{\partial U}{\partial X_i} = 0 \tag{4.16}$$

where X_i refers to any of the constants in Eq. (4.13), such as A_{00}, B_{20}, C_{02}, etc. Solving the simultaneous equations derived from Eq. (4.16), the smallest real solution for the edge displacement C can be calculated. Hence, the critical force of a single cell wall is

$$P_{cr} = 2t \cdot \frac{2}{l} \iint_A \sigma_{yy}\, dy\, dx \tag{4.17}$$

where

$$\sigma_{yy} = \frac{E}{1 - v^2}\left(\varepsilon_y + v\varepsilon_y\right) \tag{4.18}$$

Hence the critical stress of a uniformly loaded honeycomb, in its out-of-plane direction, is

$$\sigma^*_{3cr} = \frac{3P_{cr}}{2\cos\theta\,(1 + \sin\theta) l^2} \tag{4.19}$$

For the upper bound boundary condition (two opposite edges clamped and the other two edges simply supported), the deflection and displacement functions in Eq. (4.13) needs to be modified as w_b', u' and v' to fit the zero slope condition at $y=\pm l/2$:

$$w_b' = t\, A_{00}\left(1 - \frac{4x^2}{l^2}\right)\left(1 - \frac{4y^2}{l^2}\right)^2\left(1 + A_{20}\frac{4x^2}{l^2} + A_{02}\frac{4y^2}{l^2}\right),$$

$$u' = Bx + t\left(1 - \frac{4x^2}{l^2}\right)\frac{2x}{l}\left(B_{00} + B_{20}\frac{4x^2}{l^2} + B_{02}\frac{4y^2}{l^2}\right),$$

$$v' = Cy + t\left(1 - \frac{4y^2}{l^2}\right)\frac{2y}{l}\left(C_{00} + C_{20}\frac{4x^2}{l^2} + C_{02}\frac{4y^2}{l^2}\right) \tag{4.20}$$

Substituting the modified deflection and displacement functions into the same process of Eq. (4.14) to (4.19), the upper bound of the buckling stress can be obtained. Due to the fact that the derivations are based on approximate method, the solutions of the bounds are found to have relative large difference compared to the numerical and experimental results at large *2R/l* ratios. Moreover, for large perforations, the instability problem is no longer a plate instability problem, but is similar to the instability problem of two independent

columns with varying cross-sections. The critical stress σ_{3cr}^{*} obtained by the above two methods are compared with the numerical and experimental results in Section 4.4.

4.2 Finite Element Modeling and Empirical Formulas

The homogenization method similar to most of the honeycomb structure studies is used in this part. The effective properties of perforated honeycombs that are numerically investigated and empirically formulated are:

- In-plane elastic moduli E_1^{*} and E_2^{*};
- In-plane shear modulus G_{12}^{*};
- Out-of-plane elastic modulus E_3^{*};
- Out-of-plane shear moduli G_{13}^{*} and G_{23}^{*};
- Out-of-plane bending rigidity D_1^{*}, D_2^{*} and D_{12}^{*};
- Out-of-plane compressive critical buckling stress σ_{3cr}^{*};
- Out-of-plane shear critical buckling stress τ_{13cr}^{*} and τ_{23cr}^{*}.

Note that the effective bending rigidities are not calculated by the classical equation of $D_1=E_1I/(1-\nu_{12}\cdot\nu_{21})$, because Chen, D. H. [33] has demonstrated that the bending rigidities obtained in this way cannot be accurately applied to the honeycomb bending analysis.

4.2.1 Methodologies

The commercial multipurpose finite element software Abaqus (6.12) is used to conduct finite element simulations. As a typical periodic structure, a uniformly loaded infinite honeycomb panel can be accurately represented in FEA by a representative volume element (RVE) with appropriate periodic boundary conditions. The X-shaped RVE suggested by Wilbert, A., et al.'s [48] is used in this work, as shown by the dashed lines drawn in Fig. 4.6 (a), and the meshed model is depicted in Fig. 4.6 (b). The honeycomb cell wall length and height are both l, the thickness is t, and the radius of the circular perforation is R. The RVE built in FEA represents a regular hexagonal honeycomb with the cell wall angle θ=30°, hence it has a nominal transverse cross section area of $\sqrt{3}l \times (3/2)l$. Python script is developed to apply node-by-node periodic boundary conditions on the four truncated edges, i.e. the "a", "b", "c" and "d" edges labeled in Fig. 4.6 (b). To be specific, the degrees of freedom of the node pairs on the "a" and "d" edges are equated to each other, and in the same way on the "b" and "c" edges. The RVE contains a complete cell wall in the middle, which helps verify the boundary conditions by comparing its deformation and stress distribution with those of the four half cell walls. For the in-plane compression and out-of-plane bending tests, however, only a single cell wall is modeled and tested, because the cell wall deformations under these loads are proven to be identical (except cell walls in certain directions) and less dependent to each other.

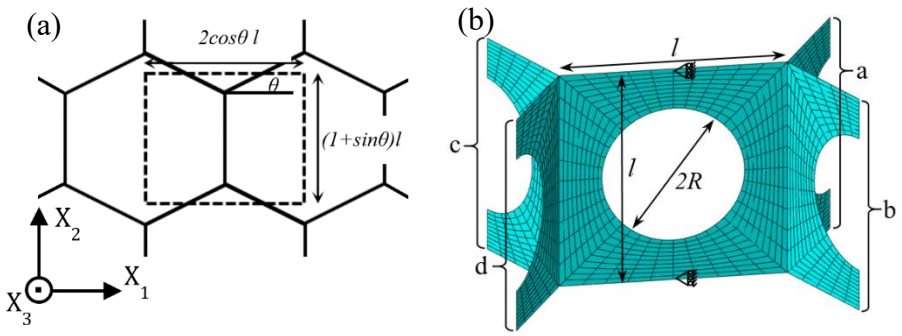

Fig. 4.6. Representative volume element (RVE) model used in finite element testes in (a) 2D view and (b) 3D view.

Nine different finite element tests, as listed in Table 4.1, are carried out with $2R/l$ varying from 0 to 0.875 to obtain the relationships between the perforation size and the effective mechanical properties. The unit cells are discretized by Abaqus's build-in shell elements. The fully integrated four-node element S4 is used for the models subjected to static loadings as it allows for finite membrane strains and can better address the stress concentration around the hole [48]. For buckling problems, the eight-node reduced integration element S8R is used. S8R element considers the transverse shear effect, therefore it provides more accuracy prediction on the elastic instability of thin plates [95]. Mesh sizes for the two element types and three load types—bending, compression and buckling—are determined by three convergence studies shown in Fig. 4.7. The nodes density selected are listed in Table 4.1. Considering the stress concentration near the perforations, a radial gradient mesh topology is adopted, as shown in Fig. 4.6 (b). The critical buckling stresses are solved by the eigen buckling analysis module in Abaqus.

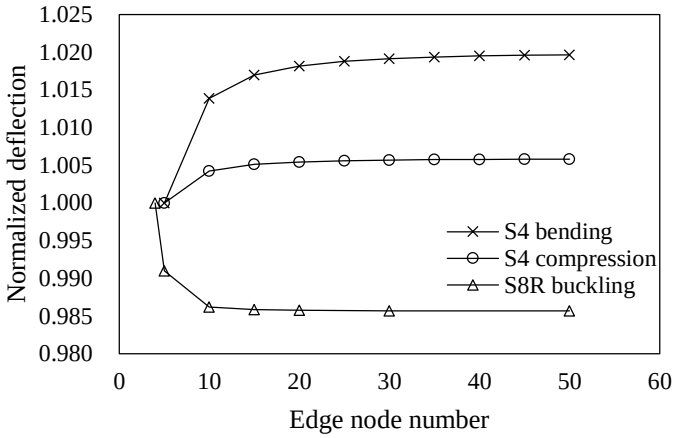

Fig. 4.7. Mesh density convergence of S4 and S8R element under three types of loads

Table 4.1. Modeling details of the finite element honeycomb RVE

Step type	Applied load	Target property	Element type	Side node number	Skin effect
Static, general	Cell wall bending	E_1^*, E_2^*	S4	30	No
Static, general	X_1-X_2 Shear	G_{12}^*	S4	30	No
Static, general	X_3 Compression	E_3^*	S4	30	No
Static, general	X_1-X_3 Shear	G_{13}^*	S4	30	Yes
Static, general	X_2-X_3 Shear	G_{23}^*	S4	30	Yes
Static, general	Cell wall twisting	D_1^*, D_2^*, D_{12}^*	S4	30	No
Buckling	X_3 Compression	${\sigma^3}_{cr}^*$	S8R	10	Yes
Buckling	X_1-X_3 Shear	${\tau^{13}}_{cr}^*$	S8R	10	Yes
Buckling	X_2-X_3 Shear	${\tau^{23}}_{cr}^*$	S8R	10	Yes

Another vital factor in the RVE modeling is its transverse boundary conditions. Since honeycombs are frequently used as sandwich cores, it is necessary to consider the effect of sandwich face sheet, i.e. the skin effect, on the RVE's deformation. Based on previous studies, it is decided that the skin effect is considered in the static shear, out-of-

plane compressive buckling and out-of-plane shear buckling tests. For the buckling problems, responses of the RVE under clamped and simply supported honeycomb-skin connections are investigated as the upper and lower bounds of the actual conditions.

Table 4.2. Geometric parameters and material properties of the finite element RVE

l (mm)	θ (°)	t (mm)	R (mm)	E_s (GPa)	G_s (GPa)	v
20	30	0.4	0~8.75	70	26.92	0.3

To focus on the interested properties and reduce the effect of trivial factors, the material anisotropy and residual stress generated during the manufacturing process are neglected in the finite element model. All cell walls are assumed to be straight without round angles. Table 4.2 lists the material and geometrical parameters of the RVE, in which E_s, G_s and v are the elastic modulus, shear modulus and Poisson's ratio of the cell wall material. These values are chosen based on real Aluminum honeycomb products. When face sheets are not considered, the external loads are applied on the reference points coupled with the nodes of the loading sides of the RVE. For conditions with face sheets, the RVE is bounded onto two rigid plates, and the external loads are applied on the rigid plates.

The FEA results of the effective moduli are normalized by the cell wall material's corresponding moduli E_s and G_s to make the result material-independent. In addition, two comparison curves are provided for every property discussed. Taking Fig. 4.9 as an example, the *Perforated HC* curve represents the normalized FEA results, the *Weight-*

normalized curve represents the values of the *Perforated HC* curve divided by the area ratio of the perforated to unperforated cell wall, which are calculated:

$$E_1^n = \frac{E_1^*/E_s}{(l^2 - \pi R^2)/l^2} \tag{4.21}$$

where E_1^n is the value of the *Weight-normalized* curve.

The values of the *Same weight HC* curve are obtained from the finite element tests conducted on the conventional honeycomb RVE with the identical unit weight and cell wall length but re-calculated cell wall thickness *t'*:

$$t' = t\frac{l^2}{l^2 - \pi R^2} \tag{4.22}$$

By this way the properties of the perforated honeycombs and the conventional honeycomb with the same relative density can be compared.

The empirical formulas are expressed by the corresponding properties of the unperforated honeycombs multiplied by a relation function. For instance:

$$E_1{}^* = E_1{}^u \lambda_1 \tag{4.23}$$

where E_1^u is the corresponding elastic modulus of the unperforated honeycomb with the same cell wall length *l*, thickness *t* and angle θ. λ_1 is a polynomial function that is derived from the FEA results by least square method. The relation functions contain only one variable: the ratio of *2R/l*, and their degree of polynomial is chosen as the smallest number to make the maximum difference between the empirical function and the FEA results less than 1%.

4.2.2 In-plane Elastic Moduli

By the same method used in Eq. (4.12), the effective in-plane elastic moduli of honeycombs can be expressed by the vertical force P_1 and the corresponding deflection δ_1 acting on an inclined cell wall:

$$E_1^* = \frac{cos\theta}{l(1+sin\theta)\ sin^2\theta} \cdot \frac{P_1}{\delta_1},$$

$$E_2^* = \frac{(1+sin\,\theta)}{l\,cos^3\,\theta} \cdot \frac{P_1}{\delta_1} \tag{4.24}$$

P_1 and δ_1 can be obtained from the bending tests of a single cell wall depicted in Fig. 4.8, in which the left end of the cell wall is fully clamped and the right end is constrained from rotation.

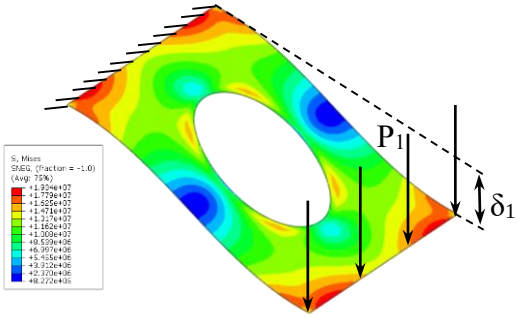

Fig. 4.8. Stress contour of the deformed inclined cell wall of a honeycomb under uniform in-plane compression.

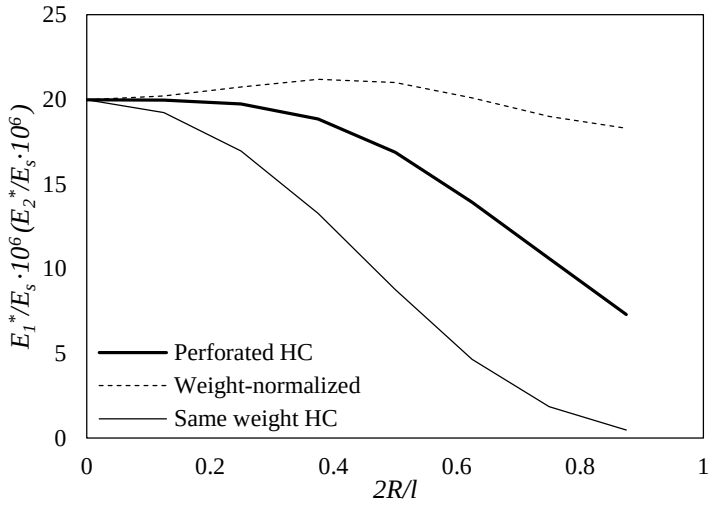

Fig. 4.9. In-plane elastic moduli of perforated honeycombs vs. *2R/l*.

From Eq. (4.24), E_1^* and E_2^* are identical for hexagonal honeycombs with θ=30°, hence the two elastic moduli are shown as one curve (the *Perforated HC* curve) in Fig. 4.9. It shows that small perforations have almost no influence on these two moduli, which dropped by only 1.24% as *2R/l* increases from 0 to 0.25. This can be explained by the classical crack theory that small holes in the middle of a plate have negligible influence on the stress distribution of the far edges. However, such assumption no longer holds when the perforation becomes larger. The *Weight-normalized* curve shows a convex shape with a maximum at *2R/l*=0.397, which is a very useful result for the lightweight designs. The *Perforated HC* curve is higher than the *Same weight HC* curve by 16.23%, 92.66% and 474.91% at *2R/l*=0.25, *2R/l*=0.5 and *2R/l*=0.75 respectively. This significant increase is mainly due to the cubic relationship between the plate's bending rigidity and thickness. Based on the numerical results, the closed-form empirical formulas are given as:

$$E_1^* = E_1^u \lambda_1,$$

$$E_2{}^* = E_2{}^u \lambda_2 \tag{4.25}$$

$$\lambda_1 = \lambda_2 =$$

$$2.7599\left(\frac{2R}{l}\right)^4 - 4.5446\left(\frac{2R}{l}\right)^3 + 1.1337\left(\frac{2R}{l}\right)^2 - 0.0864\left(\frac{2R}{l}\right) + 1 \tag{4.26}$$

Gibson and Ashby's model with small modification is employed to obtain $E_1{}^u$ and $E_2{}^u$:

$$E_1{}^u = \frac{E_s \cos\theta}{(1+\sin\theta)\sin^2\theta\,(1-v^2)}\left(\frac{t}{l}\right)^3,$$

$$E_2{}^u = \frac{E_s(1+\sin\theta)}{\cos^3\theta\,(1-v^2)}\left(\frac{t}{l}\right)^3 \tag{4.27}$$

4.2.3 In-plane Shear Modulus

In this case, the shear loads are applied on the opposite sides of the RVE by the same amount but opposite directions, as shown in Fig. 4.10. The effective in-plane shear modulus $G_{12}{}^*$ is calculated from the edge load P_{12} and the maximum relative displacement δ_{12} by the following equation:

$$G_{12}{}^* = \frac{(1+\sin\theta)}{2l\cos\theta}\frac{P_{12}}{\delta_{12}} \tag{4.28}$$

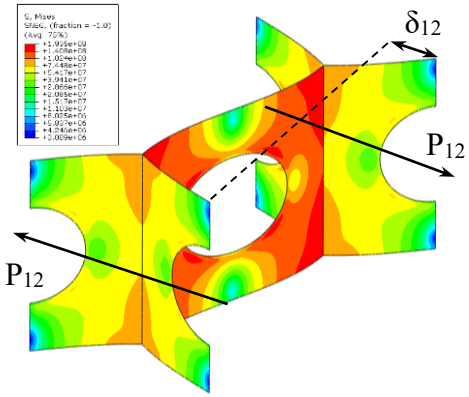

Fig. 4.10. Stress contour of the deformed RVE under in-plane shear

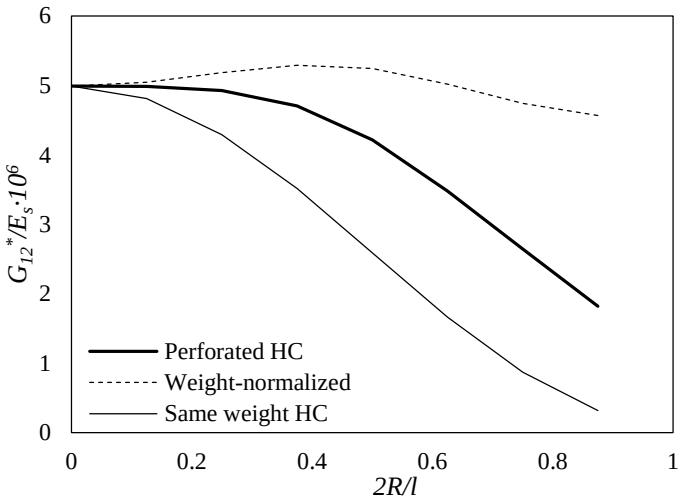

Fig. 4.11. In-plane shear modulus of perforated honeycombs vs. *2R/l*

By the same manner, the G_{12}^*/E_s curve and the two comparison curves are plotted in Fig. 4.11, which shows very similar trends with those in Fig. 4.9. A quantitative comparison shows that the curves of the two figures have almost identical proportions values at various *2R/l*. This is because the cell walls' deflection mode for in-plane compression and shear are the same, even though the cell walls in different directions have

different extents of deflections. Hence, the same polynomial relationship of λ_1 and λ_2 is used in the empirical formula of G_{12}^*:

$$G_{12}{}^{*} = G_{12}{}^{u}\,\lambda_{12}, \tag{4.29}$$

$$\lambda_{12} = \lambda_1 = \lambda_2 =$$

$$2.7599\left(\frac{2R}{l}\right)^4 - 4.5446\left(\frac{2R}{l}\right)^3 + 1.1337\left(\frac{2R}{l}\right)^2 - 0.0864\left(\frac{2R}{l}\right) + 1 \tag{4.30}$$

$G_{12}{}^{u}$ is also calculated by the same method proposed by Gibson and Ashby:

$$G_{12}{}^{u} = \frac{1 + sin\,\theta}{3\,cos\,\theta\,(1 - v^2)}\left(\frac{t}{l}\right)^3 \tag{4.31}$$

4.2.4 Out-of-plane Elastic Modulus

As shown in Fig.4.12, the out-of-plane compression load is applied on the RVE by a uniform displacement δ_3 in the X_3-direction on the transverse edges of the RVE. The RVE is free to have lateral expansion and the total reaction force P_3 is extracted to calculate the effective out-of-plane elastic modulus E_3^*. The lateral expansion of the RVE is free. E_3^* can be calculated using the RVE's section area:

$$E_3^* = \frac{1}{2\,l\,cos\,\theta\,(1 + sin\,\theta)}\frac{P_3}{\delta_3} \tag{4.32}$$

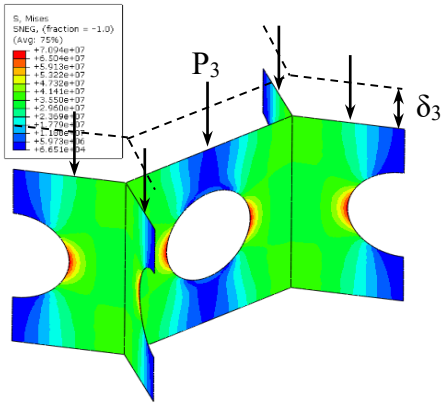

Fig. 4.12. Deformation of the RVE under out-of-plane compression

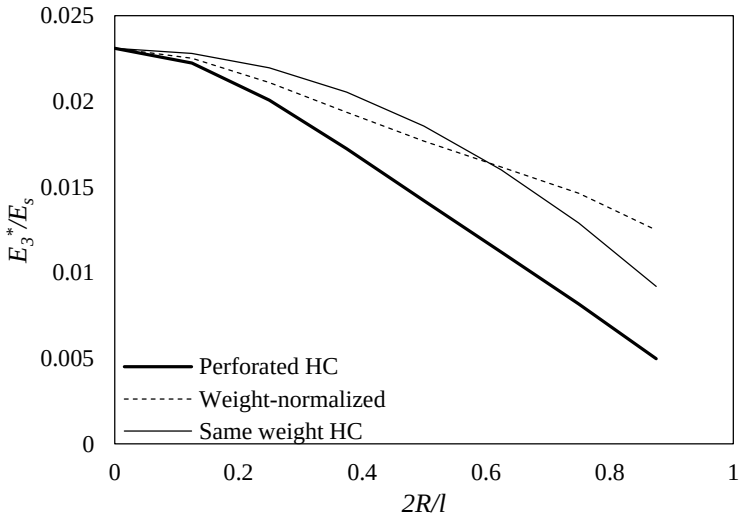

Fig. 4.13. Out-of-plane elastic modulus of perforated honeycombs vs. *2R/l*

It can be noticed from the curves plotted in Fig. 4.13 that the perforations do not bring stiffening effect on the out-of-plane compressive stiffness, even considering the weight saving. This is because the out-of-plane compression response of honeycombs does not have the cubic sensitivity to the cell wall thickness like those of the in-plane moduli, and there is no stress dispersion in the center region. After the initial severe slope change,

the *Perforated HC* curve begin to decrease by a nearly linear manner from *2R/l* =0.2. Different from the in-plane moduli, the *Perforated HC* curve is lower than the *Same weight HC* curve, which further indicates that perforated honeycombs have no advantage over the conventional honeycombs in out-of-plane compression stiffness. However, in comparison with those of Fig. 4.9 and Fig. 4.11, the decrease in stiffness are smaller, which is 9.63%, 30.85% and 57.85% at *2R/l*=0.25, *2R/l*=0.5 and *2R/l*=0.75 respectively, using the lower curve values as the denominator. The empirical formula of E_3^* is derived as follows:

$$E_3^* = E_3^u \lambda_3 \tag{4.33}$$

$$\lambda_3 = 0.821\left(\frac{2R}{l}\right)^3 - 1.475\left(\frac{2R}{l}\right)^2 - 0.2347\left(\frac{2R}{l}\right) + 1 \tag{4.34}$$

E_3^u is obtained by the Voigt and Reuss's upper bound:

$$E_3^u = E_s \frac{3t}{2l\cos\theta\,(1+\sin\theta)} \tag{4.35}$$

4.2.5 Out-of-plane Shear Moduli

In the out-of-plane shear tests, the X-shaped RVE is tied on two rigid plates (not shown in Fig. 4.14). The shear loads are applied on the upper plate while the bottom plate is fully fixed in all degrees of freedom. In other word, lateral expansion is constrained. Due to the similar load type, Eq. (4.32) with minor modification is used here for G_{13}^* and G_{23}^*:

$$G_{13}^* = \frac{1}{2\,l\,cos\,\theta\,(1+sin\,\theta)} \cdot \frac{P_{13}}{\delta_{13}},$$

$$G_{23}^{*} = \frac{1}{2\,l\cos\theta\,(1+\sin\theta)} \cdot \frac{P_{23}}{\delta_{23}} \tag{4.36}$$

where P_{13}, P_{23}, δ_{13} and δ_{23} are the RVE's loads and deflections as marked in Fig. 9 (a) and Fig. 9 (b).

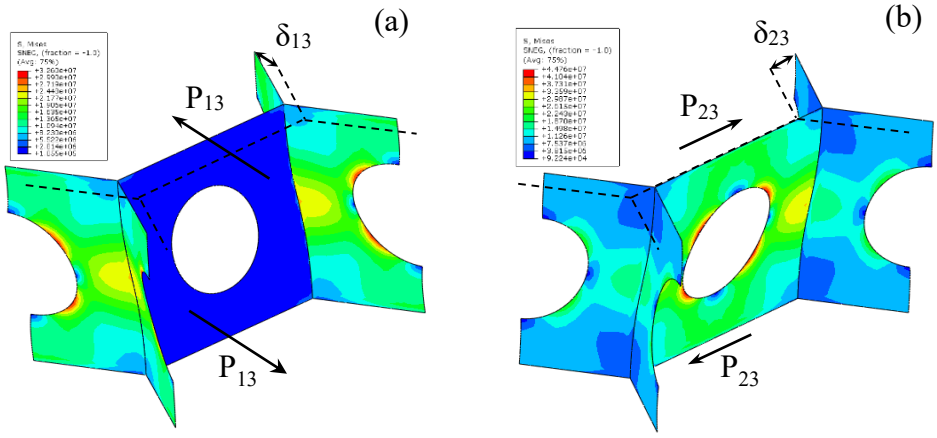

Fig. 4.14. Deformation of the RVE under out-of-plane shear in the (a) X_1-X_3 direction and (b) X_2-X_3 direction

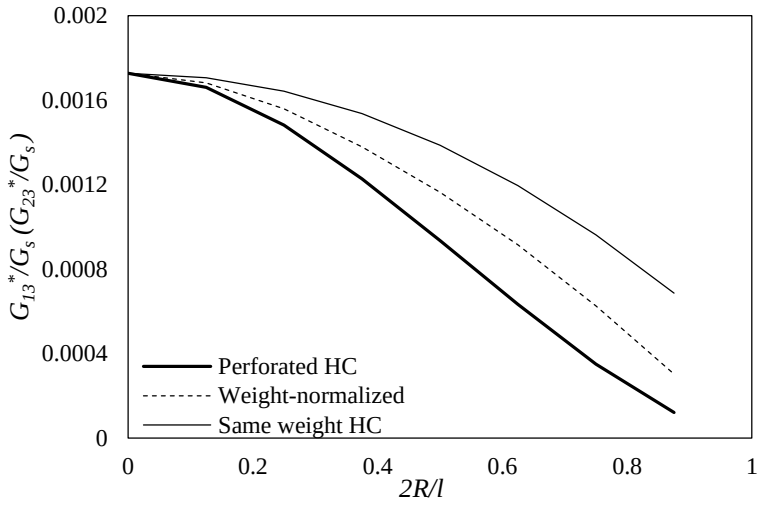

Fig. 4.15. Out-of-plane shear moduli of perforated honeycombs vs. $2R/l$

Similar to E_1^* and E_2^*, the FE simulations produces identical G_{13}^* and G_{23}^* for regular hexagonal honeycombs, as predicted by the existing analytical models [10,28]. Therefore, the two properties are plotted in the same graph as well. The curves in Fig. 4.15 shows that adding perforations on honeycomb cell walls has a negative effect on the specific out-of-plane shear moduli. In this case, the *Same weight HC* curve is higher than the *Perforated HC* curve by 10.83%, 48.37% and 175.34% at $2R/l$=0.25, $2R/l$=0.5 and $2R/l$=0.75 respectively. Analytical calculations show that for honeycombs under out-of-plane shear loads, the single cell walls' planar shear contributes the majority of the strain energy. Under this form of deformation, the stress of a cell wall will concentrate around the two diagonal lines. However, the perforation blocks the stress transfer along the diagonal lines and therefore greatly weakens the shear stiffness.

The empirical formulas for G_{13}^* and G_{23}^* are given as:

$$G_{13}{}^* = G_{13}{}^u \lambda_{13},$$

$$G_{23}{}^* = G_{23}{}^u \lambda_{23} \tag{4.37}$$

$$\lambda_{13} = \lambda_{23} = 1.5876\left(\frac{2R}{l}\right)^3 - 2.5699\left(\frac{2R}{l}\right)^2 - 0.0304\left(\frac{2R}{l}\right) + 1 \tag{4.38}$$

where

$$G_{13}{}^u = \frac{\cos\theta}{(1+\sin\theta)}\left(\frac{t}{l}\right)G_s \tag{4.39}$$

The calculation of G_{23}^u is more complicated compared to G_{13}^u because it is found that G_{23}^u is related to the aspect ratio of the cell wall. Here the empirical solution summarized by Grediac, M. [28] is employed:

$$G_{23}{}^u = 0.213\, G_{23}{}^u_{lower} + 0.787\, G_{23}{}^u_{upper} \tag{4.40}$$

where $G_{23}{}^{u}{}_{lower}$ and $G_{23}{}^{u}{}_{upper}$ are the analytical lower and upper bounds [28]:

$$G_{23}{}^{u}_{lower} = \frac{1 + sin\,\theta}{3\,cos\,\theta}\left(\frac{t}{l}\right)G_s,$$

$$G_{23}{}^{u}_{upper} = \frac{1 + 2\,sin^2\,\theta}{2(1 + sin\,\theta)\,cos\,\theta}\left(\frac{t}{l}\right)G_s \tag{4.41}$$

Numerical method is still suggested by many authors to obtain the accurate solutions of the out-of-plane shear moduli.

4.2.6 Out-of-plane Bending Rigidity

The out-of-plane bending of honeycombs is a collective effect of the twisting and planar bending of the cell walls, and the twisting has been proven to be the dominant mechanism [47]. Hence, a single cell wall instead of the X-shaped RVE is again used in this analysis. From Chen's work [32], the effective bending rigidities can be derived by the cell wall edge twisting moment M_t and the cell wall twisting angle β through the following equations:

$$D_1^* = -\frac{1}{2}\,\frac{cos\,\theta}{(1 + sin\,\theta)\,sin^2\,\theta}\cdot\frac{M_t}{\beta},$$

$$D_2^* = -\frac{1}{2}\,\frac{(1 + sin\,\theta)}{cos^3\,\theta}\cdot\frac{M_t}{\beta},$$

$$D_{12}^* = -\frac{1}{2}\,\frac{1}{sin\,\theta\,cos\,\theta}\cdot\frac{M_t}{\beta} \tag{4.42}$$

And the relationships between the external uniform moment $\bar{M}_1$, $\bar{M}_2$ and the external bending curvature ρ_1, ρ_2 are given by Timoshenko [96]:

$$\bar{M}_1 = D_1^* \frac{1}{\rho_1} + D_{12}^* \frac{1}{\rho_2},$$

$$\bar{M}_2 = D_2^* \frac{1}{\rho_2} + D_{12}^* \frac{1}{\rho_1} \tag{4.43}$$

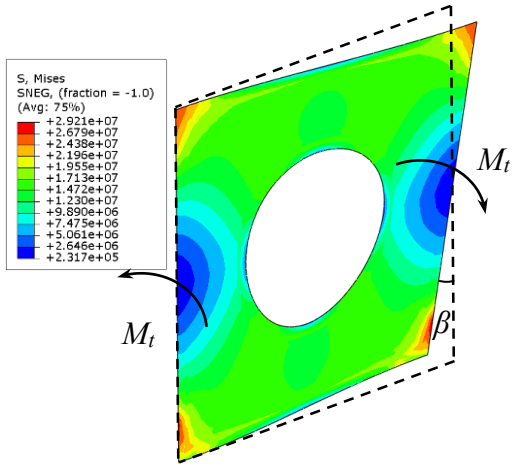

Fig. 4.16. Deflection of an inclined cell wall under overall uniform out-of-plane bending

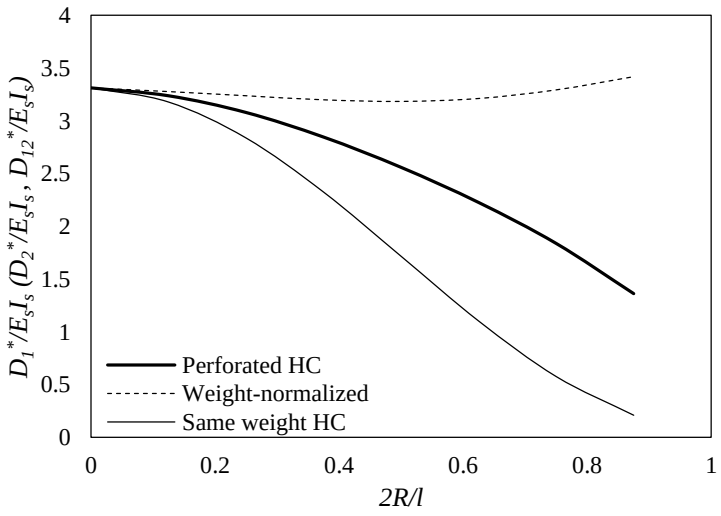

Fig. 4.17. Out-of-plane bending rigidities of perforated honeycombs vs. *2R/l*

Since D_1^*, D_2^* and D_{12}^* are identical for regular hexagonal honeycombs, Fig. 4.17—is used to represent the three bending rigidities. In this figure the curves are normalized by the bending rigidity of the solid cell walls, E_sI_s ($I_s=t^3/12$). Apparently, perforations bring significant increase in the effective bending rigidities compared with these of conventional honeycombs. The *Weight-normalized* curve first decreases slightly as *2R/l* varied from 0 to 0.6 and begin to rise slowly thereafter. The bending rigidity of perforated honeycombs is 8.52%, 49.08% and 218.47% higher than that of the conventional honeycomb counterparts at *2R/l*=0.25, *2R/l*=0.5 and *2R/l*=0.75 respectively. This enhancement is owing to the location of the perforation that is away from the stress concentrated regions, as depicted in Fig. 4.16.

Due to the same twisting mode, the empirical formulas of the three out-of-plane bending rigidities have the same relation function:

$$D_1{}^* = D_1{}^u \lambda_{d1},$$

$$D_2{}^* = D_2{}^u \lambda_{d2},$$

$$D_{12}{}^* = D_{12}{}^u \lambda_{d12} \tag{4.44}$$

$$\lambda_{d12} = \lambda_{d1} = \lambda_{d1} = -0.5912\left(\frac{2R}{l}\right)^2 - 0.1579\left(\frac{2R}{l}\right) + 1 \tag{4.45}$$

The bending rigidities of the regular honeycombs are obtained by the method proposed by Chen [32]:

$$D_1{}^u \approx -\frac{0.121\cos\theta\, E_s t^3}{(1+\sin\theta)\sin^2\theta},$$

$$D_2{}^u \approx -\frac{0.121(1+\sin\theta)E_s t^3}{\cos^3\theta},$$

$$D_{12}{}^{u} \approx -\frac{0.121 E_s t^3}{cos\,\theta \sin\theta} \tag{4.46}$$

4.2.7 Out-of-plane Critical Compressive Stress

In this and the next subsections, constant displacement are applied on the rigid plates bounded to the RVE, and the reaction force on the rigid plates at the critical displacement is extracted to calculate the effective critical stress. Two types of honeycomb-skin connections—simply supported and clamped—are modeled to obtain the lower and upper bounds of the critical stress. The first eigen buckling mode under these two boundary conditions are shown in Fig. 4.18. From the curves plotted in Fig. 4.19, it is observed that even without considering the weight, perforated honeycomb still demonstrates enhanced critical stress compared to the conventional honeycombs. If the weight is taken into consideration, such effect becomes even more significant. Taking *Perforated HC, clamped* curve as an example, the perforated honeycomb has the critical stress 16.30%, 92.66% and 474.91% higher than the *Same weight HC, clamped* curve at *2R/l*=0.25, *2R/l*=0.5 and *2R/l*=0.75 respectively.

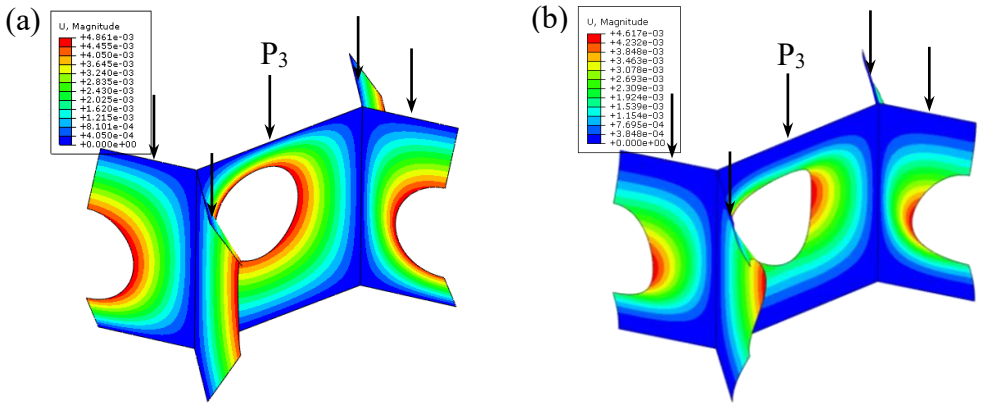

Fig. 4.18. First buckling mode of the RVE under out-of-plane compression with (a) simply supported connection and (b) clamped connection.

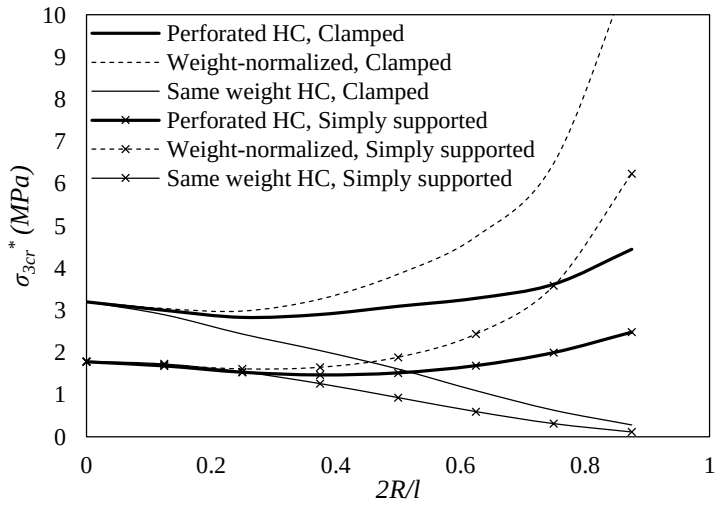

Fig. 4.19. Out-of-plane compressive buckling stress of perforated honeycombs vs. *2R/l*.

The critical buckling shape is the major cause for this drastic increase in buckling resistance. The bending deformation of the first buckling mode shown in Fig. 4.18 accumulates quickly around the center of the plate to satisfy the smallest half wave number. Since strain energy method indicates that bifurcation occurs when the work done by the external force on the plate membrane becomes larger than the bending strain energy

of any possible shape [85], punching a hole in the center of the plate will redistribute the membrane stress to the constrained boundaries and thereby increase the force needed to reach the smallest buckling mode. Although plate buckling will not cause a drastic decrease of the in-plane stress, it will lead to many other types of failures and fractures such as local yielding, delaminating and debonding between the honeycomb core and skin [86–88]. Therefore, this result shows a great potential for the future application of perforated honeycombs.

For the simply supported connection, i.e. the lower bound, the empirical formula is:

$$\sigma_{3cr,s}^{*} = \lambda_{3cr,s} \cdot \sigma_{3cr,s}^{u} \tag{4.47}$$

$$\lambda_{3cr,s} = -1.8021\left(\frac{2R}{l}\right)^{4} + 4.6733\left(\frac{2R}{l}\right)^{3} - 1.7853\left(\frac{2R}{l}\right)^{2} - 0.359\left(\frac{2R}{l}\right) + 1 \tag{4.48}$$

For the clamped connection, i.e. the upper bound, the empirical formula is:

$$\sigma_{3cr,c}^{*} = \lambda_{3cr,c} \cdot \sigma_{3cr,c}^{u} \tag{4.49}$$

$$\lambda_{3cr,c} = 15.384\left(\frac{2R}{l}\right)^{5} - 30.147\left(\frac{2R}{l}\right)^{4} + 20.243\left(\frac{2R}{l}\right)^{3} - 4.116\left(\frac{2R}{l}\right)^{2} - 0.2723\left(\frac{2R}{l}\right) + 1 \tag{4.50}$$

in which $\sigma_{3cr,s}{}^{u}$ and $\sigma_{3cr,c}{}^{u}$ are approximately calculated by the critical buckling force of a square plate. Because no lateral expansion is allowed, the load on the plate is actually biaxial compression. The solution for these buckling problems can be found in [96]. Combined with the RVE geometry, the expression for $\sigma_{3cr,s}{}^{u}$ and $\sigma_{3cr,c}{}^{u}$ are given as:

$$\sigma_{3cr,s}^{u} = \frac{E_s t^3 \pi^2}{2(1-v^2)(v+1)l^3 \cos\theta\,(1+\sin\theta)} \tag{4.51}$$

$$\sigma_{3cr,c}^{u} = \frac{81E_s t^3 \pi^2}{24(1-v^2)(3l^2 v + 4l^2) l \cos\theta\,(1+\sin\theta)} \tag{4.52}$$

4.2.8 Out-of-plane Critical Shear Stress

The in-plane moduli E_1^* and E_2^* are identical due to the planar isotropy of regular hexagonal honeycombs, but the out-of-plane critical shear buckling stresses in the X_1 and X_2 directions are different as a result of the different amounts of shear loads in cell walls along different directions. In Fig. 4.20, when P_{13} is applied on the RVE, the cell wall along the *y*-direction bears no in-plane shear load, hence the buckling initiates on the inclined cell walls first. But when P_{23} is applied, the same cell wall bears half of the total shear load, hence it will buckle before the inclined cell walls. However, since the buckling mode of the different cell walls are identical, the shape of the τ_{13cr}^* and τ_{23cr}^* curves are very similar, as shown in Fig. 4.21 (a) and Fig. 4.21 (b). It is obvious that both the perforated and unperforated honeycomb curves have decreased shear buckling stress as the perforation radius increases, but the trend is slightly different. For all of the four loading conditions (P_{13}, P_{23}; simply supported, clamped), the critical stresses of the conventional honeycomb are initially larger than that of the perforated honeycomb, then the *Same weight HC* curves fall below the *Perforated HC* curves when *2R/l* exceeds some certain values. However, from Fig. 4.21 it can be observed that the differences between these two curves are not significant, so in general the perforation can be seen as having neutral effect on the out-of-plane shear buckling resistance.

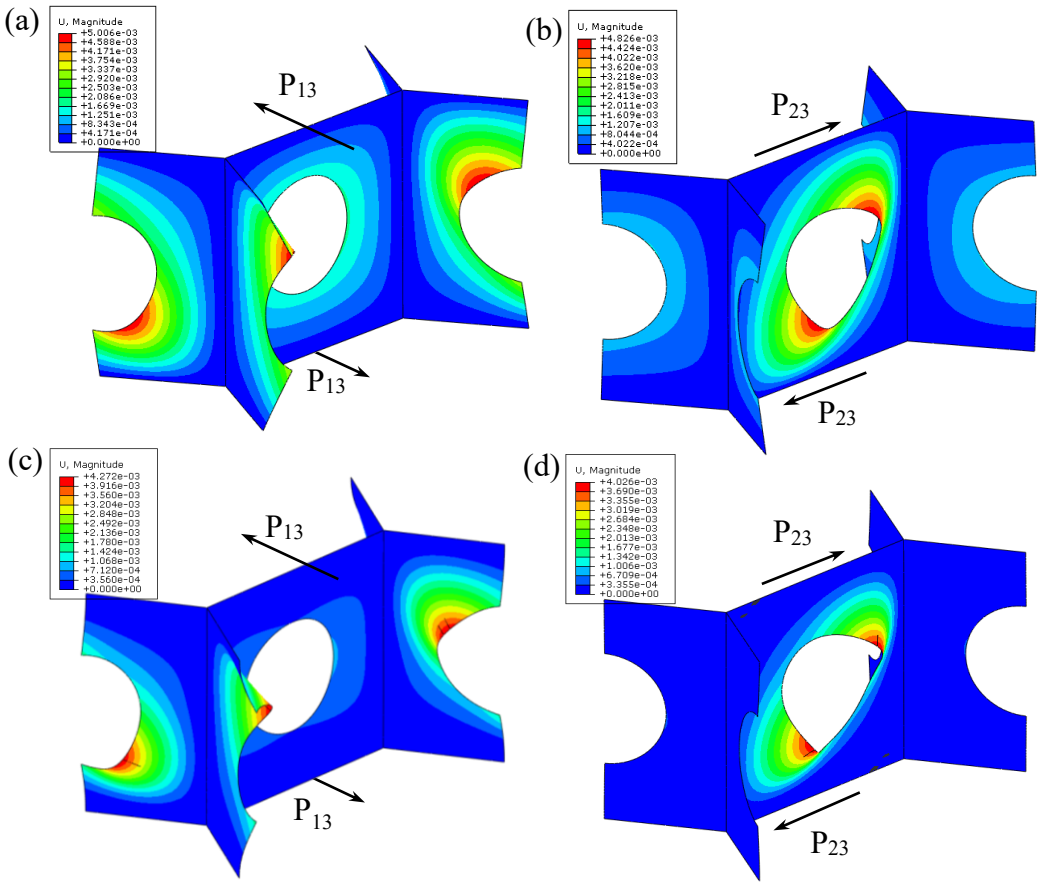

Fig. 4.20. First buckling mode of the RVE under out-of-plane shear loads. (a) X_1-X_3 shear with simply supported connection; (b) X_2-X_3 shear with simply supported connection; (c) X_1-X_3 shear with clamped connection; (d) X_2-X_3 shear with clamped connection.

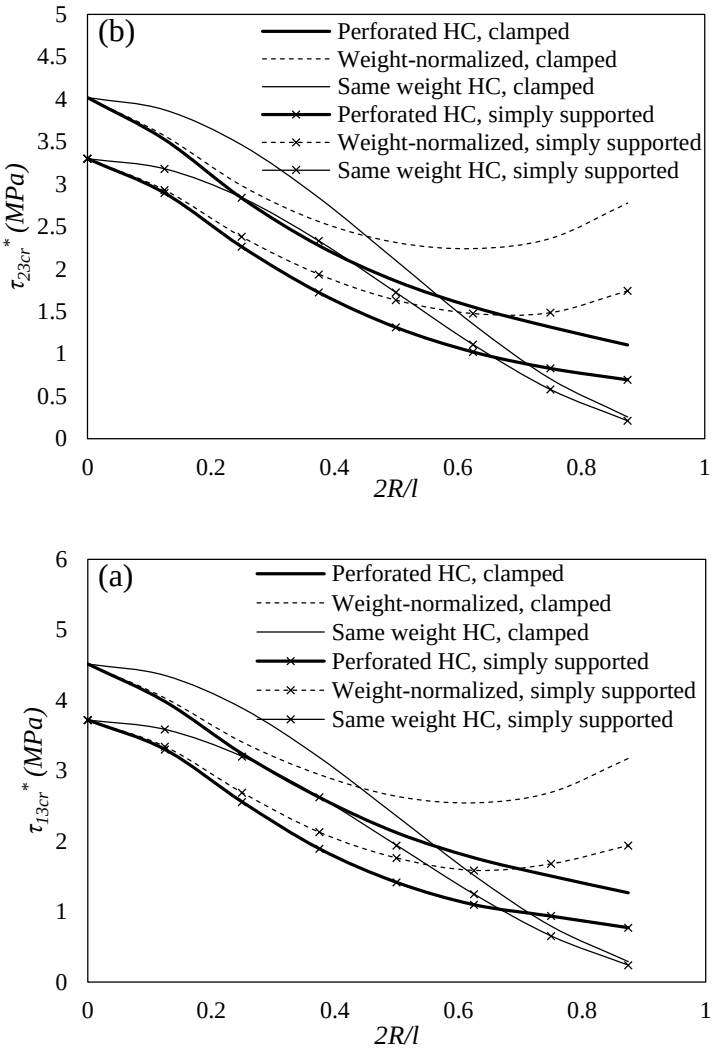

Fig. 4.21. Out-of-plane critical shear stress of perforated honeycombs vs. *2R/l* in the (a) X_1-X_3 and (b)X_2-X_3 directions

From the buckling shapes illustrated in Fig. 4.20, it is found that the bulging deformation formed an ellipse with its major axis coincides with one of the cell walls' diagonal lines. In this case, the tensile stress along that diagonal line tends to obstruct the out-of-the-plane deflection of the plate, but the perforation blocks the transfer of that tensile stress and hence make the plate more prone to buckling. On the other hand, since

the compression stress along the other diagonal line facilitates the plate's buckling, the overall effect of the perforations on the shear buckling tends to be neutralized. Due to the similar curve shape and identical buckling mode of the cell wall, is it found that the shear buckling stresses in the two directions under the same edge connection (simply supported or clamped) can be accurately expressed by one relation function, which means two relation functions are needed in the four empirical formulas:

$$\tau^*_{13cr,s} = \lambda_{13cr,s}\tau^u_{13cr,s},$$

$$\tau^*_{13cr,c} = \lambda_{13cr,c}\tau^u_{13cr,c},$$

$$\tau^*_{23cr,s} = \lambda_{23cr,s}\tau^u_{23cr,s},$$

$$\tau^*_{23cr,c} = \lambda_{23cr,c}\tau^u_{23cr,c} \tag{4.53}$$

$$\lambda_{13cr,s} = \lambda_{23cr,s} = 0.9843\left(\frac{2R}{l}\right)^3 - 0.4548\left(\frac{2R}{l}\right)^2 - 1.2644\left(\frac{2R}{l}\right) + 1 \tag{4.54}$$

$$\lambda_{13cr,c} = \lambda_{23cr,c} = 0.4234\left(\frac{2R}{l}\right)^3 + 0.0556\left(\frac{2R}{l}\right)^2 - 1.1981\left(\frac{2R}{l}\right) + 1 \tag{4.55}$$

where $\tau_{13cr,s}^*$ and $\tau_{23cr,s}^*$ are the lower bounds (simply supported) of critical shear buckling stress in the X_1-X_3 and X_2-X_3 directions respectively, and $\tau_{13cr,c}^*$ and $\tau_{23cr,c}^*$ are the upper bounds (clamped) of critical shear buckling stress in the X_1-X_3 and X_2-X_3 directions respectively. The critical shear stresses of the regular honeycombs are calculated from the shear buckling coefficient of a square plate:

$$\begin{Bmatrix}\tau^u_{13cr,c}\\ \tau^u_{13cr,s}\end{Bmatrix} = k_s \frac{E_s t^2 \pi^2}{12(1-v^2)l^2} \cdot \frac{t}{l(1+\sin\theta)} \tag{4.56}$$

$$\begin{Bmatrix}\tau^u_{23cr,c}\\ \tau^u_{23cr,s}\end{Bmatrix} = k_s \frac{E_s t^2 \pi^2}{12(1-v^2)l^2} \cdot \frac{t(1+2\sin^2\theta)}{2l\cos\theta\,(1+\sin\theta)} \tag{4.57}$$

where k_s is the shear buckling coefficient of a square plate. FE studies show that k_s=11.15 and k_s=13.52 for the lower bound and upper bound respectively.

It is noteworthy that although all of the empirical formulas derived in this section are based on regular hexagonal honeycombs, they can also describe irregular hexagonal honeycombs ($\theta \neq 30°$) since the cell wall angle factor is included in the conventional honeycomb properties like E_1^u.

4.3 Experimental Verification

To verify the derived empirical formulas, a series of perforated honeycomb specimens were fabricated through 3D printing (EOS P 396 selective laser sintering printer, EOS of North America Inc, Novi, MI) from nylon powders. The designed size parameters of these specimens are: l=16mm, t=0.7mm, θ=30°. Specimens of three perforation sizes—$2R/l$=0.25, $2R/l$=0.5 and $2R/l$=0.75— are printed, as shown in Fig. 4.22 from left to right. Each design has two replicates, which are labeled as A and B in the following graphs. Pre-tests were carried out on three solid cubic parts printed in the same batch to measure the modulus of the printed bulk. The results showed that the printed material has almost isotropic elastic modulus of 943 MPa. Due to the coarse surface generated from during sintering, the actual working thickness is less than the designed thickness. Thus, another two tests were conducted on two conventional honeycomb specimens, and the actual working thickness is calculated by substituting the measured stress-strain slope into Gibson and Ashby's analytical honeycomb model. It was found

that for the designed thickness of 0.7mm, the actual working thickness is 0.62mm. The real modulus and thickness obtained above are used in the calculation of the empirical solutions that are compared to the test results.

Compression tests in the X_1, X_2 and X_3 directions were conducted on the perforated honeycomb specimens. The tests were operated according to ASTM C364/C364M test standard for sandwich core edgewise compressive properties and C365/C365M test standard for sandwich core flatwise compressive properties. For the in-plane (edgewise) tests, a special fixture was made according to the ASTM standard to prevent the specimen's flatwise deflection, as shown in Fig. 4.23 (a). The fixture has a loose fit with the specimens, and the contacting surfaces were polished to reduce the friction that hampers the specimens' lateral expansion. For the out-of-plane (edgewise) tests, the specimens were not bonded onto the platens because any adhesive that is strong enough to form clamped boundary condition (constrain the edge rotations) will generate non-negligible property change on the adjacent material. Instead, two 1000 grit sandpapers were adhered on the upper and lower platens to approximate the simply supported non-expansion boundary condition, as shown in Fig. 4.23 (b). The tests were performed on a MTS insight screw driven mechanical test machine. The head displacement rates were 1mm/min and 0.5mm/min for the in-plane and out-of-plane compression tests respectively. For the out-of-plane compression test, the process was video recorded to capture the moment of onset of buckling onset, so that the corresponding load force can be obtained from the exported test data. The reason for using this method is because

usually there is no significant slope change on the stress-strain curve that can be identified as buckling [97].

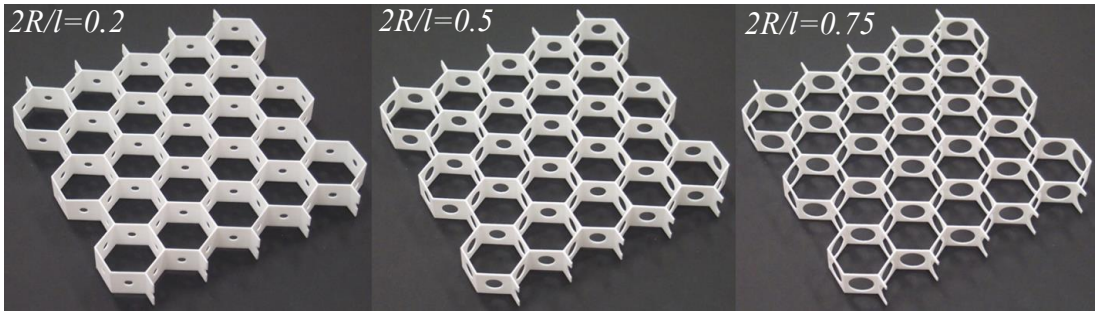

Fig. 4.22. 3D Printed perforated honeycomb specimens with *2R/l*=0.25, *2R/l*=0.5 and *2R/l*=0.75, from left to right.

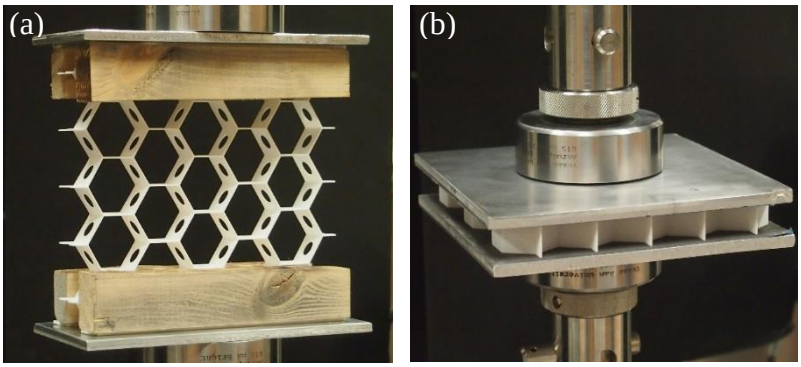

Fig. 4.23. Experiment setups for (a) in-plane (edgewise) compression tests and (b) out-of-plane compression tests.

4.4 Results and Discussion

In this part, the in-plane elastic moduli and out-of-plane compressive buckling stress obtained from the analytical model, empirical formulas and experimental tests are compared and discussed. Since the empirical formulas provide almost identical results

with those of the finite element simulations (recall that the maximum difference is less than 1%), numerical studies that repeats the experimental tests are not conducted.

In Fig. 4.24, the experimental results of the in-plane effective moduli E_1^* and E_2^* are compared with the analytical solutions calculated from Eq. (4.1) to (4.12) and the empirical formulas in Eq. (4.25) to (4.27). As mentioned in Section 4.1, two different methods are used to derive the analytical in-plane elastic moduli for honeycombs with small perforation and large perforation respectively, and $2R/l$=0.52 is the dividing point of using the two solutions. It is obvious that the two analytical solutions are very accurate when $2R/l$ is close 0 or 1, but they show a relative large deviation around the dividing point, at which the analytical result is 16.72% higher than the empirical result. The solutions obtained by the effective width method is also plotted in Fig. 4.24 as the dot-dashed line. It can be seen that through the whole domain, the empirical results agree better with the experimental data than the analytical results. The effective width method also shows a good prediction, but the curve trend at $2R/l > 0.5$ doesn't match the experimental data very well. Besides, all of the empirical and analytical solutions tend to overestimate the effective in-plane modulus at large $2R/l$ values. The major reasons for this difference is the size of the specimen. The RVE used in the finite element simulations aims to model an infinite honeycomb panel, but the outer cell walls of the specimens are less constrained than the inner cell walls, which makes the specimens less stiff under compression.

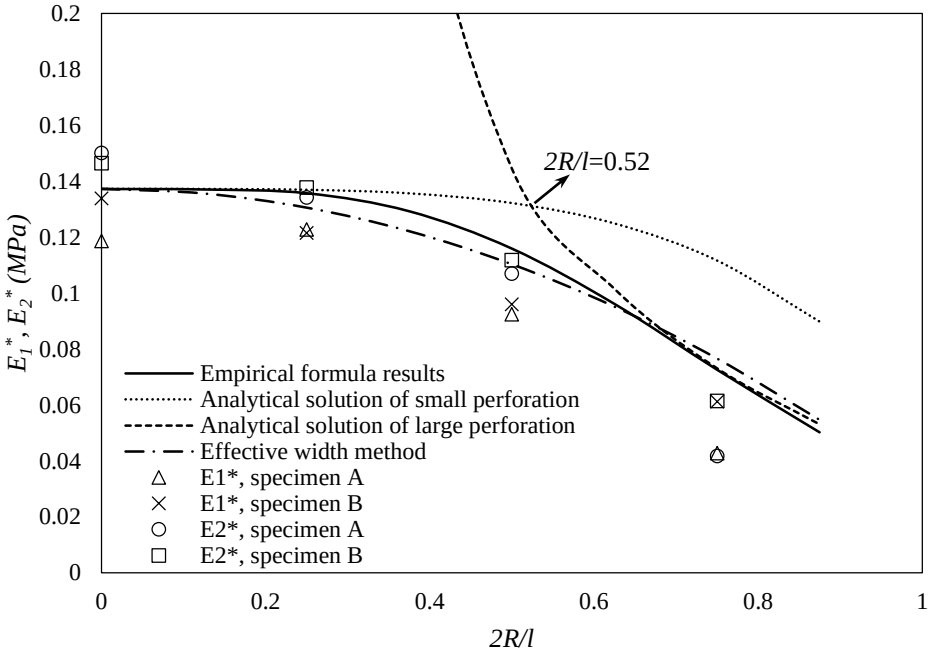

Fig. 4.24. Graphical comparison of analytical, empirical and experimental results of in-plane elastic moduli.

In Fig. 4.25, the buckling stresses of the specimens under the X_3-direction load are plotted and compared with the upper and lower bounds calculated from the analytical model stated in Eq. (4.13) to (4.20) and the empirical formulas stated in Eq. (4.47) to (4.52). Although there is no bonding between the honeycombs and the compression platens, the cell walls' free rotation at their contacting edges is still hindered due to the non-negligible cell wall thickness, which leads to an anti-rotation moment about the middle plane. Hence, the real cell walls' constraint is between simply supported and clamped condition, and this condition agrees with the data distribution of the first three points shown in Fig. 4.25. Form this figure it can be seen that the analytical upper and lower bounds buckling stress have a good agreement with the experimental and empirical

results in most of the domain. At large *2R/l* ratio, the approximate Rayleigh-Ritz method leads to a sharply increased buckling stress, which is due to the different eigen buckling mode, as discussed in the end of Section 4.1.3. For the first three *2R/l* values, the experimental results do not strictly follow the decrease-increase trend of the analytical and empirical curves, but remained broadly unchanged. In the aspect of unit weight buckling resistance, this result confirmed that honeycombs with perforated cell walls have improved specific buckling stress compared with the conventional honeycombs with the same relative density. At $2R/l=0.75$, in contrast to the increased analytical and empirical curves, the experimental results decreased steeply and fell below the two lower bounds. Observing the shape of the deformed specimens, two causes are found for this significant difference. The first cause is the finite specimen size. For large *2R/l* ratios, the cell wall behaves more like two independent columns with varying cross-sections. The inner columns with three jointed cell walls can maintain a straight center line at a very high compression load, but the outer columns (around the perimeter of the specimen) with only two jointed cell walls tend to bend outward at a relatively small load. The second cause is the buckling mode change. It is observed that, when the compression load exceeded a certain value, the $2R/l=0.75$ specimens generated a slight horizontal relative displacement between its upper and lower surfaces, which made the buckling mode shifted from axial buckling (Fig. 4.18) to shear buckling (Fig. 4.20), which has a much lower buckling coefficient at a large perforation size. For this reason, perforations with $2R/l>0.5$ are not recommended for the purpose of improving buckling resistance. However, this criterion is less critical for large honeycomb panels.

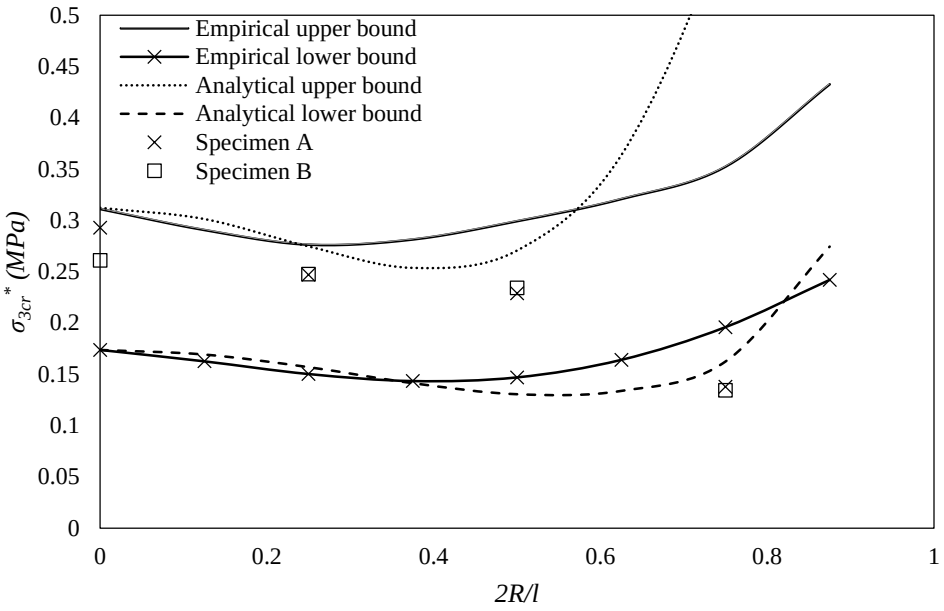

Fig. 4.25. Graphical comparison of analytical, empirical and experimental results of the homogenized out-of-plane critical stress.

In spite of the difference between the empirical and experimental buckling stresses, it is important that the finite element simulations conducted on the RVE can predict the buckling modes of the cell walls, as shown in Fig. 4.26. In both approaches, there is one half-wave buckling on each cell wall and the bulging out directions of the cell walls are barreling about the center axes of the cell wall joints.

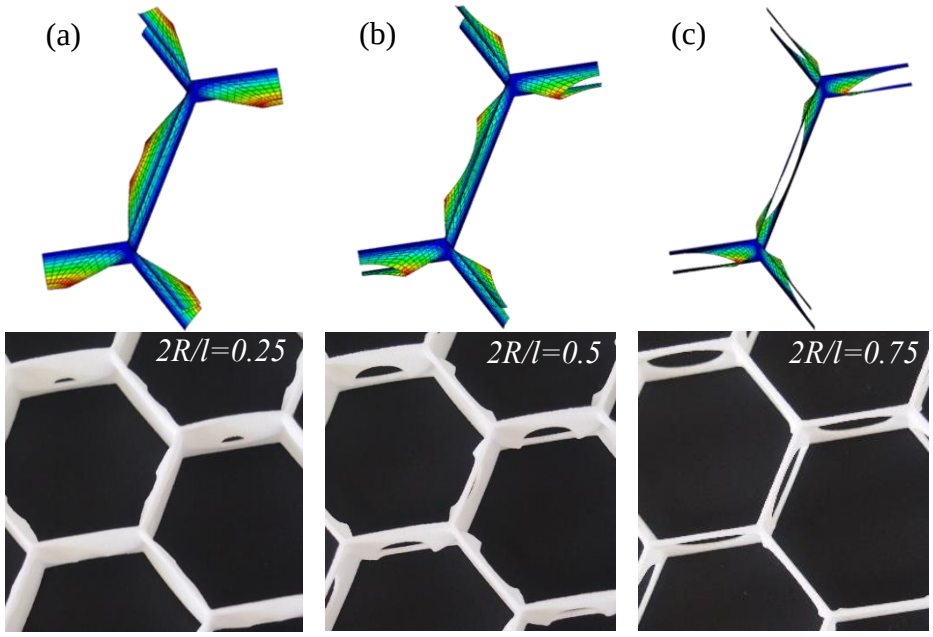

Fig. 4.26. The buckling modes of the deformed specimens and the RVE with (a) $2R/l$=0.25, (b) $2R/l$=0.5, (c) $2R/l$=0.75

4.5 Conclusions

A numerical and experimental study is carried out to investigate and summarize the mechanical behaviors of a new type of honeycombs with perforated cell walls. FE simulations are conducted on a RVE with periodic boundary conditions, and the empirical formulas for the homogenized moduli, bending rigidities and critical buckling stresses are derived based on the FEA results. A series of specimens were fabricated by 3D printing, and their compressive responses were tested and compared with those obtained from the empirical formulas.

To summarized the influence of the perforations, the percentage change of the properties of the perforated honeycombs with respect to the conventional honeycombs of

the same relative density at three *2R/l* ratios are listed in Table 4.3. A positive percentage indicates an improved property by the perforations and vice versa. The results show that adding perforations on the cell walls increases the in-plane moduli, bending rigidities, and out-of-plane compressive buckling resistance; but it decreases the out-of-plane moduli. For the out-of-plane shear buckling resistance, perforations have in general a nearly neutral effect. The in-plane and out-of-plane compression tests conducted on the 3D printed specimens verified the empirical in-plane moduli, but revealed that the buckling mode of the honeycombs with large perforation sizes is likely to shift from compressive buckling to shear buckling, which leads to a much lower buckling stress than the numerical results. Based on this fact, a *2R/l* ratio smaller than 0.6 is suggested to obtain the maximized buckling resistance per unit weight for small honeycomb panels. These property enhancements show potentials for the perforated honeycombs to be utilized in real products based on the requirements of the specific applications.

Table 4.3. Properties change brought by the perforations at three *2R/l* ratios

2R/l	**0.25**	**0.5**	**0.75**
E_1^*, E_2^*, G_{12}^*	16.2%	92.7%	474.9%
E_3^*	-8.8%	-23.6%	-36.7%
G_{13}^*, G_{23}^*	-9.8%	-32.6%	-63.7%
D_1^*, D_2^*, D_{12}^*	8.5%	49.1%	218.5%
$\sigma_{3cr,s}{}^*$	-1.0%	62.6%	540.0%
$\sigma_{3cr,c}{}^*$	16.3%	92.7%	474.9%
$\tau_{13cr,s}{}^*$	-20.1%	-27.0%	-43.4%
$\tau_{13cr,c}{}^*$	-16.7%	-10.0%	86.4%

Stress concentration around the perforations is not investigated in this part of work, but it can be an important factor to determine the real failure mode—for large holes the cell walls may yield first instead of buckle. The issue is material and thickness related and should be studied case by case.

5. SUMMARY AND FUTURE WORK

In this work, three novel honeycombs with modified cell walls are proposed and investigated in three corresponding parts.

The first part provides the analytically homogenized stiffness matrix of honeycombs with spline-shaped cell walls. This new model is proven to be accurate in describing a wide range of 2-D periodic structures with non-linear cell walls. Based on the parametric study results, cell wall design strategies are suggested for maximizing the in-plane moduli and out-of-plane buckling resistance of this honeycomb. For future work, further research is suggested to model the out-of-plane buckling stress by examining into the range of the spline function's curvature that allows low eigenvalue buckling modes to occur. The spline cell walls with more control points can also be studied to obtain higher specific stiffness and specific strength.

The second part proposes a novel honeycomb with laminated composite cell walls. The analytically homogenized stiffness matrix for this new honeycomb is derived and verified numerically. Parametric study shows that the homogenized in-plane moduli change non-linearly with the ply thickness ratio—a small thickness of the stiffer ply can bring a large increase in the effective moduli. To further explore the potential of this type of honeycombs, their collapse process can be investigated in the future. In addition to the plastic failure as that of the conventional honeycombs, the composite cell walls can also delaminate. Such failure can greatly change the stress-strain response during the collapsing process.

The third part proposes a novel honeycomb with centric circular perforations on its square cell walls. An X-shaped representative volume element with periodic boundary conditions is built for finite element analysis to investigate the influence of the perforation size on the homogenized stiffness and buckling stress. It is observed that these perforations can greatly improve some of the properties at a unit weight. Empirical formulas are derived from the numerical results to predict the behavior of this honeycomb. Future work can include the investigation of the stress concentration around the perforations under different loads, and how the perforation changes the failure mode of honeycombs. Mechanical behaviors of honeycombs with rectangular cell walls and multiple perforations on one cell wall can also be considered in the next stage of this research.

REFERENCES

[1] Gibson LJ, Ashby MF. Cellular solids: Structure and properties. Cambridge: Canbridge University Press, 1999

[2] Sarikaya M, Gunnison KE, Yasrebi M, Aksay IA. Mechanical Property-microstructural relationships in abalone shell. Mater Reseaerch Soc Symp 1990;174:109–116.

[3] Jain S, Kumar R, Jindal UC. Mechanical behaviour of bamboo and bamboo composite. J Mater Sci 1992;27:4598–4604.

[4] Wang A-J, McDowell DL. In-plane stiffness and yield strength of periodic metal honeycombs. J Eng Mater Technol 2004;126:137–156.

[5] Kintscher M, Karger L, Wetzel A, Hartung D. Stiffness and failure behaviour of folded sandwich cores under combined transverse shear and compression. Compos Part A Appl Sci Manuf 2007;38:1288–1295.

[6] Nilsson E, Nilsson Ac. Prediction and measurement of some dynamic properties of sandwich structures with honeycomb and foam cores. J Sound Vib 2002;251:409–430.

[7] Petras a., Sutcliffe MPF. Failure mode maps for honeycomb sandwich panels. Compos Struct 1999;44:237–252.

[8] Xu XF, Qiao P, Davalos JF. Transverse shear stiffness of composite honeycomb core with general configuration. J Eng Mech 2001;127:1144 –1156.

[9] Frank Xu X, Qiao P. Homogenized elastic properties of honeycomb sandwich with skin effect. Int J Solids Struct 2002;39:2153–2188.

[10] Wadley HNG. Multifunctional periodic cellular metals. Philos Trans R Soc A Math Phys Eng Sci 2006;364:31–68.

[11] Hohe J, Becker W. Effective stress-strain relations for two-dimensional cellular sandwich cores: Homogenization, material models, and properties. Appl Mech Rev 2002;55:61.

[12] Olympio KR, Gandhi F. Flexible skins for morphing aircraft using cellular honeycomb cores. J Intell Mater Syst Struct 2010;21:1719–1735.

[13] Dale AS, Cooper JE, Mosquera A. Topology optimization & experimental validation of 0-ν honeycomb for adaptive morphing wing. 22nd AIAA/ASME/AHS Adaptive Structrures Conference, National Harbor, Maryland, 2014.

[14] Olympio KR, Gandhi F. Zero poisson's ratio cellular honeycombs for flex skins undergoing one-dimensional morphing. J Intell Mater Syst Struct 2010; 21:1737–1753.

[15] Ju J, Kim DM, Kim K. Flexible cellular solid spokes of a non-pneumatic tire. Compos Struct 2012;94:2285–2295.

[16] Hu L, You F, Yu T. Effect of cell-wall angle on the in-plane crushing behaviour of hexagonal honeycombs. Mater Des 2013;46:511–523.

[17] Ruan D, Lu G, Wang B, Yu TX. In-plane dynamic crushing of honeycombs - A finite element study. Int J Impact Eng 2003;28:161–182.

[18] Papka SD, Kyriakides S. In-plane compressive response and crushing of honeycomb. J Mech Phys Solids 1994;42:1499–1532.

[19] Daryabeigi K. Heat transfer in adhesively bonded honeycomb core panels. J Thermophys Heat Transf 2002;16:217–221.

[20] Lu TJ. Heat transfer efficiency of metal honeycombs. Int J Heat Mass Transf 1998;42:2031–2040.

[21] Huang WC, Ng CF. Sound insulation improvement using honeycomb sandwich panels. Appl Acoust 1998;53:163–177.

[22] Davis EB. Designing honeycomb panels for noise control. Am Institue Aeronaut Astronaut 1999:792–801.

[23] Grosveld FW, Mixson JS. Noise transmission through an acoustically treated and honeycomb stiffened aircraft sidewall. J Aircr 1984;22:434–440.

[24] Ruzzene M. Vibration and sound radiation of sandwich beams with honeycomb truss core. J Sound Vib 2004;277:741–763.

[25] Wilson S. A new face of aerospace honeycomb. Mater Des 1990;11:323–326.

[26] Masters IG, Evans KE. Models for the elastic deformation of honeycombs. Compos Struct 1996;35:403–422.

[27] Kelsey S, Gellatly RA, Clark BW. The shear modulus of foil honeycomb cores: a theoretical and experimental investigation on cores used in sandwich construction. Aircr Eng Aerosp Technol 1958;30:294–302.

[28] Grediac M. A finite element study of the transverse shear in honeycomb cores. Int J Solids Struct 1993;30:1777–1788.

[29] Penzien J, Didriksson T. Effective shear modulus of honeycomb cellular structure. AIAA J 1964;2:531–535.

[30] Shi G, Tong P. Equivalent transverse shear stiffness of honeycomb cores. Int J Solids Struct 1995;32:1383–1393.

[31] Pan SD, Wu LZ, Sun YG. Transverse shear modulus and strength of honeycomb

cores. Compos Struct 2008;84:369–374.

[32] Chen DH. Bending deformation of honeycomb consisting of regular hexagonal cells. Compos Struct 2011;93:736–746.

[33] Chen DH. Equivalent flexural and torsional rigidity of hexagonal honeycomb. Compos Struct 2011;93:1910–1917.

[34] Hohe J, Becker W. Effective elastic properties of triangular grid structures. Compos Struct 1999;45:131–145.

[35] Hohe J, Becker W. An energetic homogenisation procedure for the elastic properties of general cellular sandwich cores. Compos Part BEngineering 2001;32:185–197.

[36] Hohe J, Beschorner C, Becker W. Effective elastic properties of hexagonal and quadrilateral grid structures. Compos Struct 1999;46:73–89.

[37] Qiao PZ, Wang JL. Mechanics of composite sinusoidal honeycomb cores. J Aerosp Eng 2005;18:42–50.

[38] Li YM, Hoang MP, Abbes B, Abbes F, Guo YQ. Analytical homogenization for stretch and bending of honeycomb sandwich plates with skin and height effects. Compos Struct 2015;120:406–416.

[39] Burlayenko VN, Sadowski T. Effective elastic properties of foam-filled honeycomb cores of sandwich panels. Compos Struct 2010;92:2890–2900.

[40] Sadowski T, Bęc J. Effective properties for sandwich plates with aluminium foil honeycomb core and polymer foam filling - Static and dynamic response. Comput Mater Sci 2011;50:1269-1275.

[41] Catapano A, Montemurro M. A multi-scale approach for the optimum design of sandwich plates with honeycomb core. Part I: Homogenisation of core properties.

Compos Struct 2014;118:664–676.

[42] Catapano A, Montemurro M. A multi-scale approach for the optimum design of sandwich plates with honeycomb core. Part II: The optimisation strategy. Compos Struct 2014;118:677–690.

[43] McFarland Jr. RK. Hexagonal cell structures under post-buckling axial load. AIAA J 1963;1:1380–1385.

[44] Wierzbicki T. Crushing analysis of metal honeycombs. Int J Impact Eng 1983;1:157–174.

[45] Timoshenko SP, Gere J. Theory of elastic stability. Stanford: Dover Publications, 2009.

[46] Zhang J, Ashby MF. The out-of-plane properties of honeycombs. Int J Mech Sci 1992;34:475–489.

[47] Aktay L, Johnson AF, Kroplin BH. Numerical modelling of honeycomb core crush behaviour. Eng Fract Mech 2008;75:2616–2630.

[48] Wilbert A, Jang WY, Kyriakides S, Floccari JF. Buckling and progressive crushing of laterally loaded honeycomb. Int J Solids Struct 2011;48:803–816.

[49] López Jiménez F, Triantafyllidis N. Buckling of rectangular and hexagonal honeycomb under combined axial compression and transverse shear. Int J Solids Struct 2013;50:3934–3946.

[50] Ju J, Summers JD, Ziegert J, Fadel G. Design of honeycombs for modulus and yield strain in shear. J Eng Mater Technol 2012;134:011002.

[51] Hou S, Ren L, Dong D, Han X. Crashworthiness optimization design of honeycomb sandwich panel based on factor screening. J Sandw Struct Mater 2012;14:655–678.

[52] Singh G, Hopkins JB. General selection of lattice shape in ductile-reinforced brittle structures for increased stiffness. Compos Struct 2015;131:325–332.

[53] Chen A, Davalos JF. A solution including skin effect for stiffness and stress field of sandwich honeycomb core. Int J Solids Struct 2005;42:2711–2739.

[54] Chen Q, Pugno N, Zhao K, Li Z. Mechanical properties of a hollow-cylindrical-joint honeycomb. Compos Struct 2014;109:68–74.

[55] Karnessis N, Burriesci G. Uniaxial and buckling mechanical response of auxetic cellular tubes. Smart Mater Struct 2013;22:084008.

[56] Ajdari A, Jahromi BH, Papadopoulos J, Nayeb-Hashemi H, Vaziri A. Hierarchical honeycombs with tailorable properties. Int J Solids Struct 2012;49:1413–1419.

[57] Sun Y, Pugno NM. In plane stiffness of multifunctional hierarchical honeycombs with negative Poisson's ratio sub-structures. Compos Struct 2013;106:681–689.

[58] Taylor CM, Smith CW, Miller W, Evans KE. The effects of hierarchy on the in-plane elastic properties of honeycombs. Int J Solids Struct 2011;48:1330–1339.

[59] Alderson A, Alderson KL, Chirima G, Ravirala N, Zied KM. The in-plane linear elastic constants and out-of-plane bending of 3-coordinated ligament and cylinder-ligament honeycombs. Compos Sci Technol 2010;70:1034–1041.

[60] Scarpa F, Blain S, Lew T, Perrott D, Ruzzene M, Yates JR. Elastic buckling of hexagonal chiral cell honeycombs. Compos Part A Appl Sci Manuf 2007;38:280–289.

[61] Lakes R. Materials with structural hierarchy. Nature 1993;361:511–515.

[62] Ajdari A, Jahromi BH, Papadopoulos J, Nayeb-Hashemi H, Vaziri A. Hierarchical honeycombs with tailorable properties. Int J Solids Struct 2012;49:1413–1419.

[63] Oftadeh R, Haghpanah B, Vella D, Boudaoud A, Vaziri A. Optimal fractal-like hierarchical honeycombs. Phys Rev Lett 2014;113:104301.

[64] Chen Q, Pugno NM. In-plane elastic buckling of hierarchical honeycomb materials. Eur J Mech A/Solids 2012;34:120–129.

[65] Sun Y, Chen Q, Pugno N. Elastic and transport properties of the tailorable multifunctional hierarchical honeycombs. Compos Struct 2014;107:698–710.

[66] Mousanezhad D, Ebrahimi H, Haghpanah B, Ghosh R, Ajdari A, Hamouda AMS, et al. Spiderweb honeycombs. Int J Solids Struct 2015;66:218–227.

[67] Larsen UD, Sigmund O, Bouwstra S. Design and fabrication of compliant micromechanisms and structures with negative Poisson's ratio. J Microelectromechanical Syst 1997;6:99–106.

[68] Ko WL. Elastic Constants for Superplastically Formed/ Diffusion-Bonded Sandwich Structures 1979;18:986–987.

[69] Fan HL, Jin FN, Fang DN. Mechanical properties of hierarchical cellular materials. Part I: Analysis. Compos Sci Technol 2008;68:3380–3387.

[70] Yu W, Davis CS. Buckling behavior and post-buckling strength of perforated stiffened compression elements. 1st International Specialty Conference on Cold-Formed Steel Structures, Rolla, Missouri, 1970.

[71] Roberts TM, Azizian ZG. Strength of perforated plates subjected to in-plane loading. Thin-Walled Struct 1984;2:153–164.

[72] Schlack AL. Elastic stability of pierced square plates. Experimental Mechanics 1964;4(6):167–172.

[73] Schlack AL. Experimental critical loads for perforated square plates. Experimental Mechanics 1968;8(2):69–74.

[74] Levy BS, Woolley RM, Kroll WD. Instability of simply supported square plate with reinforced circular hole in edge compression. Journal of Research 1947;571-577

[75] Nemeth MP, Stein M, Johnson ER. An approximate buckling analysis for rectangular orthotropic plates with centrally located cutouts. National Aeronautics and Space Administration Hampton va Langley Research Center, 1986.

[76] Maiorana E, Pellegrino C, Modena C. Elastic stability of plates with circular and rectangular holes subjected to axial compression and bending moment. Thin-Walled Struct 2009;47:241–255.

[77] Aydin Komur M, Sonmez M. Elastic buckling of rectangular plates under linearly varying in-plane normal load with a circular cutout. Mech Res Commun 2008;35:361–371.

[78] Aydin Komur M, Sonmez M. Elastic buckling behavior of rectangular plates with holes subjected to partial edge loading. J Constr Steel Res 2015;112:54–60.

[79] de Vasconcellos Real M, Isoldi LA, Damas AP, Helbig D. Elastic and elasto-plastic buckling analysis of perforated steel plates. VETOR-Revista de Ciências Exatas e Engenharias 2013;23(2):61-70.

[80] El-Sawy KM, Nazmy AS. Effect of aspect ratio on the elastic buckling of uniaxially loaded plates with eccentric holes. Thin-Walled Struct 2001;39:983–998.

[81] El-Sawy KM, Nazmy AS, Martini MI. Elasto-plastic buckling of perforated plates under uniaxial compression. Thin-Walled Struct 2004;42:1083–1101.

[82] El-Sawy KM, Ikbal Martini M. Elastic stability of bi-axially loaded rectangular plates with a single circular hole. Thin-Walled Struct 2007;45:122–133.

[83] Nemeth MP. Buckling behavior of compression-loaded symmetrically laminated angle-ply plates with holes. AIAA J 1988;26:330–336.

[84] Larsson PL. On buckling of orthotropic stretched plates with circular holes. Compos Struct 1989;11:121–134.

[85] Rockey K, Narayanan R. Ultimate load capacity of plate girders with webs containing circular cut-outs. ICE Proc 1981;71:845–862.

[86] Narayanan R, Chow FY. Ultimate capacity of uniaxially compressed perforated plates. Thin-Walled Struct 1984;2:241–264.

[87] Narayanan R DI. Strength of slender webs having non-central holes. Struct Eng Part B 1985:57–62.

[88] Shanmugam NE, Thevendran V, Tan YH. Design formula for axially compressed perforated plates. Thin-Walled Struct 1999;34:1–20.

[89] Shanmugam NE, Dhanalakshmi M. State-of-art review and compilation of studies on perforated thin-walled structures. Int J Struct Stab Dyn 2001;1:59–81.

[90] Hegarty RF, Ariman T. Elasto-dynamic analysis of rectangular plates with circular holes. Int J Solids Struct 1975;11:895–906.

[91] Lo CC, Lessian AW. Bending of plates with circular holes. Acta Mechanica 1967;4:64-78.

[92] Le Fort P. Bending of perforated plates with square penetration patterns. Nucl Eng Des 1970;12:122–134.

[93] Bailey RW, Hicks R. Behaviour of perforated plates under plane stress. J Mech Eng Sci 1960;2:143–165.

[94] Hoffman RE, Ariman T. Thermal bending of plates with circular holes. Nucl Eng

Des 1970;14:231–238.

[95] Osama Bedair. Stress analyses of deep plate girders used at oil and gas facilities with rectangular web penetrations. Pract Period Struct Des Constr 2011;16:73–81.

[96] Timoshenko, Stephen P. and SW-K. Theory of plates and shells. New York: McGraw-hill Book Company; 1959.

[97] Miller W, Smith CW, Scarpa F, Evans KE. Flatwise buckling optimization of hexachiral and tetrachiral honeycombs. Compos Sci Technol 2010;70:1049–1056.